TECHNISCHE UNIVERSITÄT WIEN

HEPHY INSTITUT FÜR HOCHENERGIEPHYSIK

DIPLOMARBEIT

Response of Si, SiC and LGAD Semiconductor Detector Systems to Alpha Radiation

zur Erlangung des akademischen Grades

Diplom-Ingenieur

im Rahmen des Studiums

Technische Physik

eingereicht von

Matthias Knopf
Matrikelnummer 11771051

ausgeführt am Atominstitut
der Fakultät für Physik der Technischen Universität Wien
(in Zusammenarbeit mit dem Institut für Hochenergiephysik (HEPHY))

Betreuung
Betreuer: Ass.Prof. Dipl.-Ing. Dr. techn. Albert Hirtl (Atominstitut)
Mitwirkung: Univ.Lektor Dipl.-Ing. Dr. techn. Thomas Bergauer (HEPHY)

Wien, 25.04.2023

(Unterschrift Verfasser) (Unterschrift Betreuer)

Abstract

This thesis investigates the response of various semiconductor detector systems to alpha radiation. The study is conducted in the context of new detector technologies aiming for faster timing resolution and improved radiation hardness, like Low Gain Avalanche Detectors (LGAD) and wide band gap materials like Silicon Carbide (SiC).

In order to characterize and develop new detector technologies, testing in known radiation environments is indispensable. Radioactive laboratory sources are a convenient way to achieve this without the need for a particle accelerator. Alpha sources especially exhibit the beneficial properties of an almost monoenergetic release of particles, as well as large signals in the sensors owing to their complete absorption in matter.

Due to the short range of alpha particles in atmospheric air and the associated energy loss, it is experimentally imperative to perform the measurements at sufficiently low pressures to obtain reproducible results. This was achieved by implementing a vacuum setup and testing the detectors at low pressure.

Using the vacuum setup, the performance of a conventional Silicon diode was compared to the behavior of SiC and LGAD sensors as a function of air pressure. Different electronic readout chains were studied and compared against each other (broad-band high-frequency amplifier with HF (High frequency) data storage vs. shaping spectroscopic amplifier and digitization using an oscilloscope). Complementary Monte Carlo studies were performed using the GATE (*Geant4 Application for Emission Tomography*) framework to support all measurement results with simulations and calibrate the energy axes of the spectra.

Applying the spectroscopic readout chain, a value of $\epsilon_{\mathrm{SiC}} = 7.755 \pm 0.132$ eV, for the ionization energy of SiC and $F_{\mathrm{SiC}} = 0.100 \pm 0.01$ for its Fano factor, were be experimentally determined by a comparison of Si and SiC spectra measured similar conditions.

Zusammenfassung

Diese Arbeit befasst sich mit der Signalantwort verschiedener Halbleiterdetektorsysteme auf Alphastrahlung. Die Studie wurde im Zusammenhang mit neuen Detektortechnologien durchgeführt, die auf eine schnellere Zeitauflösung und eine höhere Strahlenhärte abzielen, wie Low Gain Avalanche Detectors (LGAD) und Halbleiter mit breitem Bandabstand wie Siliziumkarbid (SiC).

Für die Charakterisierung und Entwicklung neuer Detektortechnologien sind Tests in bekannten Strahlungsumgebungen unerlässlich. Radioaktive Laborquellen sind eine praktische Möglichkeit, dies zu erreichen, ohne die Erfordernis eines Teilchenbeschleunigers. Insbesondere Alpha-Quellen weisen die günstigen Eigenschaften einer nahezu monoenergetischen Teilchenemission sowie große Signale in den Sensoren aufgrund ihrer vollständigen Absorption in der Materie auf.

Aufgrund der geringen Reichweite von Alphateilchen in Luft unter atmosphärischem Druck und dem damit verbundenen Energieverlust ist es experimentell erforderlich, die Messungen bei ausreichend niedrigem Druck durchzuführen, um reproduzierbare Ergebnisse zu erhalten. Dies könnte durch die Einrichtung eines Vakuum-Setups und das Testen der Detektoren bei niedrigem Druck erreicht werden.

Unter Verwendung des Vakuumaufbaus wurden die Eigenschaften einer herkömmlichen Siliziumdiode mit dem Verhalten von SiC- und LGAD-Sensoren in Abhängigkeit vom Luftdruck verglichen. Es wurden verschiedene elektronische Ausleseketten untersucht und miteinander verglichen (Breitband-Hochfrequenz-Verstärker mit HF (Hochfrequenz)-Datenspeicherung gegen einen spektroskopischen Verstärker und Digitalisierung mit einem Oszilloskop). Ergänzende Monte-Carlo-Studien wurden mit dem GATE (*Geant4 Application for Emission Tomography*)-Framework durchgeführt, um alle Messergebnisse durch Simulationen zu unterstützen und die Energieachsen der Spektren zu kalibrieren.

Unter Anwendung der spektroskopischen Auslesekette konnte ein Wert von $\epsilon_{\mathrm{SiC}} = 7.755 \pm 0.132$ eV für die Ionisationssenergie von SiC und $F_{\mathrm{SiC}} = 0.100 \pm 0.01$ für seinen Fano-Faktor experimentell bestimmt werden, indem Spektren von Si und SiC, die unter ähnlichen Bedingungen aufgenommen wurden, verglichen wurden.

Acronyms

ADC Analog Digital Converter.

APD Avalanche Photo Diode.

BB Broad Band.

CFD Constant Fraction Discrimination.

CSA Charge Sensitive Amplifier.

CSDA Continuous slowing down approximation.

DAQ Data Acquisition.

LGAD Low Gain Avalanche Detector.

MCA Multi Channel Analyzer.

MIP Minimum Ionizing Particle.

NIST National Institute of Standards and Technology.

PCB Printed Circuit Board.

PLC Programmable Logic Controller.

RF Radio Frequency.

SCPI Standard Commands for Programmable Instruments.

SMU Source Measure Unit.

SNR Signal to Noise Ratio.

TIA Trans Impedance Amplifier.

ToN Time over Noise.

ToT Time over Threshold.

UCSC University of California Santa Cruz.

UFSD Ultra Fast Silicon Detector.

Contents

1. Introduction

Ion therapy involves the use of high energy ions and specifically their unique deposition of energy in matter to treat cancer while minimizing damage to healthy tissue [1, 2]. Particle detection is a crucial component in this process: A precise and reliable characterization of the beam is essential for treatment planning and delivery.

The Institute of High Energy Physics (HEPHY) is partnering up with MedAustron (a cancer treatment facility and research center in Wiener Neustadt, Austria) to replace the current detector system within in the High Intensity Beam Position Monitor (HiBPM) project aiming at the development of an improved monitoring at high flux rates. This requires a new generation of fast, radiation hard detectors.

A number of upcoming experiments in high energy physics face a similar problem. In future high luminosity phases, the present instrumentation will not be able to resist the high particle fluxes and will no longer offer a sufficient time resolution to prevent high levels of pileup. Different strategies have been proposed to address this challenge [3, 4, 5].

Due to developments in the power electronics industry and the resulting commercial availability of high-quality wafers, Silicon carbide (SiC) has recently gained in interest as a potential candidate for such a material in the high energy physics community [6, 7]. SiC offers many prospective advantages over the ubiquitous Silicon (Si) currently in use. It is a wide band-gap material, which could allow for improved radiation hardness and an almost temperature independent performance. With a higher breakdown voltage and carrier saturation velocity than Si, the intrinsic time resolution may also be significantly improved. Additionally, SiC detectors have been found to have lower noise levels and leakage currents than traditional Si detectors. This makes SiC a promising material not only for medical applications, but also for high luminosity experiments and measurements in harsh radiation environments, where Si detectors might be pushed to their limits [5, 8].

In order to characterize the properties of a new generation of SiC detectors, a precise energy calibration is necessary. The charge collection efficiency of irradiated samples is an important metric for radiation hard detectors and its determination calls for a calibration in terms of the absolute number of collected charges [9]. Traditionally, alpha particles are used for calibration purposes as their high ionization leads to both large signal amplitudes and a total absorption within a few micrometers of matter. This circumstance, combined with a well known monoenergetic spectrum and the safe handling of laboratory sources makes them ideally suited for the task [10].

Despite all its advantages, the convenience of measuring alpha particles comes at a cost. As opposed to most other kinds of ionizing radiation the air in between the source and the detector causes significant energy straggling of the particle and hence complicates the interpretation of measured spectra. This can be circumvented by performing the experiments in a low pressure environment with the help of a vacuum chamber. A new vacuum setup up to this task was first implemented and tested at HEPHY for this work.

Over the course of this thesis, different electronic readout chains were employed and the alpha response of Silicon (Si), SiC and Si Low Gain Avalanche Detector (LGAD) detectors was studied and compared. To better understand the detector response to the laboratory sources, a series of complementary Monte Carlo simulations was performed and analyzed using GATE. The combination of both measurement and simulation serves as valuable input for the characterization of SiC detectors and provides a solid foundation for the investigation of material properties.

Chapter 2 of this thesis provides a brief summary of the theoretical background and underlying physics. Chapter 3 explains the experimental setup as well as the Monte Carlo simulations used to support the alpha measurements. Chapter 4 is dedicated to the implementation of the vacuum setup. Chapter 5 provides the results of the GATE simulations, while chapter 6 summarizes the results of the alpha measurements. Chapter 7 entails an experimental determination of the ionization energy of SiC by means of the new setup with chapter 8 concluding the findings of this thesis. In the end, an expansive appendix is given, containing selected measurement results, the source code for the pressure control and supplementary information concerning the uncertainty calculation for the ionization energy measurement.

2. Physical and Technological Background

2.1. Interaction of Charged Particles with Matter

As charged particles traverse matter they continuously interact either with the electronic shell or the nuclei of the surrounding atoms. Due to these interactions, the particles suffer quasi continuous energy loss through a number small collisions, usually assumed to be infinitesimal. Depending on the particles' energy, charge and mass the most relevant processes are ionisation, excitation, bremsstrahlung and other modes of elastic and inelastic scattering.

2.1.1. Bethe-Bloch Equation

For this work focusing on the interactions of alpha particles at moderate relativistic energies of about 5.5 MeV the most prominent type of interaction is the ionization of the surrounding atomic shells moderated by the Coulomb force. Upon encountering matter, a particle immediately interacts with many electrons consecutively. For every encounter a small portion of energy is transferred at the expense of the impinging particle. This is a statistical process and can be quantified by the Bethe-Bloch equation describing the mean rate of energy loss per unit path length the particle travels through matter. This quantity is known as the (linear) *stopping power*, usually denoted as $-\frac{\mathrm{d}E}{\mathrm{d}x}$. Properly speaking this should only be regarded to as *electronic stopping power*, as alongside the contribution of the electrons, a *nuclear stopping power* emerges, taking the inelastic collision of the ions with the surrounding nuclei into account. This separation is however negligible in terms of this work as the nuclear component is orders of magnitude smaller than the electronic contributions for energies of a few MeV.

For the Bethe-Bloch equation, multiple extensions and modifications exist, taking into account correction to the classically derived formula [11]. These concern shell corrections at low energies acknowledging the atomic binding of the electrons considered free in eq. 2.1 and radiative effects to be considered dealing with relativistic particles.

In its relativistic version for a heavy ($M \gg m_e$) particle with a charge of $z \cdot e$ and considering binding and density corrections the Bethe-Bloch equation is defined as

$$-\frac{1}{\rho}\frac{\mathrm{d}E}{\mathrm{d}x} = 2\pi N_\mathrm{A} r_\mathrm{e}^2 m_\mathrm{e} c^2 \frac{Z}{A}\frac{z^2}{\beta^2}\left[\ln\left(\frac{2m_\mathrm{e}\beta^2\gamma^2 c^2 T_\mathrm{max}}{I_\mathrm{e}^2}\right) - 2\beta^2 - \delta\right] \tag{2.1}$$

with

- N_A...Avogadro's number
- r_e...Classical electron radius
- m_e...Electron mass
- ρ...Absorber mass density
- Z/A...Atomic number and mass number of the absorber
- z...Projectile charge (in units of e)
- β, γ...Relativistic factors
- T_max...Maximum energy transfer to a free electron in a single collision (head on)
- I_e...Effective excitation potential (averaged over all atomic electrons)
- δ...Density correction

Figure 2.1 shows an example of a Bethe-Bloch curve for a relativistic particle in different absorbers. Although there are several dependencies in this formula for practical purposes the stopping power can be seen a function of just its velocity β or rather the impulse to mass ratio $\beta\gamma = \frac{p}{mc}$. Apart from the density ρ, the Bethe-Bloch equation is almost material independent, which is why stopping power is often given in terms of the mass stopping power $-\frac{1}{\rho}\frac{\mathrm{d}E}{\mathrm{d}x}$.

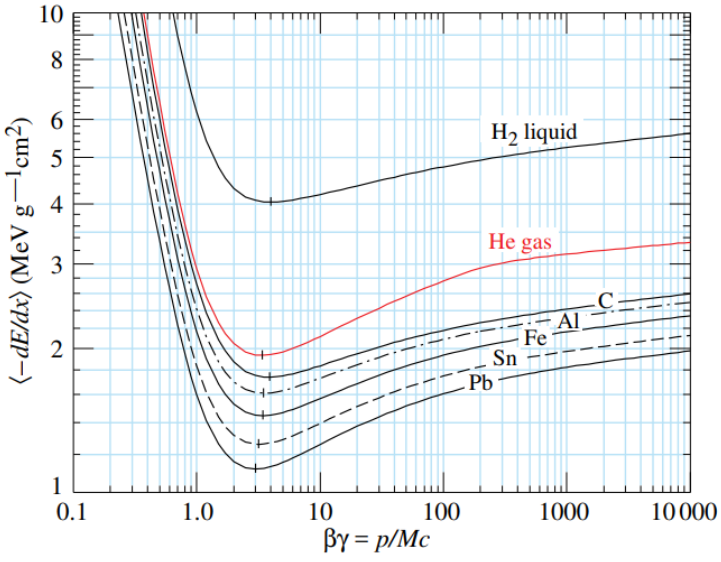

Figure 2.1.: A plot of the Bethe-Bloch equation visualizing the mean rate of energy loss in different absorber materials as a function of $\beta\gamma$. The shared minimum is clearly visible [11]

At low energies the $1/\beta^2$ term clearly dominates. Characteristically, all charged particles exhibit their minimum energy loss at a similar impulse to mass ratio $\beta\gamma \approx 3$. These are referred to as Minimum Ionizing Particles (MIPs) and are of high experimental relevance, as most particles produced in high energy physics experiments have a mean energy loss close to this minimum. For a particle detector, this dictates the minimum signal it needs to be able to resolve in order to function as such for high energy particles. Particles with $\beta\gamma$ above that of MIPs deposit higher rates of energy owing to the logarithmic term in the formula.

Bragg Curve

As a particle traversing the target loses energy, its rate of energy loss changes constantly. Owing to the $1/\beta^2$ term and the steep incline for low energies most of the initial particle's energy is lost in the last section of its path. By plotting the stopping power against the penetration depth one obtains the so-called *Bragg curve* with a distinct *Bragg peak* at the end. This point constitutes the maximum energy loss per unit path length. Having surpassed this stage there is little energy left to disperse and the particle is completely stopped. This convenient circumstance is the essence of a type of medical treatment known as *ion therapy* making use of the localized energy deposition in order to reduce tissue damage, radiation exposure and enable the treatment of deep seated tumors in cancer therapy. The characteristic form of a Bragg curve is depicted in Figure 2.2 for alpha particles in air.

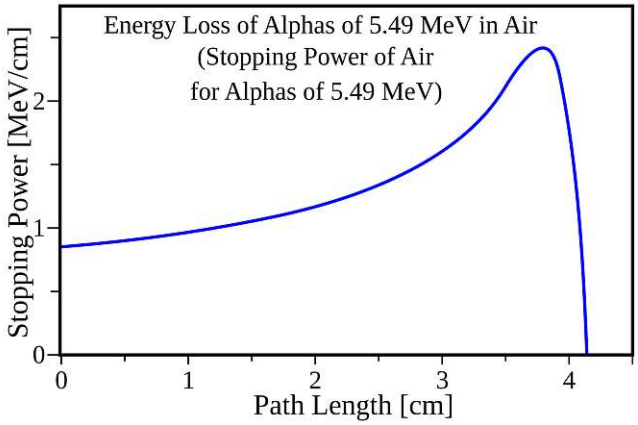

Figure 2.2.: The typical progression of a Bragg curve, depicted for alpha particles [12]

Range

In contrast to photon beams, the number of charged particles in an absorber does not decline exponentially as a function of penetration depth. Assuming a steady loss of energy, known as the Continuous slowing down approximation (CSDA), there is a well-defined range attributed to particles depending on their energy and the absorber material, although there are different definitions to be found in literature. However, as the stopping

of particles in matter is a statistical process the actual range is distributed around a mean value. This circumstance is called *range straggling* and is usually assumed to be of a Gaussian nature. Figure 2.3 shows an absorption curve for a charged heavy particle.

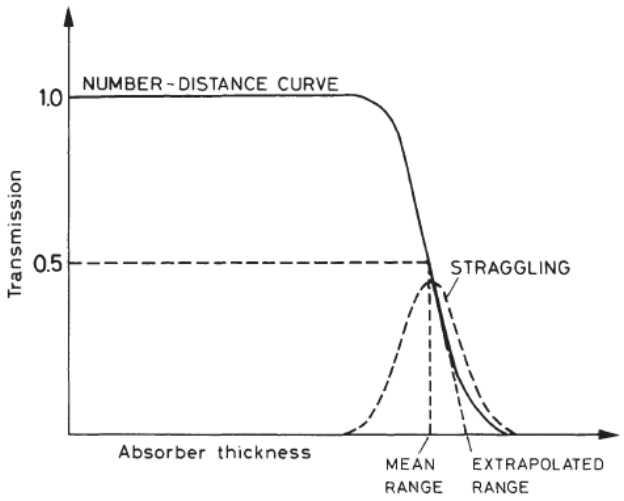

Figure 2.3.: The absorption curve of a charged heavy particle in matter. Mean range and extrapolated range are indicated in the plot [13].

The Bethe-Bloch equation allows an estimate of the range of a given particle by integrating the inverse of the infinitesimal energy loss from a given energy T_0 to zero

$$S(T_0) = \int_0^{T_0} \left(\frac{\mathrm{d}E}{\mathrm{d}x}\right)^{-1} dE \tag{2.2}$$

This formula however considers a random random path of the particle describing its total path length rather than its linear range along an axis. In the case of the heavy alpha particle however this does not constitute a significant difference as there is practically no change in direction while its ionizing the target's atoms due to the large momentum.

2.1.2. Energy Straggling - Gauss / Landau Distribution

The Bethe-Bloch formula just gives an estimate of the mean energy loss ΔE per path length Δx. The actual energy loss is composed of a number of statistically distributed small contributions δE fluctuating in both their number and the individual energy transfer. This phenomenon is known as *energy straggling* and leads to a probability density of energy transfer $f(\Delta E; \Delta x)$ for charged particles. An originally monoenergetic beam develops an energy distribution becoming wider with penetration depth. However, near the end of the range the distribution becomes narrower again, due to the energy transfers growing in magnitude. This behavior is illustrated in Figure 2.4.

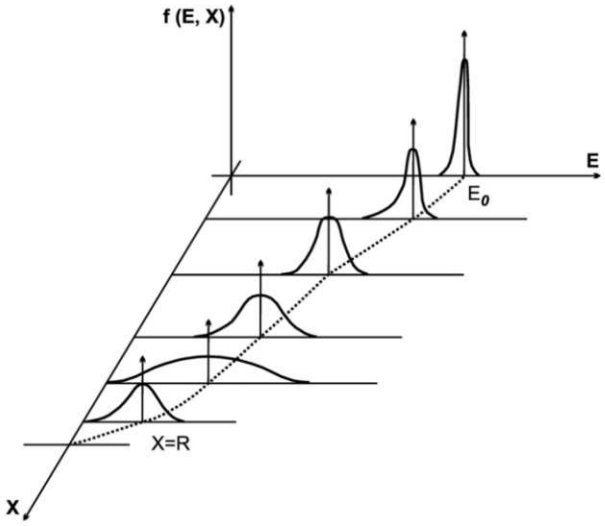

Figure 2.4.: Schematic illustration of the energy straggling of an alpha particle beam in matter [14].

$f(\Delta E; \Delta x)$ has two characteristic manifestations. Ideally the single δE are small enough to be statistically independent and the resulting probability distribution is a Gaussian curve. Usually the observed distribution will however exhibit an asymmetric shape composed of a Gaussian contribution with many small δE and a tail for the rare, high energy collisions and delta electrons that may be caused by the particles' passage. This distribution is skewed, meaning its *mean value* is no longer the *most probable value* of energy loss.

The degree of this asymmetry can be quantified by a ratio of the Bethe-Bloch prefactor $K_{\text{Bethe-Bloch}}$ (in front of the square brackets in eq. 2.1), multiplied with the path length and the maximum energy loss Tmax

$$\kappa = \frac{K_{\text{Bethe-Bloch}} \cdot \Delta x}{T_{\text{max}}}. \tag{2.3}$$

The larger κ, the more symmetric the given distribution is with the extremal case of a Gaussian distribution. For small κ the distribution is increasingly asymmetric. An analytic form is usually given for $\kappa \to 0$ as the Landau distribution via the integral

$$f_{\text{L}}(\lambda) = \frac{1}{\pi} \int_0^\infty \exp\{-t \ln(t) - \lambda t\} \cdot \sin(\pi t) dt. \tag{2.4}$$

For thick absorbers the energy loss distribution follows a Gaussian, while for thin absorber layers it follows a Landau distribution. For intermediate absorbers between those two limits, a convolution of a Gaussian and a Landau distribution, the Langau, can be used. Figure 2.5 illustrates the differences in these distributions.

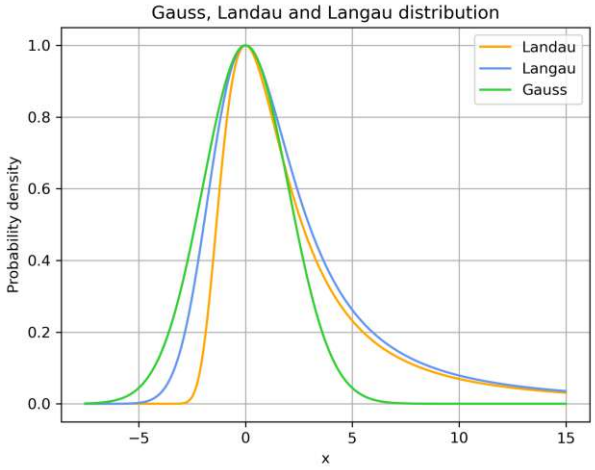

Figure 2.5.: Comparison plot of a standard Landau, Langau and a Gaussian ($\mu = 0,\ \sigma = 2.0$) probability distribution

2.1.3. Alpha Particles and their Interaction with Matter

Alpha decay is a type of nuclear decay common for heavy nuclei with atomic numbers above $Z = 83$ (i.e. beyond Pb and Bi) in which they spontaneously emit *alpha particles*, nuclei of ${}^{4}_{2}\mathrm{He}^{2+}$. This constitutes the nuclear reaction

$$ {}^{\mathrm{A}}_{\mathrm{Z}}\mathrm{X} \longrightarrow {}^{\mathrm{A-2}}_{\mathrm{Z-4}}\mathrm{Y} + {}^{4}_{2}\mathrm{He} + Q \tag{2.5} $$

in which Q denotes the decay energy which is set free and shared between the two reaction products. Considering the kinematics of this event, the kinetic energy of the alpha particle can be calculated from Q and the masses of the decay products as

$$ E_\alpha = Q \cdot \left(1 - \frac{1}{1 + m_Y/m_\alpha}\right). \tag{2.6} $$

Since the mass of the recoil atom m_Y is significantly higher than that of a He nucleus the latter takes the major share of the liberated energy and E_α is almost equal to Q. The energy range of naturally occurring alpha particles is between 2 and 8 MeV. For all practical purposes the emission is monoenergetic.

As opposed to other kinds of nuclear transitions like beta and gamma decay, alpha decay schemes and spectra are of a comparatively simple nature. Per nuclide there are only a hand full of possible alpha transitions with differing emission probabilities (see for example Figure 2.6 for ${}^{241}\mathrm{Am}$). As only the highest energy transition ends up in the ground state of the daughter nucleus, a lot of these alpha decays end up with an excited nuclear state and are usually followed by gamma emission. The energy differences are however relatively small and alpha lines of one radionuclide tend to show up in groups with often overlapping peaks. In practice, the list of alpha emitters with a sufficiently long half-life is short enough to easily identify different nuclides in alpha spectra.

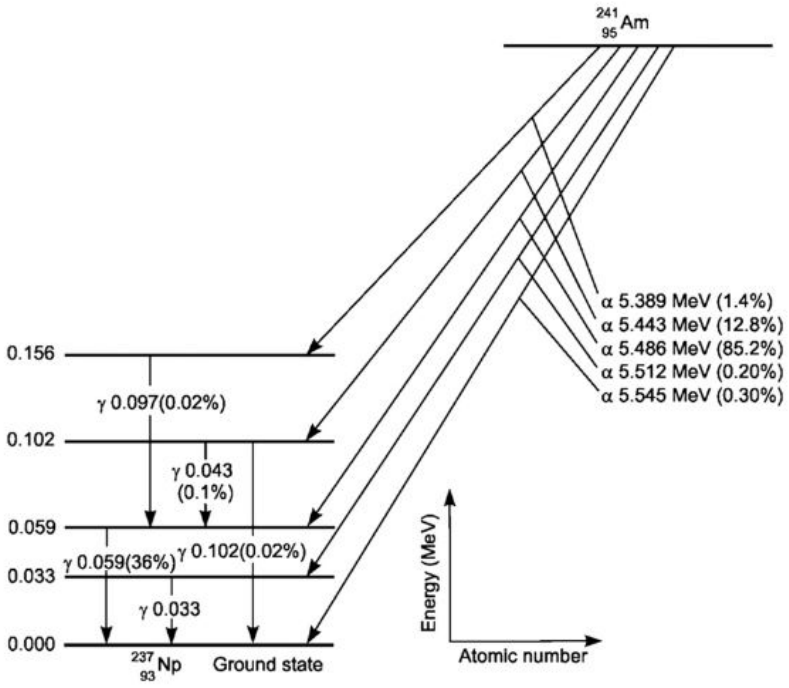

Figure 2.6.: Decay scheme of ^{241}Am. The relevant gamma transitions are indicated on the left. [10]

Alpha particles can be considered heavy particles and their behavior can be described in terms of the Bethe-Bloch equation 2.1. Below the GeV scale the stopping of alpha particles in matter is accomplished through a multitude of inelastic collisions with electrons, exciting or ionizing the atoms. As an alpha particle is almost 7500 times heavier than the atomic electrons and has a correspondingly high momentum, its direction of motion does not get significantly influenced by collisions and it deposits its energy on a straight path.

Via a quick relativistic calculation using the MIP condition from eq. 2.1 it is easily seen that alpha particles at the energies dealt with in this work are definitely not MIPs:

$$\beta\gamma \stackrel{!}{=} 3 \implies p_\alpha = 3m_\alpha c \tag{2.7}$$

In order to be of a minimum ionizing nature the particles would require an energy of

$$E^2 = p^2c^2 + m^2c^4 \implies E_\alpha^{\mathrm{MIP}} = \sqrt{10}m_\alpha c^2 \approx 11.8\,\mathrm{GeV}. \tag{2.8}$$

Depending on the (semiconductor) detector, the energy absorbed by a single ionization event is in the range of $1-10\,\mathrm{eV}$. A complete stop of a single alpha particle of a few MeV in matter leads to a production on the order of $10^5 - 10^6$ charge carriers. Because of its high ionisation cross section the penetration depth is usually very low compared to other types of radiation. In solid matter it is on the order of tens of µm.

In reference to the preceding chapter, alpha particles are expected to yield a Gaussian energy loss distribution as every absorber measuring more than a few µm can be considered thick for these particles. The low penetration depth has both advantages and disadvantages experimentally. On the one hand the particles deposit their total energy inside the active detector volume even with an incomplete depletion which leads to large signal charges. According to the National Institute of Standards and Technology (NIST) the CSDA range of a 5 MeV alpha particle in silicon with a nominal density of $2.329\,\mathrm{g\,cm^{-3}}$ is about 24 µm [15] which is less than a standard semiconductor detectors' bulk thickness. This makes them an ideal tool to produce a highly localized large number of electron-hole pairs. The high ionization cross section leads to peak shapes slightly deviating from the ideal Gaussian shape. Due to self-absorption in the source and variations in path lengths from the source to the detector (not all particles leave the source in a perfectly perpendicular direction) $f(\Delta E; \Delta x)$ often shows a low-energy tail seemingly skewing the distribution slightly towards higher energies. To inhibit this effect the alpha source should be as thin and be placed as close to the detector as possible. Different mathematical models have been proposed to fit alpha peaks accurately [10]. In this work a *skewed Gaussian* distribution

$$f(x) = \frac{1}{\sqrt{2\pi}\sigma} \cdot e^{-\frac{(x-\mu)^2}{2\sigma^2}} \left[1 + \mathrm{erf}\left(\frac{\gamma \cdot (x-\mu)}{\sqrt{2}\sigma}\right)\right] \tag{2.9}$$

was chosen, as it constitutes a relatively simple modification of a Gaussian distribution. The additional parameter γ indicates the strength of deviation (*skewedness*) from a perfectly symmetrical shape and $\mathrm{erf}(x)$ is the Gaussian error function. In a lot of cases the deviations are small and it is also possible to fit spectra using a Gaussian.

Alpha sources also have favorable properties in regards of radiation safety. Although alpha radiation is biologically the most hazardous, it is mostly harmless and easy to handle as long as alpha emitters are not ingested or inhaled. Alpha radiation of a few MeV does not even penetrate further than the dead skin layers in humans and is naturally very easy to shield.

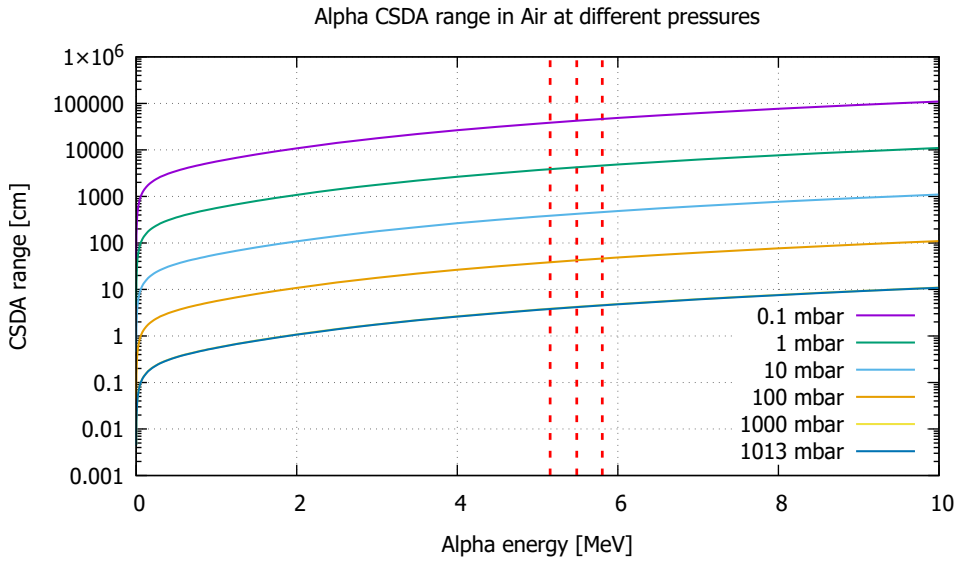

Figure 2.7.: CSDA range of alpha particles in air at different pressures. The dotted lines mark the main emission energies of the mixed nuclide alpha source utilized in this work (see section 3.5.2) [15].

The low range of alpha particles is, however, also one of the main experimental challenges. As opposed to most other kinds of high energy particles the surrounding air and detector structure is no longer a negligible factor. This can be visualized by plotting the CSDA range at different air pressures against the particle's energy as shown in Figure 2.7. At atmospheric pressure the range of an alpha particle with 5 MeV is just around 4 cm. By lowering the pressure to 1 mbar this can be extended to about 4 m.

A similar behavior may be observed for the Bragg peak of those particles. A GATE [16] simulation at different air pressures was done for particles emitted by an ^{241}Am source at 5.486 MeV. As observed in Figure 2.8, at about a pressure of 100 mbar the Bragg peak is no more prominent, and only very little energy is lost within the first 100 mm. Considerations like these necessitate the implementation of a vacuum setup in order to obtain reproducible and viable experimental results.

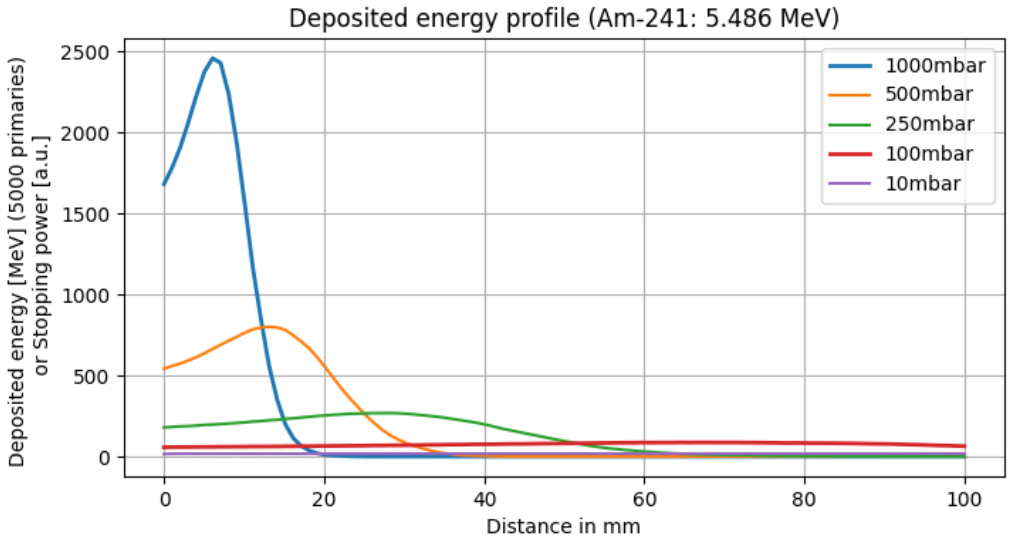

Figure 2.8.: The Bragg peak of alpha particles in air as a function of pressure. As the underlying GATE simulations were performed with a fixed number of particles this gives a statistical estimate of the deposited energy per single particle. At low pressures $\leq 100\,\text{mbar}$ the range increases dramatically.

2.2. Semiconductor Particle Detectors

Since the early 1960s solid state particle detectors began establishing themselves, mainly in the field of gamma spectroscopy. The main advantages of a solid state design are the far higher density of the absorber leading to a much higher energy loss in smaller volumes and the reduced diffusion drift compared to gas detectors. Further, the ionization energy in semiconductors is smaller than than in gasses by about a factor 5. Another benefit is the easy implementation with readout electronics as integrated circuits are also mostly silicon based and a broad option of manufacturing configurations is possible by exploiting existing techniques from the semiconductor industry. Another consideration is the high spatial resolution obtainable with semiconductor detectors, especially compared to the previously used wire chambers [17, 18].

2.2.1. Semiconductors

All solids can be roughly categorized by their electronic conduction in the *band model*. A schematic is shown in Figure 2.9. On a microscopic level this represents the internal electronic structure of solid matter. In solid states the single atoms are distributed densely enough for their individual electronic shells to influence each other. In a way the electronic electronic states "overlap" to form quasi-continuous *energy bands*. Individual bands of certain widths are separated by so called *band gaps*. It has to be noted, that in order to obtain a detailed picture of the electronic structure, the energy-impulse relationship $E(\vec{k})$ of the whole lattice has to be examined by solving or approximating the Schrödinger equation for the electrons. A simplified categorization is however possible by

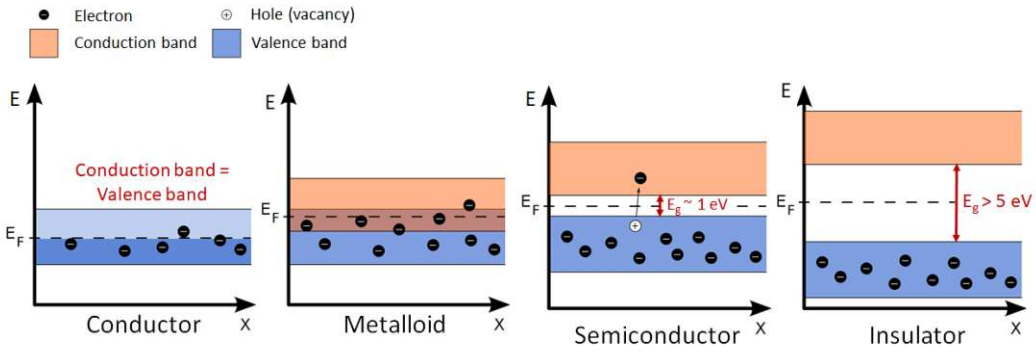

Figure 2.9.: The band model: a simplified model of the electronic band structure of electrons in solids. Adapted from [19]

looking at the behavior of the two energy bands surrounding the Fermi energy, the highest energy state a free electron can occupy at 0 K. The uppermost occupied band is referred to as *valence band*, the lowest unoccupied or partly occupied is called *conduction band*. Neither fully occupied nor completely empty bands contribute to charge transport. Unoccupied allowed energy states in a range of $\pm k_B T$ (with k_B being the Boltzmann constant) around the Fermi energy have to be available in order for a current to flow through a solid.

In conductors this is inherently given as both bands overlap partly or completely. There is no band gap and charge carriers can freely move between the bands without the help of external stimuli. In an insulator the electrons of the valence band are strongly bound and not easily freed by thermal excitation or external fields. There is a large band gap on the order of upwards of 10 eV and as a consequence the conduction band is completely unoccupied. There are no free charge carriers available for a current. Semiconductors also have band gaps but they are significantly smaller with an extent of a few eV. This way it is possible to partially overcome the separation of the bands by thermal excitation or external fields. As an electron is freed from its atom in this way it leaves behind a free negatively charged electron in the conduction band and a positively charged ion (electron vacancy) known as a *hole* in the valence band. Both act as free charge carriers.

Due to the temperature dependent occupation of the bands, semiconductors show an intrinsic charge carrier density at temperatures > 0 K. For technical applications it has proven valuable to deliberately manipulate these densities and the band structure by a process called *doping*. Usually semiconductors have 4 valence electrons. By introducing foreign atoms from either the third or fifth group of the periodic table the properties can be significantly altered.

- **n-doping** As pentavalent atoms are introduced in the lattice, the number of free electrons in the conduction band increases. There is one additionally introduced electron per foreign atom which is not able to bond to the crystal lattice. The n-doped material therefore is called an *electron donor* and is negatively charged.

- **p-doping** When implanting a trivalent atom, the lattice will always be an electron short for the required 4 covalent bonds per lattice site. This way there is a new vacancy introduced per foreign atom. The p-doped semiconductor is now positively charged and an *electron acceptor*.

Another way to look at the process is to imagine new energy levels being introduced inside the band gap which facilitate the promotion and demotion of electrons and holes between the bands. With n-type doping the lower edge conduction band is extended towards the Fermi energy whereas for p-type doping the upper edge of the valence band comes closer to it. Levels above the center of the band gap are called *donator levels* and those below the center *acceptor levels*. With a more sophisticated doping profile present in a single sample their relative strength is often indicated by $+$ or $-$ signs next to the polarity. Intrinsic semiconductors are often indicated with the letter i.

The significance of doped semiconductors is revealed once one brings two oppositely doped semiconductors together at a so-called *p-n-junction*. As they are of opposite charge the electrons and holes at the border quickly diffuse into the opposite region where they recombine with opposing free charges. Due to the intrinsic electric field a drift current opposing the diffusion current is introduced. Both counterbalance each other leaving a *depletion zone* devoid of free charge carriers which is dominated by the remaining ionized atoms. Figure 2.10a shows this mechanism and the associated quantities.

By contacting the doped regions one can manipulate the extent of the depletion zone as shown in Figure 2.10b. This constitutes a diode with an anode at the p-type and a cathode at the n-type region. As a positive voltage is applied to the p-side and a negative one to the n-side (*forward bias*) the drift current is reduced in relation to the diffusion current. The charge carriers are basically pushed away from the electrodes and recombine. The depletion volume decreases. Applying the opposite configuration (*reverse bias*) with the positive potential on the n-side the diffusion current is reduced and the depletion volume increases. One can imagine the charges being "transported away" by the electrodes. This depletion can be driven to a maximum by applying a high enough voltage known as the *full depletion voltage*. At this point no remaining free charges are left in the bulk material. This is the mode semiconductor detectors are usually operated in.

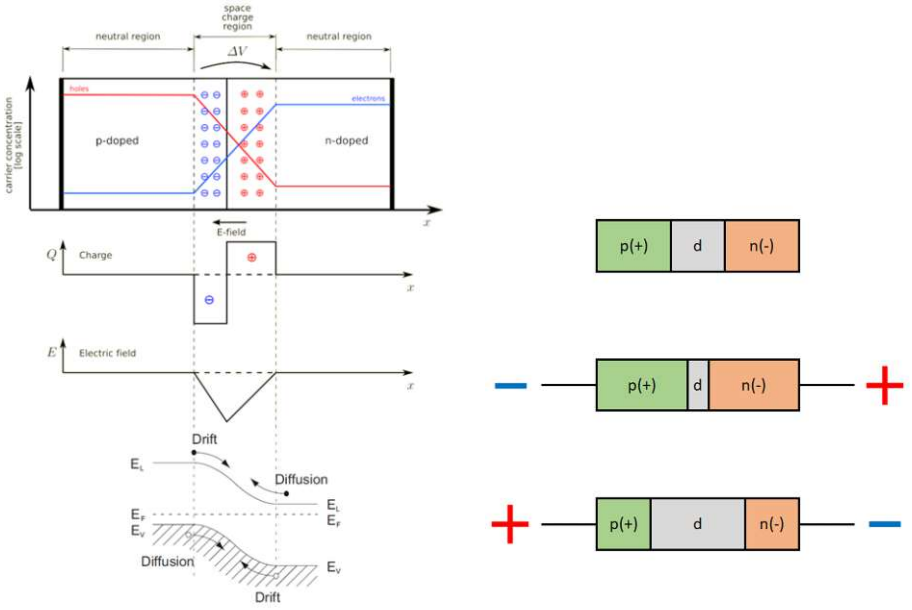

(a) Schematic of a pn junction

(b) Manipulation of the depletion zone via external biasing

Figure 2.10.: Visualisation of the phenomenology of pn junctions. On right side the operational modes of a diode are shown (no external voltage, forward bias, reverse bias). The left side shows the doping concentrations, space charges and electrical field of a pn junction. The lower schematic indicates the drift and diffusion of the charge carriers around the fermi level. Adapted from [20] [17].

2.2.2. Basic Principles

A semiconductor detector is a diode operated in reverse bias (most often at full depletion). It works like an ionization chamber and converts the deposited energy of an impinging charged particle into an electrical signal. As the particle is absorbed in the semiconductor it produces a number of electron-hole pairs along its path. The process is illustrated in Figure 2.11. The amount of liberated charge carrier pairs is proportional to the absorbed energy. As they move under the influence of an external field (introduced through the bias voltage) they produce a current which can be integrated over time to yield the freed charge, a direct measure of the incident particle's energy.

The average signal charge per completely absorbed particle is given as

$$Q_S = \frac{E}{\epsilon_i} \cdot e \tag{2.10}$$

with E as the absorbed energy, ϵ_i as the energy required to from an electron-hole pair (*ionization energy*) and the electron charge e. In order to yield a signal E has to exceed the ionization energy of the semiconductor. As an estimate of scale, pure Silicon (Si)

has a gap energy of E_g =1.12 eV and an ionization energy of ϵ_i =3.62 eV [17]. A MIP produces on average 108 and most probably 72 charge carrier pairs per µm path length (following a Landau distribution) in Si.

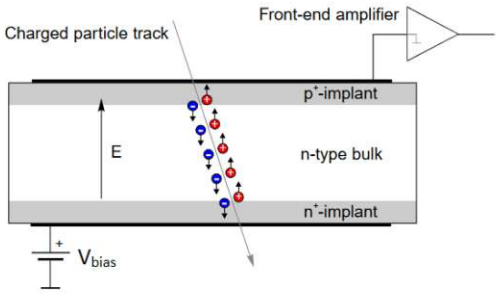

Figure 2.11.: Schematic cross section of a semiconductor sensor pad. The traversing particle ionizes the depleted bulk [21].

This allows a quick estimate which strikingly reverse biasing the need for depletion in semiconductor sensors. The intrinsic carrier density of pure silicon at 300 K is about $N_i = 10^{10}$ cm^{-3} [22]. Following eq. 2.1 a MIP on average loses $\frac{dE}{dx}$ =3.88 MeV cm^{-1} inside the material. The produced signal for a particle travelling a distance of d =300 µm is thus on the order of 10^4 electron-hole pairs:

$$\frac{\frac{dE}{dx} \cdot d}{\epsilon_i} \approx 3.2 \cdot 10^4 \tag{2.11}$$

whereas the number of intrinsic charges in a volume with surface area A =1 cm^3 is four orders of magnitude higher with

$$N_i \cdot d \cdot A \approx 3.03 \cdot 10^8. \tag{2.12}$$

In order to obtain any useful signal from a semiconductor detector the sensitive volume has to be significantly depleted of its intrinsic charges, even for alpha radiation with possibly upwards of 10^6 produced charge carrier pairs.

As the freed charges begin to move in the electric field they induce a charge on the sensor electrodes. Their velocity is a function of the local electric field $\vec{E}(x)$

$$\vec{v}(x) = \mu \vec{E}(x) \tag{2.13}$$

where μ is the mobility of the respective charge carrier

$$\mu_i = \frac{e\tau_i}{m_i}. \tag{2.14}$$

This dependency is obtained within the Drude model as a simplification of the Boltzmann transport equation in relaxation time approximation. τ is the mean free time between collisions (also known as carrier lifetime) and m the respective particle's effective

mass (basically a manifestation of the band structure). It has to be noted that all these values are temperature dependent. Typical values for silicon at 300 K are 1450 $\mathrm{cm^2\,V^{-1}\,s^{-1}}$ for electrons and 500 $\mathrm{cm^2\,V^{-1}\,s^{-1}}$ for holes [17], the holes being slower due to their higher mass.

In order to establish a high field and enable short signal collection time the absorbers resistivity

$$\rho = \frac{1}{e(\mu_\mathrm{e} n_\mathrm{h} + \mu_\mathrm{h} n_\mathrm{h})} = \frac{1}{e\mu n_\mathrm{eff}} \tag{2.15}$$

(where n_e, n_e are the electron and hole densities and n_eff is the effective doping concentration) has to be sufficiently high. As this quantity is usually exponentially dependent on the band gap energy, the choice of suitable detection materials is limited. Reverse bias diode structures are a good solution to achieve this compromise, as it is possible to establish a quasi insulator in the depletion zone while being able to maintain a high electric field over the whole region. Considering the doping of the wafer substrate, sensors may be implemented as either p-in-n or n-in-p structures or even more sophisticated doping profiles depending on the particular application.

The current-voltage (I-V) behavior of a semiconductor sensor mimics an ideal diode following the Shockley equation

$$I = I_0 \cdot \left(e^{eV/k_\mathrm{B}T} - 1\right) \tag{2.16}$$

with its typical progression shown in Figure 2.12a. I_0 is the reverse saturation current caused by the diffusion of minority charge carriers into the depletion zone. With a fully depleted detector this is a negligible contribution. Bigger problems may be caused by the current generated solely by thermal excitation (*dark current*) and leakage currents evoked by impurities or material damage. This can be mitigated by cooling the detector, finding suitable materials with wider band gaps and several isolating structuring techniques like *guard rings* or *p-stops* [23, 17].

On the other hand, planar semiconductor sensor also resembles a plate capacitor and can be modeled as such with the depletion zone as a stand-in for the dielectric. The sensor capacitance is then calculated as

$$C = \varepsilon_0 \varepsilon_\mathrm{r} \frac{A}{d} \tag{2.17}$$

with the dielectric constant $\varepsilon_0\varepsilon_\mathrm{r}$, the junction area A and the extent of the depletion zone d. This depletion width can be calculated from the bias voltage V_b

$$d = \sqrt{2\varepsilon_0 \varepsilon_\mathrm{r} \mu \rho |V_\mathrm{b}|} = \sqrt{\frac{2\varepsilon_0 \varepsilon_\mathrm{r} |V_\mathrm{b}|}{n_\mathrm{eff}\ e}}. \tag{2.18}$$

Values for the bias voltage are, depending on sensor material, geometry and thickness

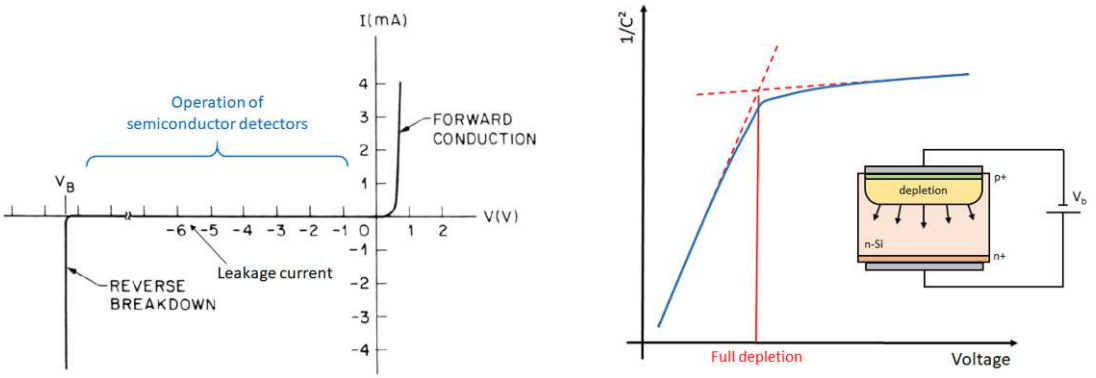

(a) IV curve of a pn diode

(b) Semiconductor detectors as capacitors.

Figure 2.12.: Semiconductor sensors as diodes (a) and capacitors (b). The right hand figure details method to determine the full depletion voltage of a detector and the propagation of the depletion volume with rising bias voltage. IV curve adapted from [24].

ranging from V_b =10–1000 V. The capacitance is proportional to this voltage

$$C \propto \frac{1}{\sqrt{V_\mathrm{b}}}, \tag{2.19}$$

which can be used to determine the full depletion voltage of a given sensor as indicated in Figure 2.12b. In electrical circuits a semiconductor sensor is often modelled as a current source in parallel with a capacitance. Typical magnitudes for the capacitance of a Si diode with 100 µm thickness are on the order of 1 pF mm^{-2} [23]. To obtain a spatial resolution of particle tracks the electrodes can be segmented in various ways. There are several strategies like strip sensors, pixel sensors as well as concepts aiming at an integration of the readout circuit in the silicon bulk [25, 26, 27]. The basic working principle of all these designs is however the same as with a pad detector, they only differ in their surface structure.

2.2.3. Signal Formation

The detection of a particle in every ionization detector follows the same scheme independent of the detector specifics. After energy deposition in the active volume and the generation of electron-hole pairs, the charge carriers are separated by an electric field and drift towards them in opposing directions. These moving charge carriers induce charges on the electrode surfaces which are then registered as a voltage, current or charge signal by a readout circuit. The registered signal emerges from the movement of charges relative to the electrodes. It is not necessary for the charges to actually reach the electrodes in order to evoke a response.

The process of signal formation in ionization detectors is described by the Shockley-Ramo theorem [28, 29]. It assumes a point charge q moving in a closed volume between two or more electrodes evoking an electric field $\vec{E}_0$. The field of the electrodes exerts an amount of work $dW_q = q\vec{E}_0 d\vec{r}$ necessary to perform this task which is itself provided by the voltage supply of the electrodes. Energy conservation requires

$$dW_q + dW_U = q\vec{E}_0 d\vec{r} + dQU \;\Rightarrow\; dQ = -q\frac{\vec{E}_0}{U}d\vec{r} \tag{2.20}$$

and hence gives the magnitude of the influenced charge dQ on the electrodes. As the field is purely given by the electrode geometry and proportional to U itself, the quantity $\vec{E}_0/U$ and the influenced charge are also independent of the supply voltage. It may be set to $U = 1$ defining the normalized *weighting potential* and a corresponding *weighting field*

$$\phi_\mathrm{w} = \frac{\phi_0}{U}, \quad \vec{E}_\mathrm{w} = -\vec{\nabla}\phi_\mathrm{w}. \tag{2.21}$$

The charge signal is now given as

$$dQ = -q\vec{E}_\mathrm{w} d\vec{r} \tag{2.22}$$

which can be modified to give the signal current

$$i_\mathrm{S} = -\frac{\mathrm{d}Q}{\mathrm{d}t} = q\vec{E}_\mathrm{w}\vec{v}. \tag{2.23}$$

The definition of the weighting field enables several simplifications in dealing with the electrodynamics of semiconductor detectors. The doping profile of the depleted volume shapes the electric field and hence influences the velocity and direction of the charges $\vec{v}$ (see eq. 2.13). It does not change the weighting field. Neither does the magnitude of the electrical field between the electrodes depending on the bias voltage. The influenced signal is solely dependent on the geometry of the setup. This holds true for an arbitrary number of electrodes in any configuration. A weighting field is calculated for every electrode. In practice one can resort to a single one for the readout electrode. In a parallel plate capacitor it is inversely proportional to the distance of the electrodes $E_\mathrm{w} = 1/d$.

The signal form can be calculated from eq. 2.23. The total signal $i_\mathrm{S}(t)$ is the superposition of the $i_\mathrm{S}^{\pm}(t)$ per charge carrier. Instead of a linear progression, as it manifests itself in ionisation detectors without space charges, the semiconductor signal current exhibits an exponential shape

$$i_\mathrm{S}^{\pm} \propto e^{-\frac{t}{\tau_\pm}}, d, \tau_\pm, V_\mathrm{b}, V_\mathrm{dep}. \tag{2.24}$$

Above $V_\mathrm{b} \approx 2V_\mathrm{dep}$ the progression, however, is almost linear and can be simplified. The technically most interesting aspect of $i_\mathrm{S}(t)$, its duration, depends mainly on the thickness of the detector d, the time between collisions τ as well as a sufficiently high bias voltage V_b. The bias voltage has to exceed the full depletion voltage V_dep in order to yield a finite zero crossing time [17]. τ can be taken as a stand-in for the electronic structure of the

semiconductor, which is usually taken into account via the carrier mobility μ. Figure 2.13 shows a sketch of the expected signal form for a slightly overdepleted silicon detector next to that of a gas filled detector. Integrated over time, eq. 2.24 gives the signal charge Q_S. It has to be stressed that this signal form is only theoretically valid. When measuring real current signals, the amplifier has a limited bandwidth and thus a limited rise time.

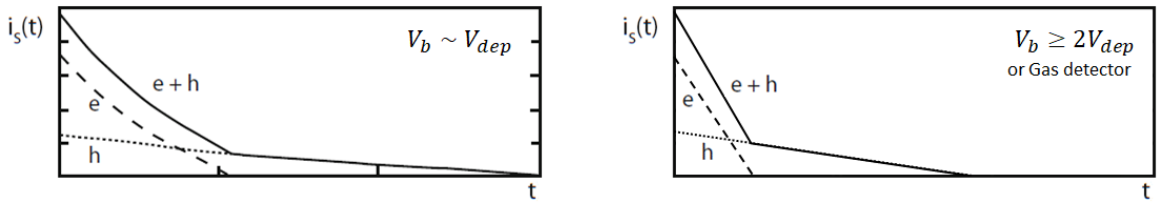

(a) Detector with space charge

(b) Detector strongly overdepleted or without space charge

Figure 2.13.: Typical time dependency of the signal current $i_S(t)$ on the negative electrode of a silicon detector next to a gas detector signal. The signal of a strongly overdepleted silicon sensor also approaches the triangular one. The path of incident particle is assumed orthogonal and uniformly ionizing along a straight line. Adapted from [17]

2.2.4. Conventional Silicon (Pad) Detectors

The pad design is the conceptionally easiest geometry for a sensor. It features just one active area without any segmentation. This allows for an easy readout and serves as a good tool for basic testing. Silicon is by far the most ubiquitous detector material in semiconductor technology, due to its historical prominence as well as its cheap and easy accessibility, but also its convenient material properties for particle detection. Its band gap of 1.12 eV [17] is a good compromise for detecting particles and generating a relatively large number of electron-hole pairs per MeV.

Although it is light sensitive, the extent of the band gap does not make it too sensitive to photons as to render huge leakage currents in dark environments and shielding in the optical spectrum is sufficient. Further it does not need to be cooled like Germanium as its not as prone to thermal excitations. Si can be manufactured in very high purities featuring arbitrary doping profiles thanks to the decades of experience in the semiconductor industry. Charges also have a high mobility in Si which allows for relatively fast detectors. Selected material properties are given in Table 2.1. Future high luminosity experiments and intense radiation environments however call for a new generation of detector technology due to shortcoming of conventional Si in these aspects [30].

Property	4H-SiC	Si
Atomic number Z	∼10	14
Density [g/cm^3]	3.22	2.33
Thermal conductivity [W/Kcm]	4.9	1.5
Bandgap [eV]	3.23	1.12
e-h pair creation energy [eV]	5-8	3.62
Mean e-h pairs per µm (MIP)	∼ 57	80
Electron mobility [cm^2/Vs]	800 - 1000	1300 - 1450
Hole mobility [cm^2/Vs]	115 - 120	450 - 460
Saturated electron drift velocity [10^7 cm/s]	2.0 - 2.2	0.8 - 1.0
Approx. breakdown field [MV/cm]	∼3	∼0.3

Table 2.1.: Selected physical properties of 4H-SiC and Si at 300 K. Some values are still ambiguous in literature and provided as ranges here. [5, 31, 32]

2.2.5. Silicon Carbide as a Detector Material

Silicon carbide (SiC) is a promising candidate for a new generation of particle detectors requiring faster signal times and an enhanced radiation hardness. To the physics communities' benefit, it also features a number of fortunate electrical and mechanical properties. This made it an interesting material for the semiconductor and especially power electronics industry and lead to an increased availability. [33]

SiC is considered a *wide band gap material* with a band gap more than double the width of conventional silicon. This renders the need for a temperature control obsolete as thermal excitations are no longer able to promote charge carriers to the conduction band. The operation is essentially temperature independent (below about 300 °C [34, 35]) and shows a reduced dark current. The high displacement threshold compared to other semiconductors should theoretically improve radiation hardness. SiC exhibits a significantly higher breakdown voltage as well as considerably higher saturated drift velocity than Silicon increasing the intrinsic time resolution of detectors. It is also an excellent thermal conductor and incidentally one of the hardest naturally occurring materials. Generally speaking, in some sense the properties of SiC are a compromise between Si and diamond as it is structurally relatively similar.

SiC manifests in a large number of different amorphous and crystalline structures called *polytypes* differing in their structure and characteristics. The most relevant polytypes for the particle physics (and also semiconductor) community are known are the cubic structure 3C-SiC and the hexagonal 4H-SiC and 6H-SiC. 4H-SiC is the most commonly used polytype for particle detectors as it shows an optimal interplay of mechanical and electrical properties and can be reliably manufactured [31]. Selected properties of 4H-SiC are given in Table 2.1 next to Si values commonly accepted by the community. As the advent of SiC is relatively recent some the literature is still quite ambiguous in some values. In chapter 7 this work aims at contributing to a clarification by determining the ionization energy via spectroscopic measurements.

2.2.6. The LGAD concept

The LGAD concept, also known as Ultra Fast Silicon Detector (UFSD), works similar to an Avalanche Photo Diode (APD). All APD detectors achieve charge multiplication by introducing a high electrical field through an additional doping layer close to the readout electrode. This is triggering a process called *impact ionization*. During the charge collection, secondary ionization enables the buildup of a charge avalanche. [24] Figure 2.14 shows the schematic structure of an p-in-n LGAD device next to an illustration of the avalanche process.

The charge multiplication allows for a vast increase in signal charge and the fabrication of much thinner detectors and consequently a faster timing resolution. In contrast to an APD the gain is however kept at a moderate level of around 10 to maintain a low level of dark current, preserve the radiation hardness and to ensure a proportionality to the deposited charge [36, 37, 21].

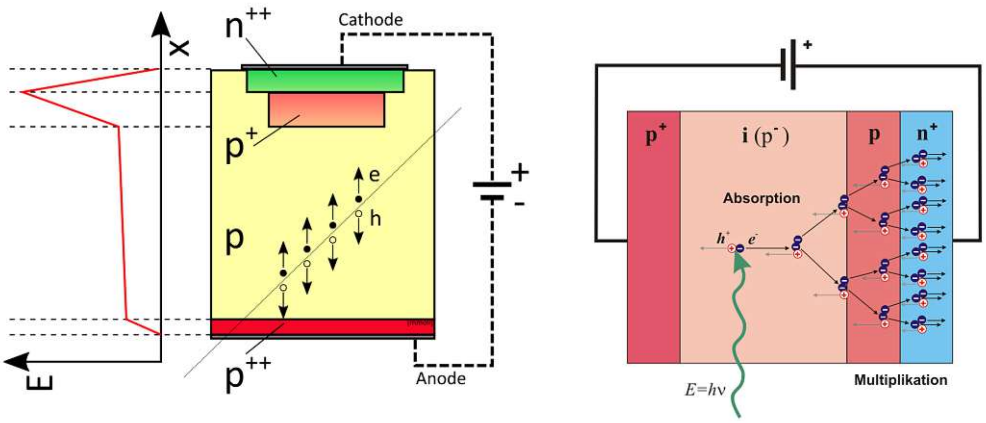

(a) LGAD cross section and electric field (b) The avalanche process

Figure 2.14.: A schematic of an LGAD device with the characteristic electrical field next to a schematic of the charge multiplication process for electrons in an APD. Adapted from [38, 39]

2.3. Readout

The current signal generated by a detector has to be processed to be of any experimental use. Usually the *readout chain* can be split in two major parts: The *front end* being directly involved in signal generation and shaping and the *back end* for digitizing and processing the information for further use. Figure 2.15 shows a scheme for a typical set of electronics in a particle physics experiment.

The front end usually features four main components:

- Sensor: Converts a particle's deposited energy into an electrical signal
- Amplifier: As the signal charge is very small it has to be amplified significantly; Usually this is a charge sensitive amplifier processing the signal charge as $Q_S = \int idt$
- Shaper: To improve the Signal to Noise Ratio (SNR) and optimize the further processing with a appropriate pulse shape; Usually this entails a bandpass filter
- Data concentration: As there is noise and lots of unwanted features in the signal curve, the relevant information has to be selected (e.g. by a multiplexer, threshold triggers or a sample and hold)

In the back end one typically finds:

- Analog Digital Converter (ADC): To digitize the analog signal into concrete numerical values
- Digital processing and filtering (e.g. setting a baseline, removing noise, attaching time stamps, ...)
- Buffer: May actually be implemented on several steps in the chain as a preliminary fast storage (there is usually some delay passing information to the next component)
- Computer or other Data Acquisition (DAQ) systems (oscilloscopes, etc.)

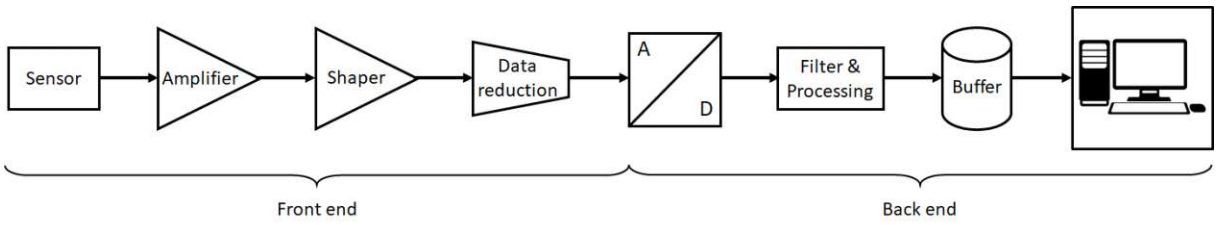

Figure 2.15.: A typical readout chain for a particle physics experiment

3. Data Acquisition and Analysis

3.1. Alpha Measurement Setup

The basic setup shared by all alpha response measurements was kept fairly simple consisting only of the sensor itself mounted on a circuit board, an amplifier and an oscilloscope for the digitization of the signals. There were two different versions of Printed Circuit Boards (PCBs) used to mount the sensors. The first configuration just features a simple geometry allowing for biasing and readout of a diode (CERN SSD board 25, referred to as *ceramic board* in the following). The second PCB is a version (V1.4) of the UCSC LGAD board featuring an on-board Trans Impedance Amplifier (TIA) (see section 3.2.1). The DAQ is controlled by a PC running dedicated software developed in-house at HEPHY. Detailed readout chains are discussed below in section 3.2.

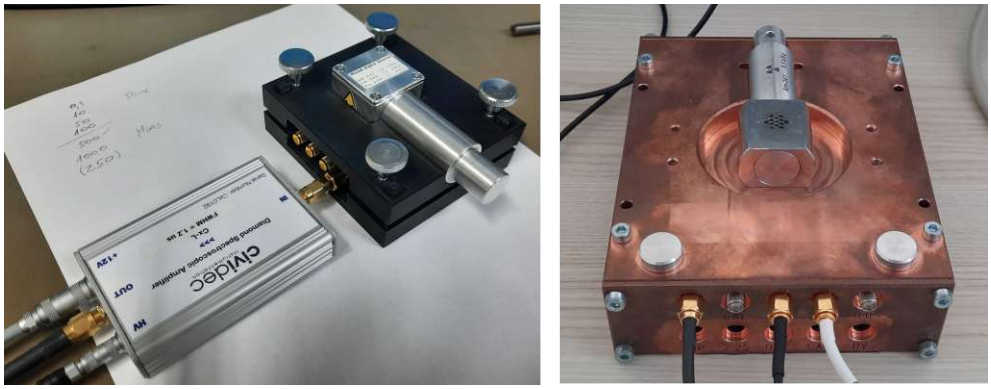

Figure 3.1.: The custom made holders (3D printed alpha holder, copper box) with the two radioactive sources used for the alpha measurements in this work. The shaping amplifier can be seen attached to the left circuit board.

The measurement were performed using laboratory alpha sources as described in section 3.5. The sources and PCBs are mounted in custom made holders in order to ensure a constant distance between detector and radioactive source. This is necessary to limit the variability due to scattering in air. The LGAD board is inserted in a copper box featuring a milled slot for the alpha source while a 3D printed prototype (*alpha holder*) was used for the ceramic boards. Both are shown in Figure 3.1. With the copper box the source-detector distance is (8.0 ± 0.1) mm. The 3D printed holder can be adjusted in height and was kept at that same distance for all measurements. This distance is a compromise between reducing energy losses and a safety margin for the bond wires on top of the PCBs.

The bias voltage (high voltage, HV) for the diodes was provided by either a Keithley 2410 or 2470 Source Measure Unit (SMU). The amplifiers and the UCSC board electronics (low voltage, LV) are supplied by a Rhode & Schwarz NGE100 power supply. The measurements were partially performed in a newly implemented vacuum setup which is described in chapter 4. All measurements were performed at room temperature. Measurements bearing the title "1000 mbar" were performed at ambient pressure, which might vary up to 25 mbar depending on the location of the setup and meteorological conditions.

As the energy loss of particles in matter is a statistical process, an adequate number of events have to be recorded in order to yield a statistically significant distribution. To keep track of the huge amounts of data accumulating this way (several 10k waveforms per measurement run), it is necessary to manage the readout automatically with the help of a computer. In this work the digitization of the amplifier signals was performed with either a Rhode & Schwarz RTO6 or RTP164 oscilloscope. The internal trigger is set manually above the noise level to only record events of interest. The fast oscilloscopes have a bandwidth of 4 GHz with a sampling rate of 20 GSa/s (RTO6) and 16 GHz with 40 GSa/s (RTP164) respectively. The high bandwidth is necessary for measurements using the Broad Band (BB) amplifier or the LGAD board, as the signals are typically only a few ns long (see section 6.2.2). Both oscilloscopes can achieve a 16 bit vertical resolution in the *HD mode* by using a low pass filter.

For testing purposes and low resolution spectroscopic applications not requiring a resolution like this a standard mid-range oscilloscope was employed. The Tektronix TBS2204B has a bandwidth of 200 MHz with 2 GSa/s and features a standard 8 bit vertical resolution.

For the RTO6 and RTP164 oscilloscopes, the input impedance was set to 50 Ω to avoid reflections. For the Tektronix oscilloscope, a parallel 50 Ω terminator was used.

As the amplifiers are very sensitive to high frequency Radio Frequency (RF) noise, the alpha holder containing the source and detector were wrapped in aluminium foil to shield it. With the copper box, no additional shielding was necessary. Cables on the input side of the amplifiers were kept as short as possible to prevent noise pickup.

3.2. Readout Electronics

One goals of this thesis is the comparison of different readout methods. The basic setup follows the description of the preceding chapter employing three different types of amplifiers: The UCSC LGAD board, a BB amplifier and a spectroscopic shaping amplifier.

3.2.1. LGAD Board

The LGAD readout board is a PCB for fast sensor readout widely known and applied within the community. It is distributed by the University of California Santa Cruz (UCSC) and thus also referred to as the UCSC board. It offers a low noise onboard amplification via an inverting TIA. A HV input, which is capacitively decoupled from the amplifier, can be used to bias the detector. The amplification Z_{trans} can be directly influenced by changing the feedback resistor R_{14}. The output of the amplifier scales according to Ohm's law

$$U_{\text{out}} = I_{\text{in}} \cdot Z_{\text{trans}}. \tag{3.1}$$

Details can be found in the documentation [40]. The readout scheme for the LGAD board in this work is sketched in Figure 3.3. For some measurements two LGAD boards were also modified to bypass the onboard amplification and enable a direct readout of the signal with an external amplifier. This way it just acts as a holder for the sensors, similar to the ceramic boards. Figure 3.2 shows this configuration of the board with a SiC sensor.

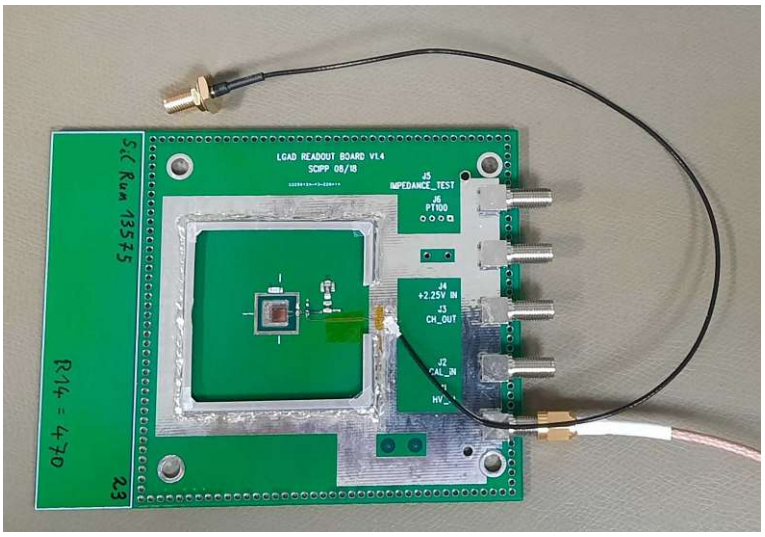

Figure 3.2.: The UCSC LGAD board with a SiC sensor. The TIA is bypassed in this version to provide a direct readout of the detector signal for external amplification. The bias voltage is still supplied by the board.

3.2.2. Broadband Amplification

The second type of readout used for this work employs a fast BB amplifier which directly amplifies the signal and passes it to the DAQ system, ideally without interfering with the pulse shape. This way the integrated signal is proportional to the number of produced electron-hole pairs (and the deposited energy in the detector), as indicated in Figure 3.6 for a single SiC peak. The Cividec C2-HV (C2HV0248) is a non-inverting general purpose current amplifier with a bandwidth of 1 MHz - 2 GHz and a gain of about 40 dB. It is optimized for particle detection purposes as it is a comparatively fast amplifier with a rise time below 1 ns. It features a bias tee, allowing for simultaneously supplying the bias voltage to the detector and reading out the signal with a single cable connection. Figure 3.3 shows the BB readout chain for this work.

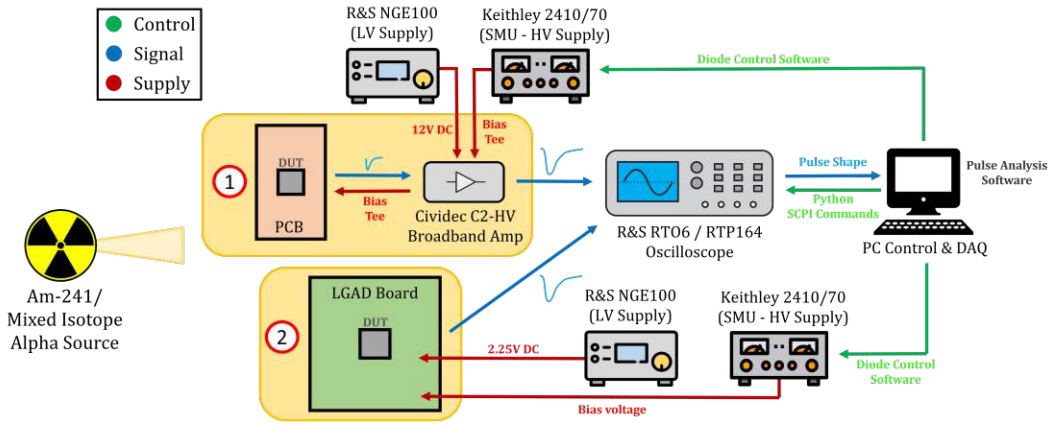

Figure 3.3.: Readout chain using the BB amplifier (1) or the LGAD board (2)

3.2.3. Spectroscopic Readout

Finally, a spectroscopic readout chain was also employed. In this mode, the sensor signal is fed into a shaping amplifier which integrates over a given time period and yields characteristic pulses of a consistent length and shape. As the height of the pulses is directly proportional to the integrated charge, these amplifiers are referred to as Charge Sensitive Amplifier (CSA). The amplifier signal can be digitized by either an oscilloscope or a Multi Channel Analyzer (MCA). An MCA can measure the pulse height with high accuracy and stores the results in a pulse-height histogram (i.e. a spectrum). The shaping amplifier used in this work is a Cividec Cx-L (CxL0192). It is optimized for high precision spectroscopy and integrates a signal current into pulses with a FWHM of 1.65 µs. A typical waveform is shown in Figure 3.5. The Cx-L is an inverting CSA with a gain of 12.21 mV/fC at 0 F input load. The output signal is linear up to a maximum of 2 V. The amplifier also features a bias tee similar to the BB amplifier. Figure 3.4 shows a schematic of the spectroscopic readout chain devised for this work.

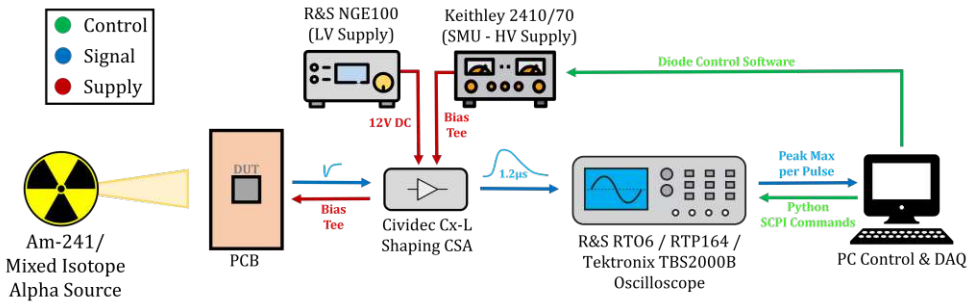

Figure 3.4.: Readout chain using the shaping amplifier (CSA)

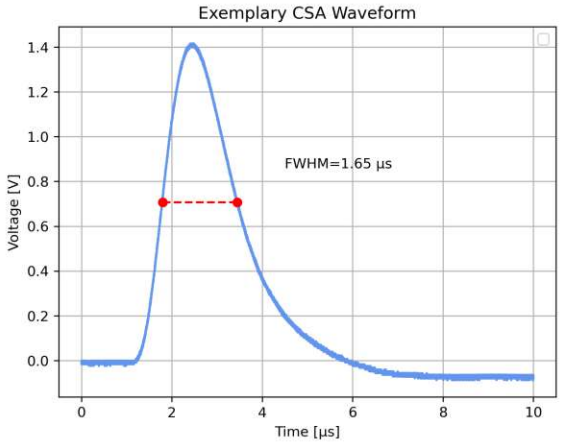

Figure 3.5.: An example of a waveform from the Cividec Cx-L shaping CSA. The peak height is a direct measure of the charge at the amplifier input.

3.3. Data Analysis

3.3.1. Broadband and LGAD Board Measurements

After acquiring data of a BB or LGAD board measurement run, further analysis was carried out offline using a Python based peak analysis software developed at HEPHY [41]. It is able to read several oscilloscope and simulated data formats and analyze each recorded event. The code performs a peak search, separates signal from noise and analyzes each peak. For every event, the

- Peak maximum [mV]
- Peak area [Vs]
- Time over Threshold (ToT) and Time over Noise (ToN) [ns]
- SNR [dB]

and other quantities are determined. Thresholds, a Constant Fraction Discrimination (CFD) factor and different ranges can be set manually to obtain optimal results. Figure 3.6 shows an example of a SiC peak analyzed by the software. The collected data is pooled into a histogram format for further evaluation and plotting. The program also allows a ramp evaluation for some parameters.

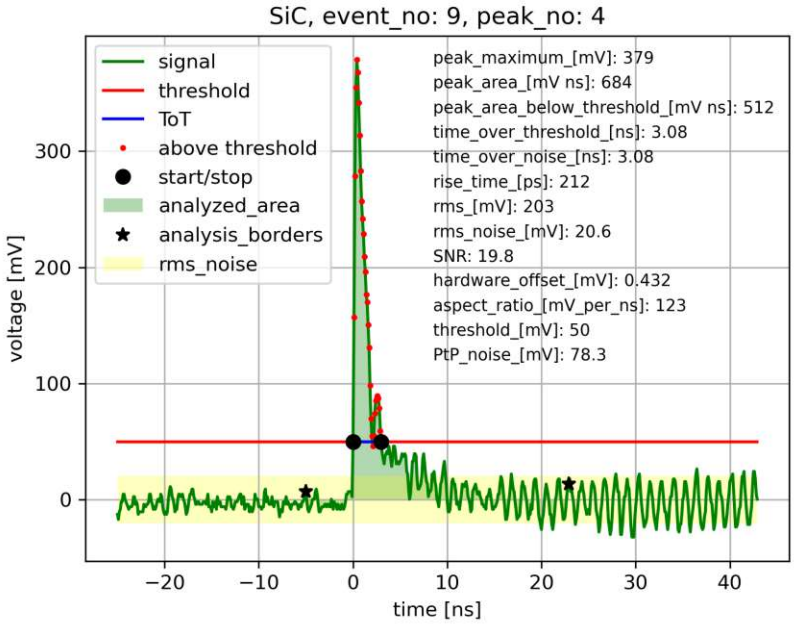

Figure 3.6.: Screenshot of a SiC measurement with the BB amplifier analyzed with the Peak Analysis Code

3.3.2. Spectroscopic Measurements

Data taken for the spectroscopic measurements could in principle also be analysed using the peak analysis software. However, as only the height of the signals contains relevant information, a measurement of the entire waveform is unnecessary.

Therefore, the peak maximum of every triggered waveform was acquired with a PC communicating with the oscilloscope via Standard Commands for Programmable Instruments (SCPI) commands. A measure for the peak height was determined internally with the oscilloscopes' *Measure* function. A Python script gathers the data and converts it into histograms. This setup mimics the function of a traditional spectroscopic readout chain with a charge sensitive pre-amplifier followed by a shaping amplifier and an MCA.

As the signals from the CSA are quite slow ($\sim$ µs, see Figure 3.5), the energy spectrum can already be obtained by using a low-bandwidth oscilloscope, such as the TBS2204B. A distinct resolution of different alpha peaks was possible with the Tektronix TBS2204B at atmospheric pressure. The limitation of lower-end oscilloscopes, is however, the limited resolution (most often an 8 bit ADC is used) and the dead time between acquisitions.

The long integration time of the shaping amplifier leads to a far better SNR compared to the fast BB amplifier and TIA. However, the linearity of the amplification is a limiting factor for very large signals, and changing with different input capacitances. Alpha particles of about 5.5 MeV produce a total signal charge of

$$Q_S^{\mathrm{Si}} = \frac{5.5\,\mathrm{MeV}}{3.62\,\mathrm{eV}} \cdot 1.6 \cdot 10^{-4}\ \mathrm{fC} \approx 240\,\mathrm{fC} \tag{3.2}$$

in Si. For SiC it about half that size due to the higher ionization energy between 5 eV to 8 eV, between 110 fC and 175 fC. The Cividec Cx-L was modified by the manufacturer to ensure the linearity for all alpha measurements in SiC performed over the course of this work. Deviations for the Si measurements are discussed in chapter 6.2.2.

3.4. Sensors

Three different types of detectors are compared in this work. Figure 3.7 shows them mounted on the ceramic boards.

Figure 3.7.: The Si, SiC and Si-LGAD samples used in this work

The planar SiC pad sensor used in this project was developed and manufactured at IMB-CNM-CSIC [42] (run number 13575). It features an active SiC layer grown epitaxially on a 4H-SiC substrate. The p-on-n diode has an area of 3×3 mm. The thickness of the active layer is about 50 µm with a resistivity of 20 Ω cm. On top of the activate volume there is an additional metalization layer (1020 nm) consisting of Titanium, Aluminium and Nickel as well as some passivation (SiO_2, Si_3N_4) on its surface. Figure 3.8a shows a cross section of this type of sensor [43, 44].

The Si diode used in this work is also a planar pad sensor without further surface segmentation. It originated in the wafer production for the CMS experiment. The sample is structurally relatively similar to the SiC sample as it also features a similar layer of passivation on top of an Aluminium metalization of roughly the same thickness. This allows to be relatively confident in comparing the two sensors.

The LGAD sensor used in this work was developed by CNM-CSIC as part of the run 9088. It is Si based and has an active thickness of 50 µm on top of a 300 µm silicon-on-insulator substrate. It features a highly doped boron implant near the surface ($1.9 \times 10^{13}\,\mathrm{cm}^{-2}$) acting as the p-type multiplication layer within a high resistivity p-type bulk. It is a single pad diode with an active surface area of 1.3 × 1.3 mm. This area is covered with a metalization layer, while the surroundings have a passivation on the surface. Figure 3.8b shows a cross section of the diode [45].

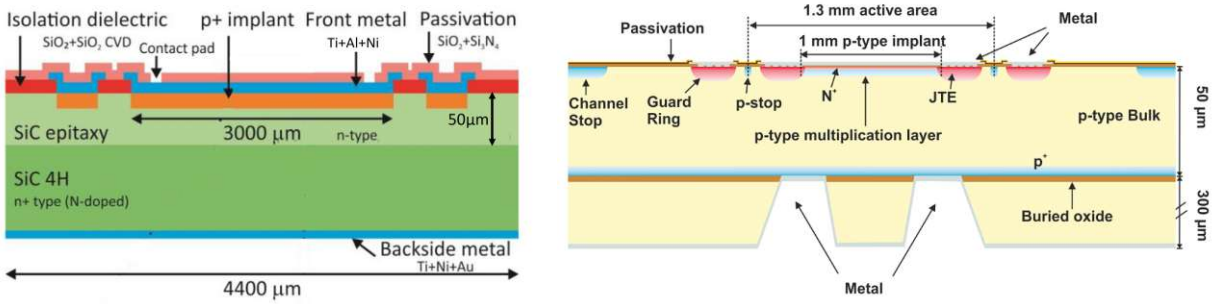

(a) CNM SiC diode

(b) CNM LGAD sensor

Figure 3.8.: Cross section of the SiC used in this project, Adapted from [43], [45]

3.5. Radioactive Sources

Laboratory radioactive sources enable the testing and characterization of detectors without the need for a particle accelerator or other expensive equipment. If the activity is within certain limits, they combine a safe and easy handling with a consistent and reproducible, known output of ionizing radiation. Alpha sources are especially prominent because of their well known, practically monoenergetic spectra and the full absorption of the radiation in matter. This renders them a convenient choice for the calibration of detectors and their associated electronics..

3.5.1. Am-241

Initial measurements were performed using an ^{241}Am source from Eckert & Ziegler with an activity of 9.5 kBq. ^{241}Am is a popular choice for laboratory alpha sources because of its half life of 432.6 years implying no loss in intensity for extended periods. It's alpha decay has three prominent energies, given in Table 3.1 and Figure 2.6 in chapter 2.1.3).

However, the structure of this source is not optimal for high precision or calibration use. The isotope itself is deposited on a 1 µm thick disk with a diameter of 8 mm housed inside a steel collimator. However, the active area is located behind a protective gold layer of 1.4 µm. This Gold layer leads to a significant energy loss and energy straggling before the alpha particles even exit the source. The behavior could be reproduced by GATE simulations in section 5.1.1. The distribution of the alpha energy is broadened to an extent, that the individual decay energies overlap in a single skewed Gaussian. This energy straggling leads to an additional, unnecessary source of uncertainty in measured spectra. An alpha source like this is hence only useful for general testing purposes and not recommended as a calibration device.

Radionuclide	**Alpha Energy [keV]**	**Relative Intensity [%]**
Pu-239	5105.50 (8)	11.94 (7)
	5144.30 (8)	17.11 (14)
	5156.59 (14)	70.77 (14)
		Σ =99.82
Am-241	5388	1.66 (20)
	5443.80	13.10 (3)
	5482.56	84.80 (5)
		Σ =99.56
Cm-241	5762.64	23.10 (10)
	5804.77	76.90 (10)
		Σ =100

Table 3.1.: Relevant alpha energies of the isotopes present in the laboratory sources used in this work. These eight energies constitute the relevant alpha radiation emitted by the three nuclides [46].

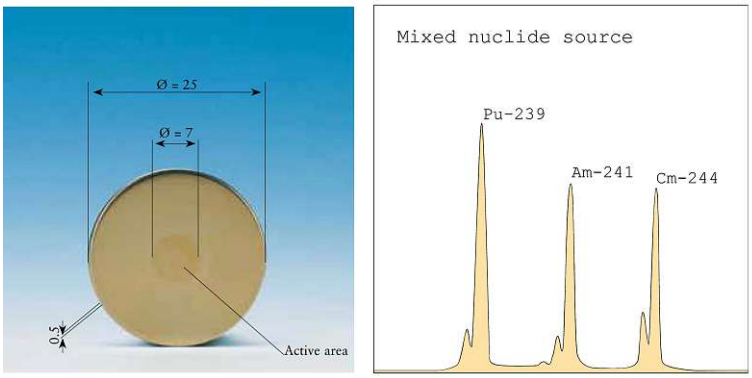

Figure 3.9.: Triple alpha source and the expected spectrum given by the manufacturer [47]

3.5.2. Mixed Isotope Alpha Source

The spectrometric mixed nuclide source (further referred to as *triple alpha source*), an Eckert & Ziegler QCRB25, does not suffer from energy straggling, as it omits any protective layers on top of the active area. According to the manufacturer, sources like these exhibit a line width of less than 20 keV FWHM. The geometry of this source is quite similar to the single isotope one with the active components deposited onto a thin disk with a diameter of 7 mm. A housing similar to the one of the ^{241}Am source was built in-house at HEPHY.

The radionuclides present in the source are ^{239}Pu, ^{241}Am and ^{244}Cm. Their decay energies are almost equidistant (separated by around 320 keV), at 5.157 MeV, 5.483 MeV and 5.805 MeV [46]. Relevant alpha energies are given in Table 3.1. The source has an activity of 1 kBq per isotope.

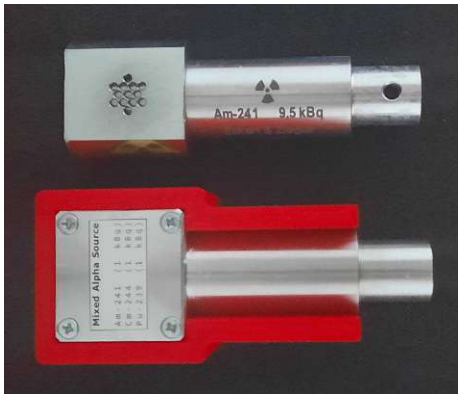

Figure 3.10.: The alpha sources used in this work. The mixed isotope source features a 3D printed cover.

3.6. Monte Carlo Simulations with GATE

Monte Carlo based simulations are a convenient and relatively inexpensive way to model particle transport in matter without the need to build elaborate experimental setups. This is often done as an initial step to get an idea of the properties of a planned experiment,to scan through parameters or as a complementary contribution in the evaluation of data. With Monte Carlo simulations complex geometries and experiments can be approximated by simulating the trajectories of many different particles.

Generally speaking, a simulation tries to calculate the expectation value $\langle x \rangle$ of a randomly distributed parameter x with a given probability distribution $p(x)$ over the whole of the parameter space

$$\langle x \rangle = \int_0^\infty x \cdot p(x) dx. \tag{3.3}$$

Of course the number of interactions and mechanisms is a finite property in a actual simulation. A particle traversing matter is subject to a small number of individual interaction mechanisms with given respective possibilities (more precisely *cross sections*) $p_1, ..., p_n$. The probabilities are normalized to give $\sum_n p_i = 1$ and a total cross section p per interaction.

With an ideally truly random algorithm (independent and evenly distributed) a random number x is generated between 0 and 1. It acts as the seed for one interaction at a time to generate small contributions $x_i = p(x)$. Eventually this converges to give a mean value

$$\overline{x} = \frac{1}{n} \sum_{i=1}^{n} x_i \tag{3.4}$$

for the expected outcome of all interactions.

GATE [16] (*Geant4 Application for Emission Tomography*) is an open source program based on the Geant4 [48] toolkit. It uses Monte Carlo algorithms to simulate particle passage through arbitrary geometries and quantify their interactions. Although being developed mainly for radiotherapy purposes (such as emission tomography and computer tomography), it is also used by the particle physics community.

Its main advantage is the user friendliness compared to lower level Monte Carlo applications like MCNP or Geant4. This is achieved through a *user layer* using human readable scripts called *macros*.

There is a number of predefined physics models and digitization techniques which can be used. The minimum requirements for a simulation are:

- a definition of the beam geometry, type of source and spectrum
- a definition of the phantom (i.e. target) geometry

- a specification of the simulation output (including setting up digitization and detectors)
- a setup of the required physics

There are several optional possibilities like introducing time dependence and visualizations. Additionally, *aliases* acting as internal variables for macros can be used, which simplifies parameterized simulations.

3.6.1. GATE Model for this Work

GATE simulations are used in this work to estimate different geometrical effects, such as the protective layers on top of the source, the air between the source and the detector and finally passivation and metalization layers on top of the detector. The geometry is shown in Figure 3.11 and 3.12 and represents the copper box or alpha holder with a PCB (green), and a SiC detector (pink). The alpha source is modeled as a flat disk emitting particles through a collimator (yellow).

The source geometry can be changed to take the Gold protection layer covering the active disc of the ^{241}Am source into account. The sensor is modelled as a slab of SiC with passivation and metalization layers on top according to [43] (see also Figure 3.8a). Between the leading edge of the source collimator and the PCB surface there is an air gap of 5.2 mm. The height and opening radius of the collimator can be adjusted to simulate the two different alpha sources.

In order to investigate the effect of the air gap between the source and detector, simulations at different air pressures were performed. GATE does not provide pressure as a parameter by default. However, pressure ramps were achieved by adding new entries for air at different densities to the *materials database*. A Python script was written which can add entries to the materials database "on-the-fly". The density ρ of air at a given pressure p is calculated according to the ideal gas law at $T = 20°$

$$\rho = \frac{pM}{RT}, \tag{3.5}$$

where M is the molar mass and R the universal gas constant.

The simulations quantify the energy deposition in the sensor volume. In order to ensure sufficient statistical significance, the simulations were run for 500k primary particles each. These simulations quantify the energy loss in the air gap and the layers on top of the detector, and can be used to calibrate the measured signals to an energy in MeV.

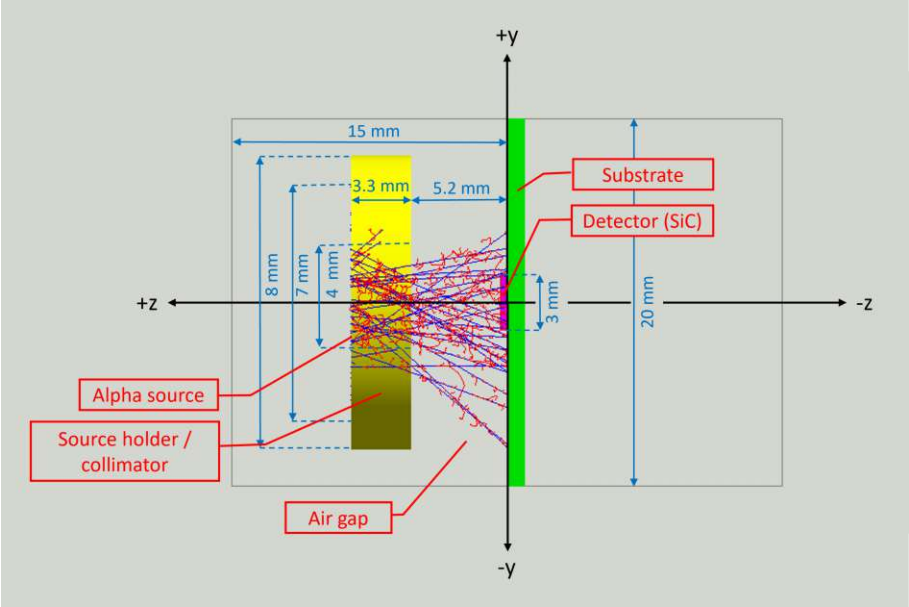

Figure 3.11.: The geometry of the GATE simulations. The dimensions are indicated for the ^{241}Am source here. The triple alpha source collimator is only about 1 mm high instead of 3.3 mm.

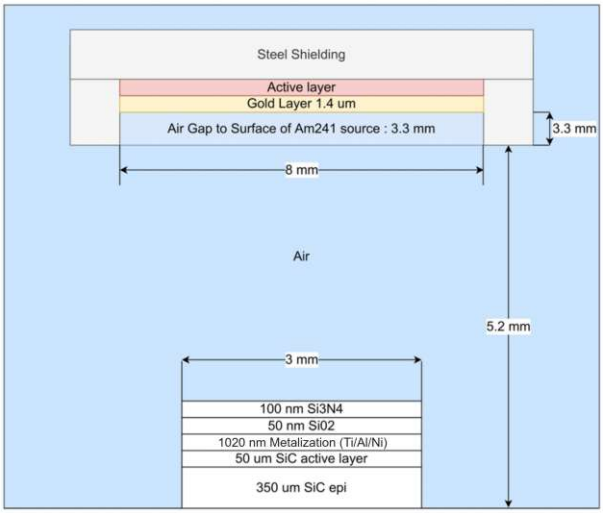

Figure 3.12.: Detail of the layer structure in the GATE model. The dimensions are again indicated for the ^{241}Am source. The triple alpha source does not feature the protective Gold layer and the collimator is a different height.

4. Vacuum Setup

Helping in the conception, design and implementation of a new vacuum setup at HEPHY was a key part of this thesis. This setup was successfully used to perform measurements in low pressure environments. The vacuum pressure can be controlled to any value between 0.3 mbar and ambient pressure desired by the user.

4.1. Design of the Vacuum Setup

The setup consists of a vacuum chamber and a pump mounted on a movable lab bench as well as the electronics needed for the pressure control. The vacuum chamber (Airtech RB451) is cylindrical with a diameter of 30 cm and a height of 46 cm which amounts to an approximate volume of 10 L. This is sufficient to house a detector with a laboratory source or a circuit board and potentially even small amplifiers, cables and further equipment. Figure 4.1 shows the setup located in the module clean room at HEPHY.

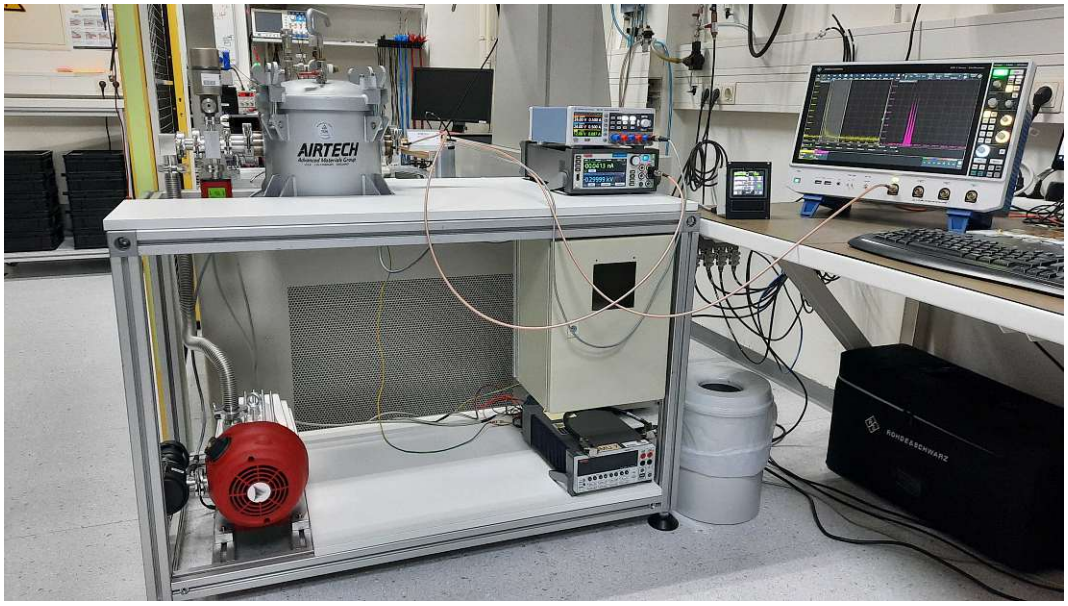

Figure 4.1.: The vacuum setup in operation, measuring alpha spectra at low pressure

A scroll pump (Pfeiffer HiScroll 6) is used to generate a low pressure environment in the tank. Any desired pressure can be achieved by establishing an equilibrium between the suction of the pump and the inflow of air through a venting valve. This is achieved by controlling the setup with a Siemens LOGO!8 Programmable Logic Controller (PLC)

connected to a gas control valve (Pfeiffer EVR 116) and a pressure gauge (Pfeiffer RTP 200 AR). Additionally the pump can be included in the control circuit. For higher pressures, the pumping speed needs to be throttled, as the venting speed of the gas control valve is limited. The PLC is configured to act as a PI-controller making it possible to set and hold any given pressure between 0.3 mbar and ambient pressure for extended periods of time.

A limiting factor in this configuration is the conversion from the analog voltage levels of the gauge and needle valve into the LOGO internal units which have a resolution of only 10 mV (0-10 V = 0-1000 units). As the voltage-to-pressure function of the gauge rises in a logarithmic fashion with $U(p) = 5.5 + \log(p)$ this uncertainty is, however, only an issue for higher pressures above several hundred mbar. In the worst case at ambient pressure (1000 mbar) the unit conversion ($\Delta V = \pm 0.01$) could lead to an uncertainty of about 23 mbar. This is a value comparable to inevitable differences in barometric ambient pressure due to elevation and the weather. For a pressure of 10 mbar the uncertainty measures only half a mbar, which is exceeded by the fluctuations in the PI pressure control.

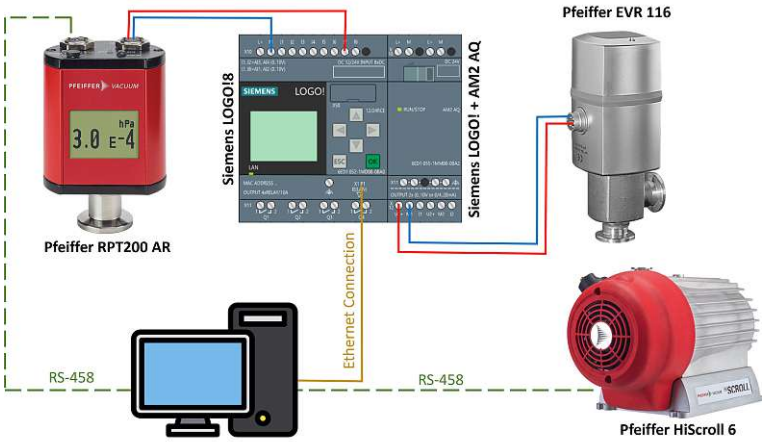

Figure 4.2.: Schematic of the pressure control system. An implementation of the pump and the gauge readout over RS-458 is optional and not yet implemented

4.2. Vacuum Setup Control

The control software is implemented as a combination of a PLC internal program and a Python code running on a PC connected via Ethernet to the PLC. The setup can be extended in the future by a serial RS-458 interface connected to the gauge and the vacuum pump. As of the publication of this work, the RS-458 communication is not yet implemented. A schematic of the communication strategy is shown in Figure 4.2.

The LOGO program is shown in Figure 4.3. It features a PI-controller (B002) comparing an *analog input* receiving from the pressure gauge signal (AI1) and a set point accessed by the PC via an *analog marker* (AM2). The PI-controller output is connected to the *analog out* (AQ1) which is itself connected to the needle valve's analog control. The measured gauge and valve voltages received can be accessed externally via the *analog markers* (AM1) and (AM3).

The Python control software accesses these *analog markers* with the help of the `snap7` library [49] with read-write capability. Conversions from the LOGO internal units to the actual pressure are all performed by the external software. The PLC is only used to keep the currently requested pressure value stable and as a communication device between the analog interfaces of the gauge and valve.

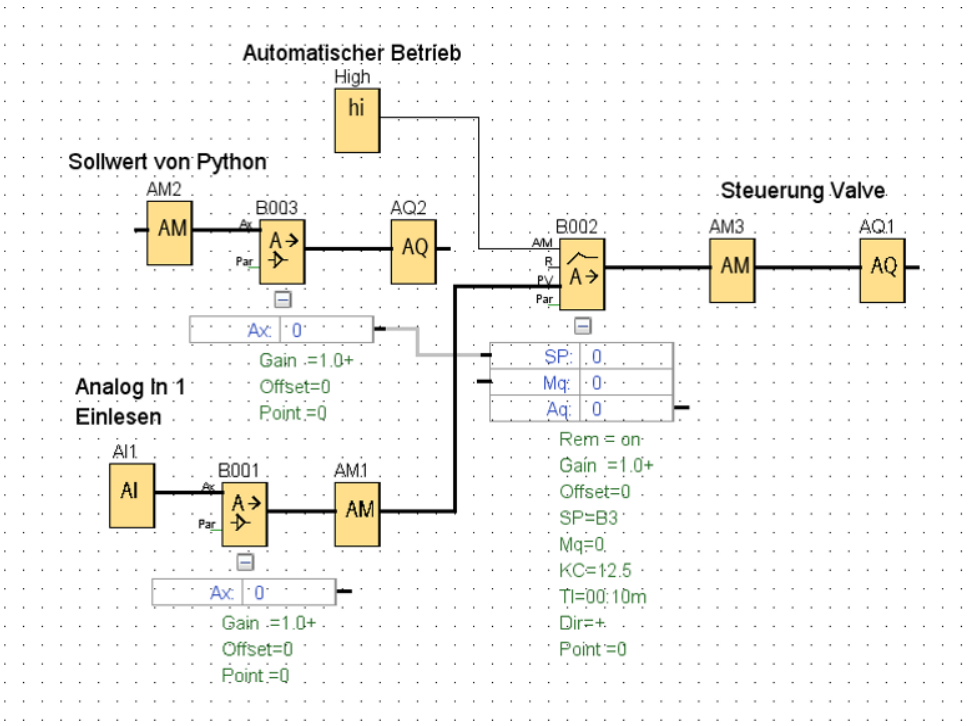

Figure 4.3.: The PI-controller implemented in the PLC

A JSON-RPC (Remote Procedure Call) server [50] was set up within a Python class allow the vacuum control to be integrated into DAQ systems.

The commands are sent as JSON dicts in the generic form

```
{"jsonrpc": "2.0", "method": "<method>", "params": {"param1": "<param1>", "param2":
    "<param2>",...}, "id": 0}
```

Answer strings follow the same structure. As of the publication of this work the available methods are:

- `get_state`, returning the gauge pressure and voltage applied to the needle valve
- `set_pressure`, defining a new set point and starting the pressure control (in mbar)
- `open_valve`, completely opening up the setup and re-pressurizing to ambient pressure
- `close_valve`, complete closing of the needle valve.

A desired pressure value of 100 mbar may, for example, be set by sending the command

```
{"jsonrpc": "2.0", "method": "set_pressure", "params": {"set_press_mbar": 100.0}}
```

to the server. Given the structure of the code, the functionality can be extended in the future to include the vacuum pump or a RS-485 communication with the gauge. The source code of the pressure control in its current state is supplied in B in the appendix.

5. Results of the GATE Simulations

5.1. Simulations for the ^{241}Am Source

5.1.1. Effect of the Gold Protection Layer

In order to quantify the impact of the gold protective layer used in the ^{241}Am source, simulations varying the thickness of this layer were performed. All simulations were done in vacuum, in order to remove the effect of energy straggling in the air gap. The strong impact of the gold protection layer on the energy spectrum in SiC is visualized in Figure 5.1. A dense material such as Gold severely reduces the energy of alpha particles after only a few hundred nm. As the thickness of the layer is increased, the three individual decay energies merge into a continuous distribution, already after a thickness of about 200 nm. The decrease in energy seems to follow a linear progression as evident in Figure 5.2.

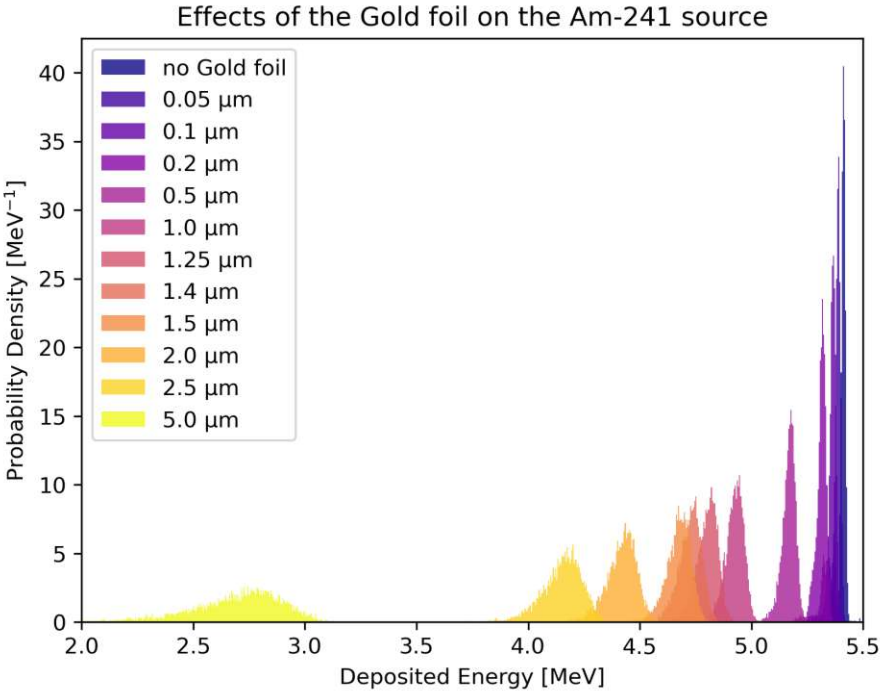

Figure 5.1.: The effect of the Gold layer thickness on the ^{241}Am energy spectrum in vacuum

Even in an absolute vacuum, the mean energy value of the main peak is shifted by 0.67 MeV from 5.41 MeV, without any protective layer, to 4.74 MeV for a Gold layer with a thickness of 1.4 µm as stated by the source manufacturer. This is visualized in Figure 5.3.

The passivation and metalization layers of the detector have a lower effect, reducing the energy by 0.08 MeV. As these layers cannot be removed, they represent an intrinsic limit to the energy resolution of this detector.

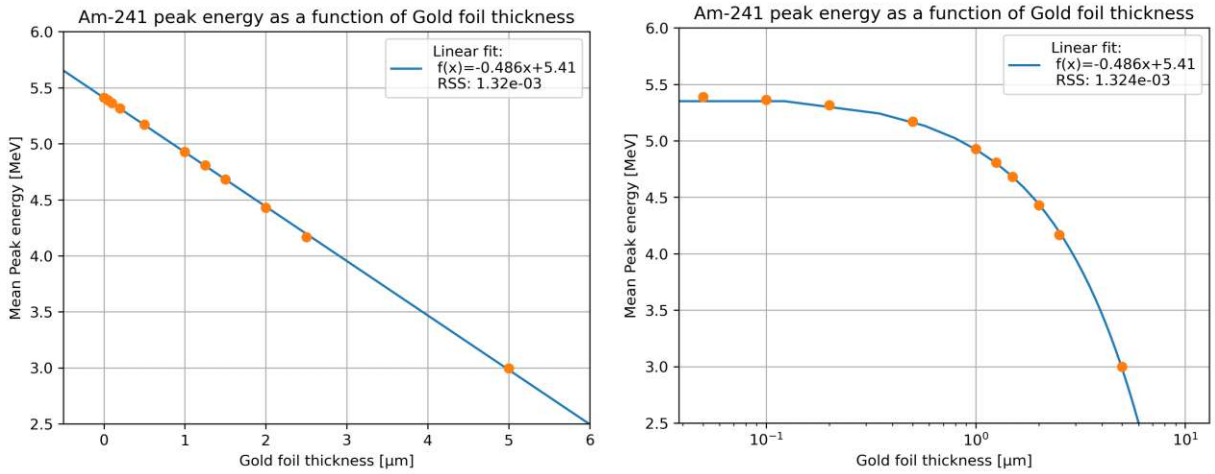

(a) Linear plot (b) Logarithmic plot

Figure 5.2.: Linear dependence of the mean peak energy with Gold layer thickness

As with the ensuing pressure simulations, the simulated energy loss matches the results one would expect according to chapter 2.1.2 and the energy probability distribution follows the progression as hinted at in Figure 2.4. Selected histograms and fit parameters obtained from the simulations can be found in appendix A.1.

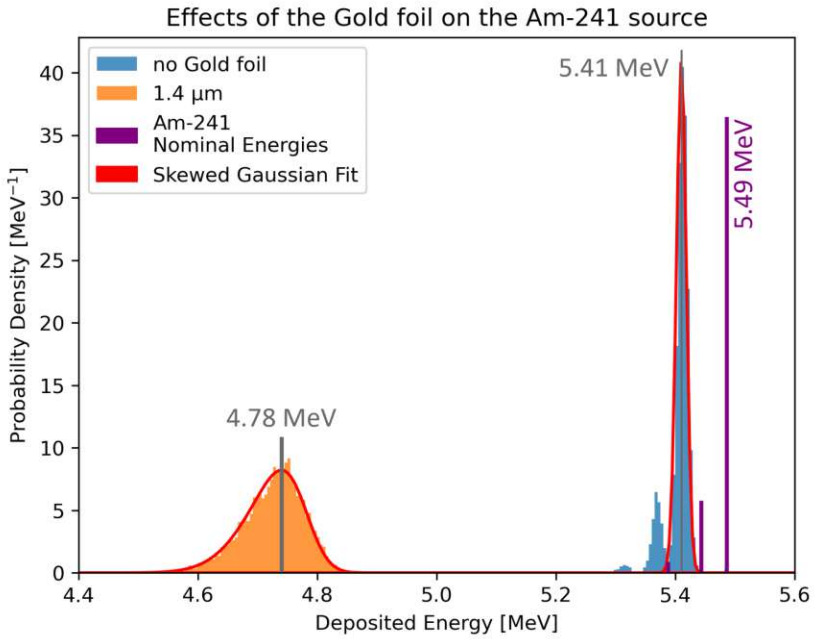

Figure 5.3.: The effect of the 1.4 µm gold layer on the ^{241}Am spectrum in vacuum

5.1.2. Pressure Response

The pressure simulation demonstrates why alpha measurements should be performed under vacuum conditions, if an accurate energy resolution is of concern. In this example only about 8 mm of air at atmospheric pressure lead to an additional energy shift of 0.57 MeV in the ^{241}Am source after the gold layer, almost doubling the peak energy spread. These results are depicted in a logarithmic and a linear pressure ramp in Figure 5.4.

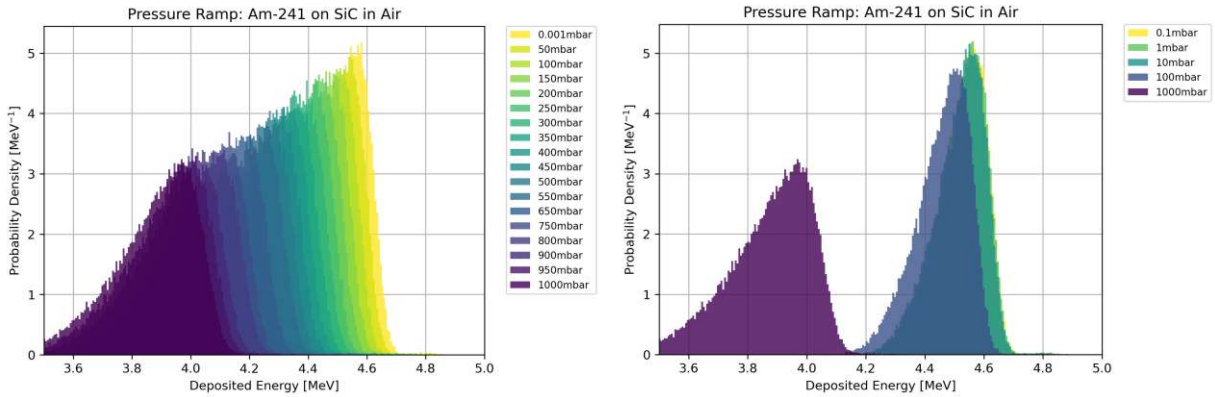

(a) Linear pressure ramp

(b) Logarithmic pressure ramp

Figure 5.4.: Simulated pressure ramps for the ^{241}Am source on SiC

As the air pressure, and hence the density, increases, the alpha particles are subject to a higher number of collisions and consequently lose more energy on their way to the detector. The energy spread is also increasing with pressure due to energy straggling. Both effects seem to follow a linear progression as shown in Figure 5.5 and Figure 5.6. Increasing the pressure basically simulates an increase of the distance the particles travel through the gas.

However, there is a lower boundary to the pressure response. As the density reaches a certain threshold, there seem to be so little collision partners left, that the alpha particles reach the detector basically unimpeded. As evident in the logarithmic plots, the peak energy as well as its spread do not change significantly below a pressure of 100 mbar for the ^{241}Am source. From an experimental standpoint, this is good news, as vacuum pressures as low as these are easily reached within the vacuum setup devised for this work. Detailed results and plots are again given in the appendix in A.2.

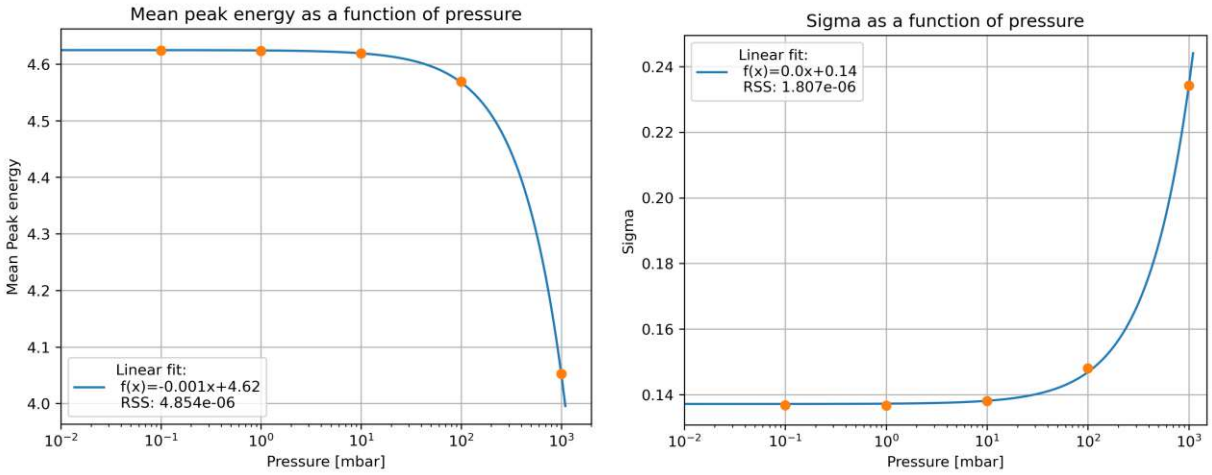

(a) Mean energy as a function of pressure (b) Width of energy distribution as a function of pressure

Figure 5.5.: Mean and distribution width of energy as a function of pressure for the ^{241}Am source (logarithmic pressure ramp)

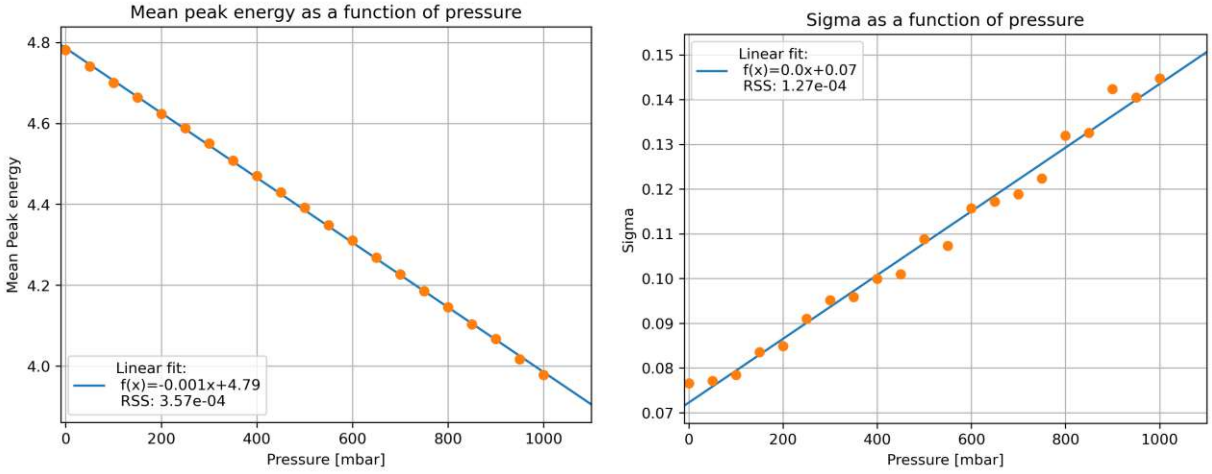

(a) Mean energy as a function of pressure (b) Width of energy distribution as a function of pressure

Figure 5.6.: Mean and distribution width of energy as a function of pressure for the ^{241}Am source (linear pressure ramp)

5.2. Triple Alpha Source

The main goal of these simulations was to observe the broadening of all three decay energies with increasing pressure and investigate up to which pressure the individual energies can still be resolved. As to be observed in Figure 5.7b, the main peaks are separated, even at ambient pressure. The following simulations were performed with the respective dimensions of the triple alpha source (collimator height 1 mm). It was however noted by accident, that a visible difference due to 2 mm of difference in air gap does not emerge up until a pressure of about 250 mbar. This corresponds to the pressure independent nature of the spectra below a pressure of 100 mbar.

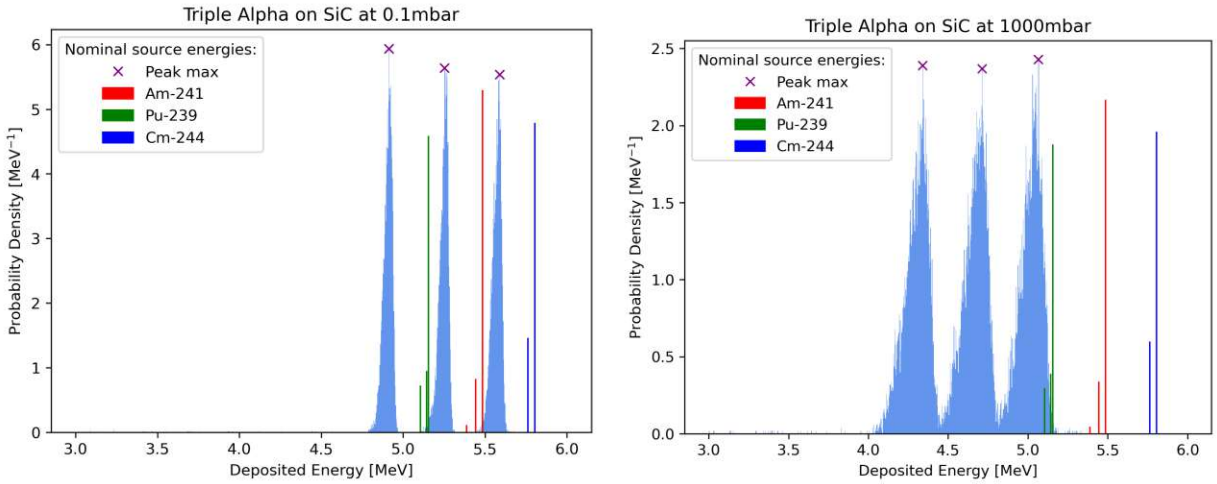

(a) Spectrum at 0.1 mbar (b) Spectrum at 1000 mbar

Figure 5.7.: Spectra of the triple alpha source at different pressures in SiC

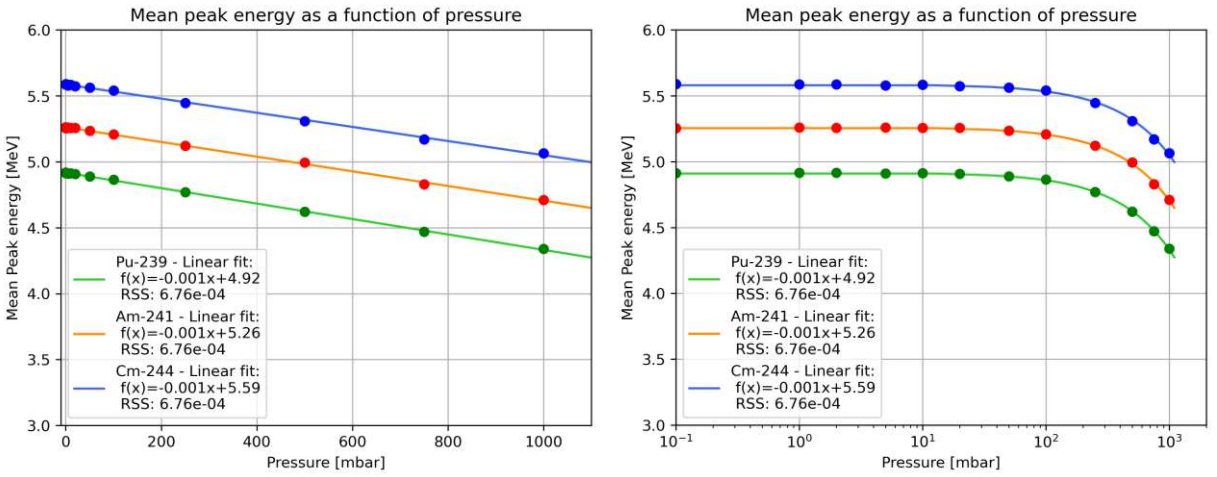

(a) Mean energy as a function of pressure (b) Mean energy as a function of pressure

Figure 5.8.: Mean peak energies as a function of pressure for the triple alpha source

Figure 5.8 shows the same linear scaling of the three main decay energies observed for the single isotope source with pressure in air or distance in Gold (chapter 5.1). There is again a plateau below a pressure of 100 mbar and the energy loss behavior does not change significantly from this point on. Another interesting aspect is indicated in Figure 5.9: The relative distances between the peaks also seem to decrease in a roughly linear fashion. Stated another way, this means the three peaks scale together and can be used for the calibration of the measurement or to determine the amplifier linearity at any given pressure. Selected plots for each simulations are given in the appendix in A.3.

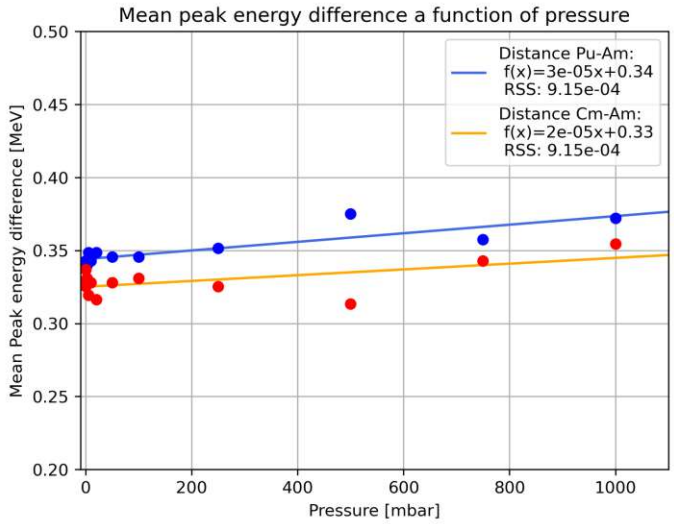

Figure 5.9.: Relative distance of the triple alpha peaks as a function of pressure. Deviations can be attributed to the fit uncertainties.

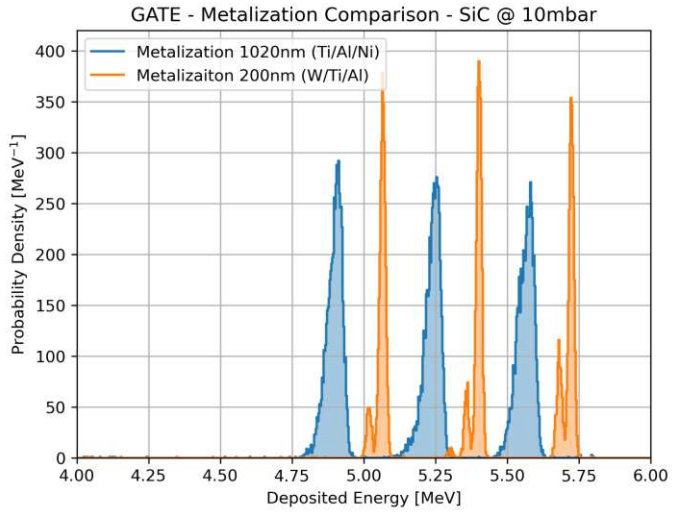

Figure 5.10.: The effect of the metalization layer of the SiC detector on the triple alpha spectrum at 10 mbar

Incidentally, the effect of the metalization layer on the spectra was also probed as the initial GATE simulations featured a faulty geometry of only 200 nm of a Tungsten, Titanium and Aluminium layer as opposed to the actual 1020 nm of Titanium, Aluminium and Nickel for the SiC diode used in this work. With the thinner metalization, the substructure of the alpha peaks can even be resolved at low pressures. The energy straggling and losses are clearly reduced as evident in Figure 5.10. This means, that if one is interested in resolving this substructure in alpha spectra, not only a good vacuum (below 10 mbar) but also a sensor with as little surface coating covering the active volume as possible is needed.

6. Results of the Alpha Measurements

The ^{241}Am and triple alpha spectra were measured in a reproducible fashion at arbitrary pressures with a number of different combinations of readout electronics. These measurements may serve as an important tool for future energy calibration and sensor characterization. The measured energy distributions are reproducible with GATE simulations to a satisfying degree.

This section entails a brief summary of the experimental observations and evaluations for the alpha measurements performed over the course of this work. The Si and SiC detectors were biased with 300 V, while the LGAD was biased with 50 V for all measurements to ensure consistent results. The measurements were performed in the new vacuum setup under similar conditions, concerning the cabling and electronics. All broad-band BB and spectroscopic measurements were performed with the diodes on ceramic boards, with the exception of the triple alpha BB measurements of SiC, which were taken with the bypassed version of the LGAD board. All spectra shown are normalized density functions. Within a given plot, the binning of all histograms is consistent.

6.1. Measurement of the ^{241}Am Source

As expected, the energy distributions of the ^{241}Am source closely match skewed Gaussians for both the BB and spectroscopic measurements. Already in the first BB measurements a trend could be observed, which could be confirmed in further measurements: Due to the higher electronic noise contribution associated with the fast amplification of the Cividec C2-HV, the expected narrowing of the energy distribution due to the vacuum does not translate to the BB spectra. Figure 6.1 and 6.2 show comparisons between the simulated GATE results for the ^{241}Am source and corresponding BB and spectroscopic measurements. The energy axes were linearly scaled to the mean peak energy determined with the simulations.

It can be clearly seen in direct comparison, that the spread of the energy distribution measured with the BB amplifier is far bigger than the spectroscopic one and its width does not significantly change with pressure. The spectroscopic measurements fit the GATE simulations very well, taking into account the exact source geometry and the energy straggling and loss due to the gold layer. The remaining mismatch can be explained by the uncertainty in the gold layer thickness, which is given with as 0.4 µm by the manufacturer.

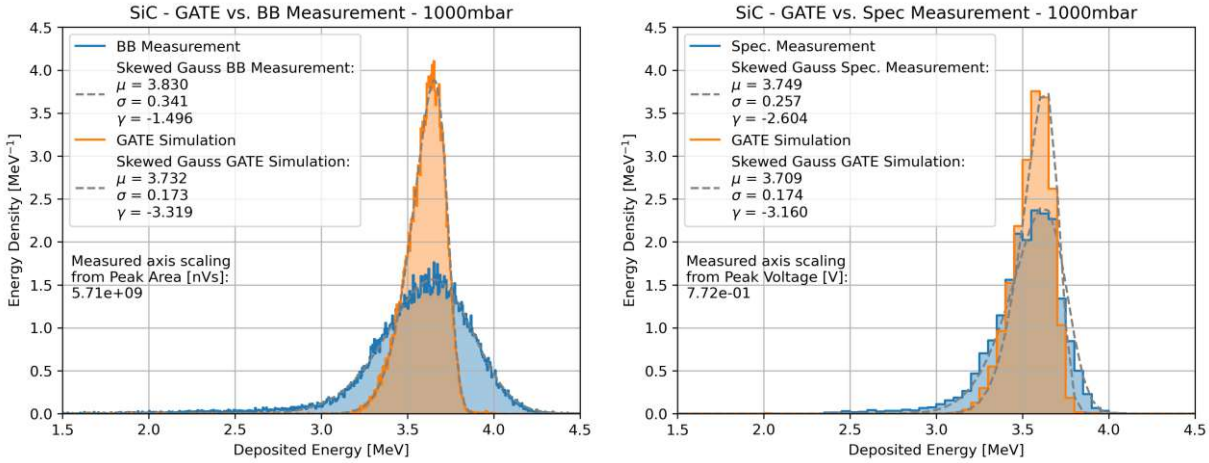

(a) GATE vs. BB measurement (b) GATE vs. spectroscopic measurement

Figure 6.1.: ^{241}Am spectra taken with the BB and spectroscopic readout chain compared to the corresponding GATE simulation (1000 mbar, SiC)

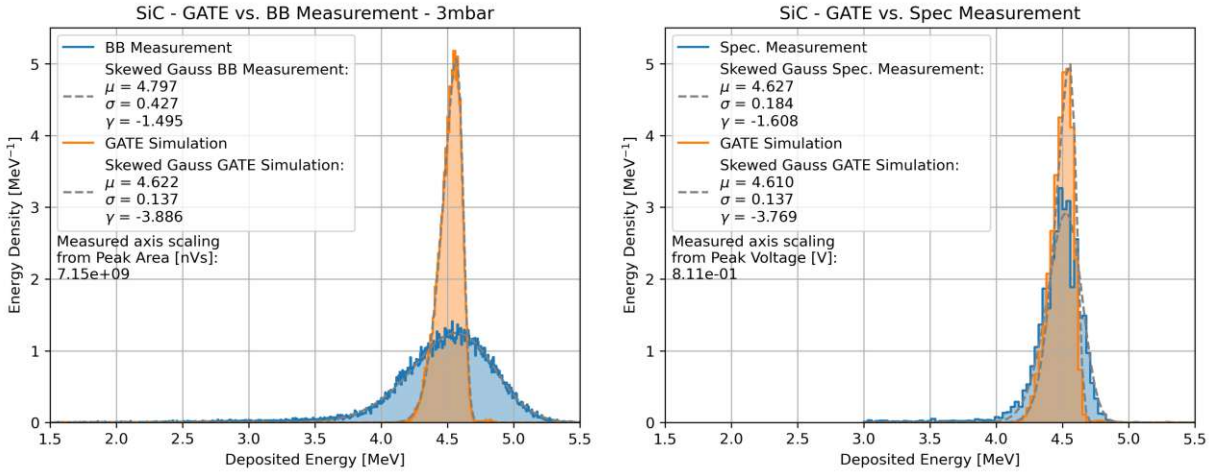

(a) GATE vs. BB measurement (b) GATE vs. spectroscopic measurement

Figure 6.2.: ^{241}Am spectra taken with the BB and spectroscopic readout chain compared to the corresponding GATE simulation (3 mbar, SiC)

6.1.1. Pressure Response

A set of pressure dependent spectra of ^{241}Am was collected with a lower resolution oscilloscope as an initial test of the spectroscopic readout and analysis. Although the Tektronix TBS2204B only features an 8 bit vertical resolution, it was accurate enough to infer the linear behavior in both the mean energy of the distributions and their width (see Figure 6.4). Figure 6.3 shows an example peak for SiC at low pressure next to a combined plot of the pressure ramp.

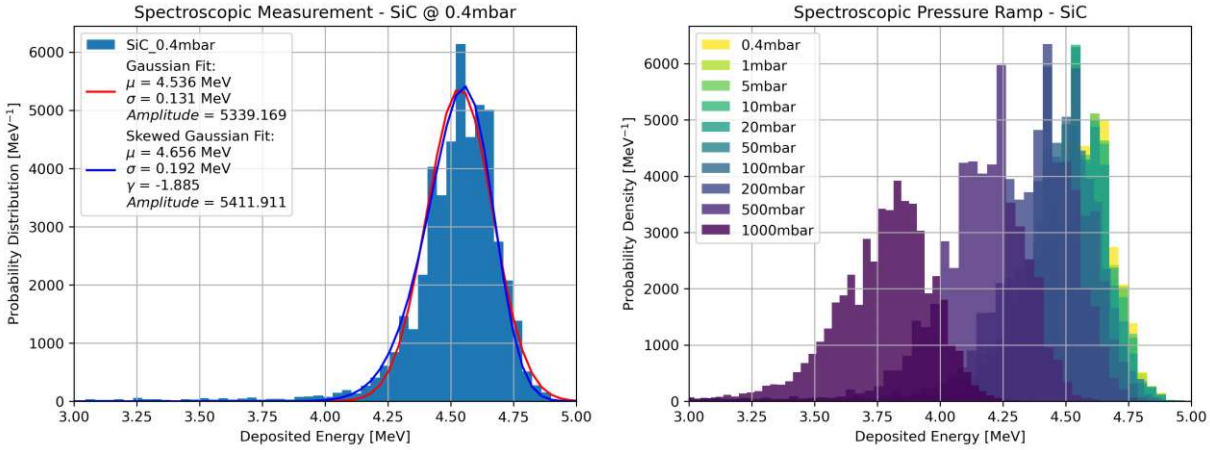

(a) Example spectrum of ^{241}Am on SiC (b) Spectroscopic pressure ramp in SiC

Figure 6.3.: An example spectrum of ^{241}Am on SiC at 0.4 mbar next to a combined plot of the pressure ramp

The energy axes were again scaled with a linear factor (determined as an average for all data sets) according to the GATE simulation. The measured spectra seem broader than the simulated ones in this plot (compared to Figure 5.4). This is however just a binning artefact and results from the low vertical resolution of the oscilloscope (as evident in Figure 6.1 and 6.2, when applying the same binning). As observed in the simulations previously, the spectra no longer change their shape significantly below 100 mbar. The same behavior could be observed for Si (see Figure C.1 in the appendix).

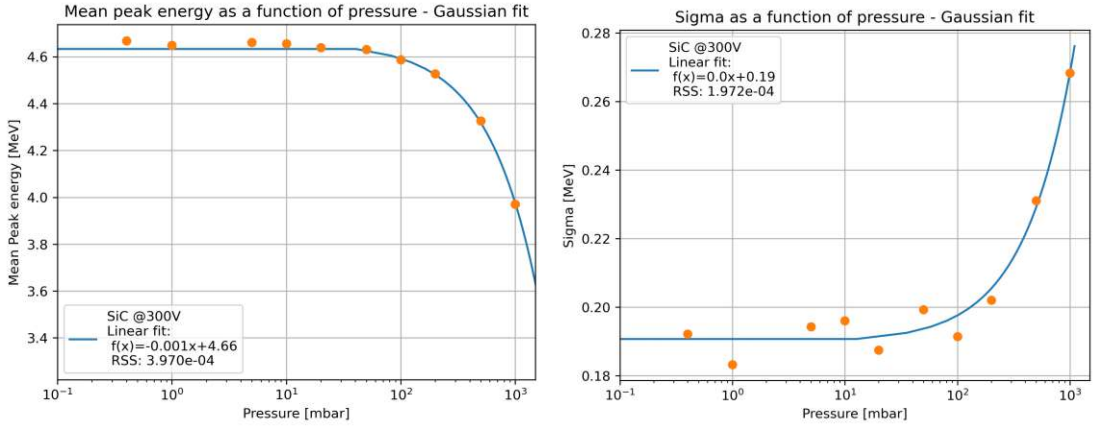

(a) Mean energy against pressure (b) Spectrum width against pressure

Figure 6.4.: Linear pressure dependence of the ^{241}Am energy distribution

6.2. Measurement of the Triple Alpha Source

The measured spectra of the triple alpha source are consistent with the GATE simulations. In all three modes of acquisition (Spectroscopic, BB and LGAD board TIA) and at any pressure, the three decay energies are clearly separated and can be used for energy calibration. However, there are considerable qualitative differences, as evident in Figure 6.5, which are discussed in chapter 6.2.2.

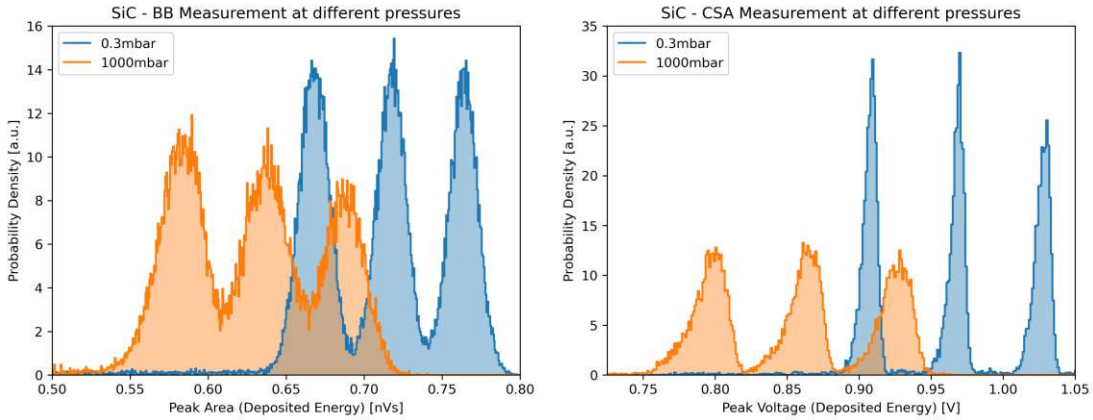

(a) SiC BB spectra

(b) SiC CSA spectra

Figure 6.5.: BB and CSA spectra of SiC in vacuum and at ambient pressure (energy axes not scaled)

6.2.1. Pressure Response

The linear pressure dependence of the deposited energy (or the energy loss of the alphas in air) could again be replicated for the triple alpha source both in Si and SiC over the course of several measurements. The broadening of the spectra with increasing pressure was observed for the spectroscopic measurements, whereas for the BB measurements, the electronic noise again dominates the spectra rendering the transition not as pronounced. The same shift of the mean peak energies can be observed for both methods.

Figure 6.6a shows the linear pressure dependence of the mean peak energies for SiC. A similar result could be achieved for Si (see Figure C.2 in the appendix). Figure 6.6b shows the pressure dependence of the peak widths for both the spectroscopic Si and SiC measurements. The width was determined as the FWHM of the peaks via skewed Gaussian fits. With the high resolution of the spectra, the behavior is no longer linear, but nevertheless, shows the same trend of broadening with increasing pressure. The figure shows the individual FWHM together with the average values for Si and SiC, the dotted exponential fits are just a guide to the eye. The spectra have been linearly scaled to match the GATE simulations. Plots for the full pressure ramp in SiC can be found in the appendix in Figure C.3, Figure 6.5 shows BB and CSA measurements of SiC at 0.3 mbar and ambient pressure.

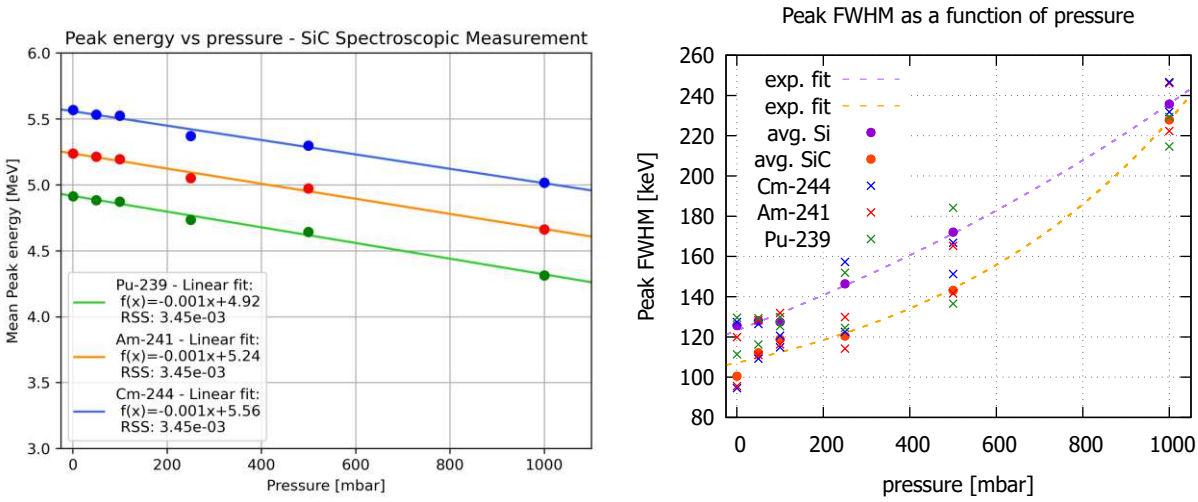

(a) Mean energy as a function of pressure (SiC) (b) Width of energy distribution as a function of pressure (Si and SiC)

Figure 6.6.: Mean and distribution FHWM of energy as a function of pressure for the spectroscopic measurements. The FWHM was determined via skewed Gaussian fits for both Si and SiC. The energy axes were scaled to match GATE simulations.

6.2.2. Electronics and Sensor Comparison

Qualitatively, the spectra differentiate mainly in the broadening of the peaks due to electronic noise. From a number of independent measurements it could be concluded, that the spectroscopic readout has a far lower noise contribution, which is negligible compared to the energy straggling in the passivation and metalization layers of the detector. For the BB measurements, a reduction in the air pressure does not lead to significant advantages in the resolution, as the peak broadening can be mainly attributed to the electronic rather than energy straggling in air. Nevertheless, the uncertainties in the mean energy associated with a varying source-detector distance can be prohibited by performing the measurements in a vacuum.

Using the HD mode on the Rhode & Schwarz oscilloscopes it is possible to collect high resolution spectra with the Cividec Cx-L. An example measured with the 16 bit ADC of the RTP164 is shown in Figure 6.7 for SiC at ambient pressure. This configuration allows for an energy resolution of around 400 eV and can compete with a traditional spectroscopic readout chain using a high precision MCA as a digitizer. As seen in Figure 6.8 and 6.9 the noise in the spectroscopic readout is very low because of the long integration time of the amplifier. For SiC and Si at a pressure of 0.3 mbar, an averaged FWHM of the individual peaks of 100 keV could be observed. At ambient pressure, the peaks broaden to a FWHM of about 220 keV (see Figure 6.6b).

When measuring highly ionizing radiation, such as alpha particles, with Si or other detectors with lower ionization energies, one has to be careful when using the spectroscopic readout chain. As the linearity of its gain is only assured up to an output voltage of 2 V, spectra may be deformed for large energy depositions. This effect and a possible workaround are addressed in the next chapter 7 and in the appendix at D.

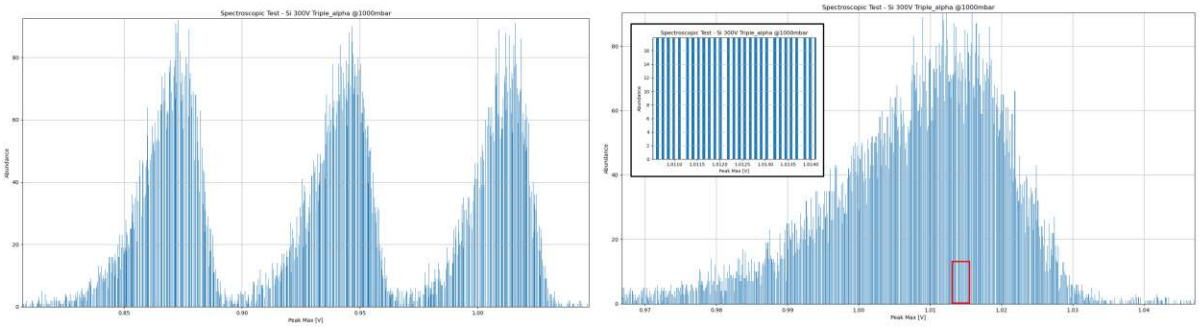

Figure 6.7.: Spectroscopic measurement of the triple alpha spectrum on SiC at ambient pressure. The detail on the right side shows the highest decay energy peak and a detail of the resolution limit ($\sim$ 0.1 mV), which in this case amounts to roughly 400 eV of deposited energy.

With the high bandwidth of the BB amplifier, the true signal waveform from the detector is preserved with high accuracy. With a sufficient sample rate, a high resolution on the integrated signal area can be achieved. However, due to the fast amplification, there is also a lot of electronic noise polluting the measurements and the separation of the three triple alpha peaks is by far not as pronounced as it can be achieved with the CSA. The LGAD board TIA suffers from the same problem and turned out to be even more susceptible to electronic noise in the measurements taken for this work, see Figure 6.10.

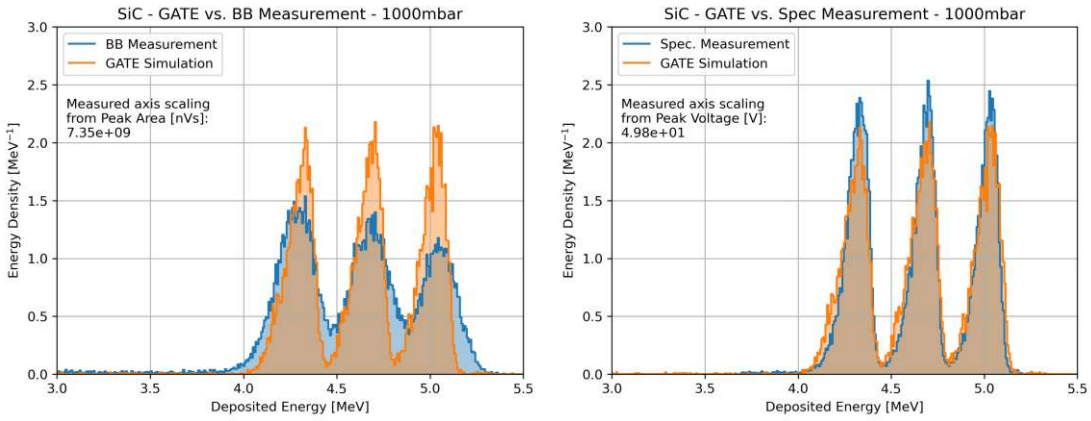

(a) GATE vs. BB measurement (b) GATE vs. spectroscopic measurement

Figure 6.8.: Triple alpha energy spectrum taken with the BB and spectroscopic readout chains compared to the corresponding GATE simulation (0.3 mbar, SiC).

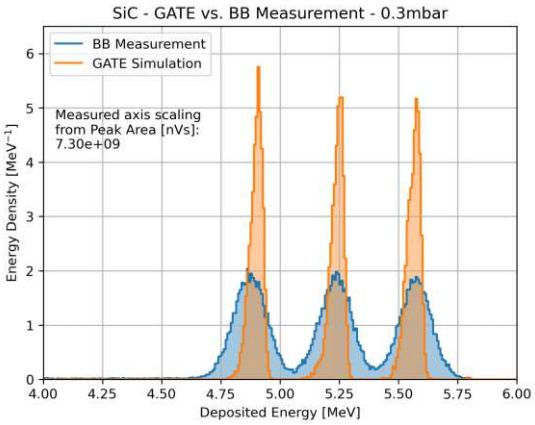

(a) GATE vs. BB measurement

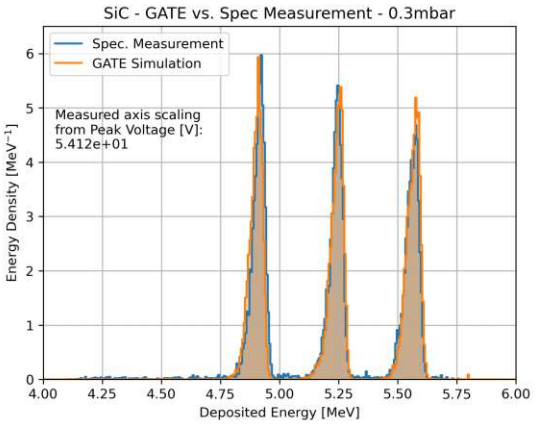

(b) GATE vs. spectroscopic measurement

Figure 6.9.: Triple alpha energy spectrum taken with the BB and spectroscopic readout chains compared to the corresponding GATE simulation (around 0.3 mbar, SiC).

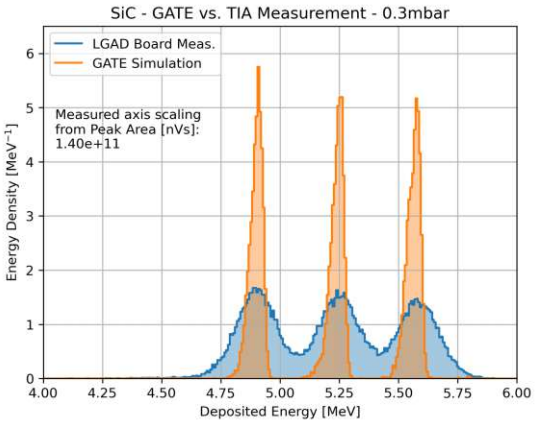

(a) GATE vs. TIA measurement

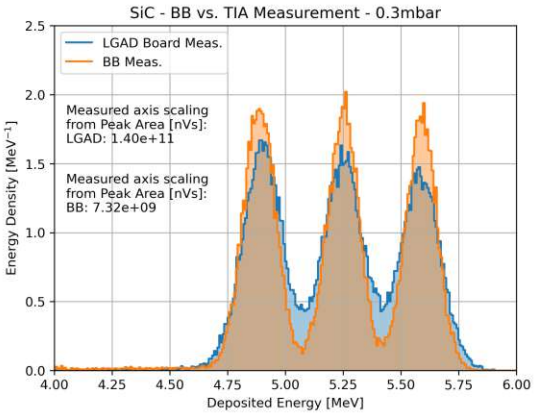

(b) BB vs. TIA measurement

Figure 6.10.: Triple alpha energy spectrum taken with the LGAD board readout chain compared to the corresponding GATE simulation (1000 mbar, SiC). The right figure shows a direct comparison of the TIA and BB measurement.

Both the CSA and BB amplifier inputs are are very susceptible to noise pickup. In order to guarantee successful measurements, great care has to be taken to properly shield the detectors and PCBs from any RF and HF noise.

Measurements using the three detectors under similar conditions were also compared to each other. The Si spectra have to be scaled down due to the difference in the produced charge, rendering both the measured peak areas in the BB measurement and the CSA voltages approximately double the size of SiC. The scaling factor can be determined as the ratio of their ionization energies (more on that in the next chapter 7). For the Si-LGAD with the additional internal gain, a scaling factor was determined visually from the spectra.

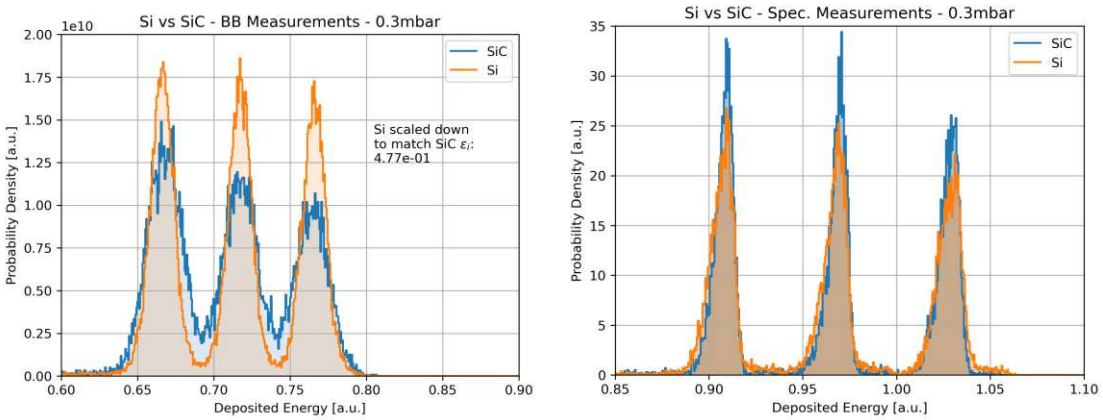

(a) BB readout chain (b) Spectroscopic measurements

Figure 6.11.: Comparison of the Si, SiC and LGAD measurements using the same readout chains.

As to be seen in Figure 6.11b, the Si and SiC spectrum taken with the spectroscopic readout chain look very similar an can be scaled to each other with a single factor. The original Si CSA spectrum was re-scaled to compensate for the non-linearity in the amplifier gain function, as determined in the appendix D.

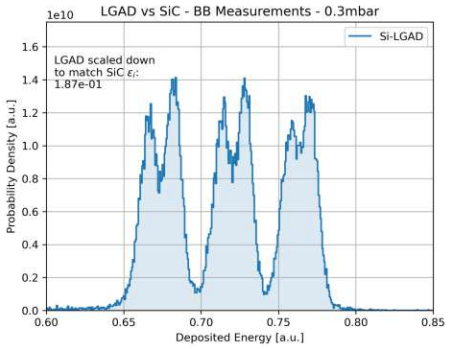

Figure 6.12.: Si-LGAD BB measurement at 0.3 mbar.

For the BB spectra, the original SNR for the different detectors differ, which results in narrower peak widths for larger signals after rescaling, see Figure 6.11a. The energy distributions of the LGAD detector measured in vacuum show an additional feature (Figure 6.12). Due to the surface structure featuring both an area of metalization and a passivation surrounding it (see figure 3.8b), a pattern of double peaks emerges. This is due to the different paths alpha particles take through the surface structure and the differences in energy loss. With increasing pressures, the effect blurs out and a single broadened spectrum is measured. At low pressures, scaling the LGAD spectra to Si or SiC is not possible with a single factor, as it is unclear which set of peaks to base it on.

For measurements of low intensity sources under standard laboratory conditions, the advantages of SiC over Si are not yet apparent in these comparisons. Since neither a high time resolution is necessary (pile-up is not a concern) nor radiation damage or high temperatures cause problems in this configuration, the results for both detectors are very similar. However, this is good news, as the performance of SiC can directly be compared to the well known characteristics of Si detectors this way. This could be especially interesting for measurements with samples, which suffered radiation damage or at high temperatures, exhibiting the advantages of SiC over Si. A selection of spectra taken with the Si, SiC and LGAD detectors is given in Figure C.4 in the appendix.

Signal Shapes

The shapes of the individual signals collected for the three detectors vary due to their different physical properties. The type amplification of course also has an impact on the collected signals as demonstrated in Figure 6.13a and 6.13b for the SiC detector read out with the BB amplifier and the TIA on the LGAD board. Figure 6.14a and 6.14b show to example peaks of the Si and LGAD detector gathered with the BB readout chain. The polarity of the peaks depends either on the amplifier or the doping profile of the sensor. It does, however, not affect other characteristics of the signal.

The clearest difference in the signals is in their time resolution. The relevant aspect here is the rise time, as the exponential decay of the signals after reaching their apex is a characteristic of the amplifier and should be roughly the same for all BB measurements. It is clearly visible, that the time response of the SiC detector is much faster than in Si in both the BB and the TIA signal. This is due to the Si detector's thickness of 300 µm being six times the one of the SiC with 50 µm and the longer drift time. The Si-LGAD is also much slower than SiC but sometimes twice as fast a the conventional Si diode. The internal amplification of the LGAD yields more than double the charge of Si when biased with 50 V. The gain of the LGAD is strongly dependent on the bias voltage. Even when measuring with the BB amplifier, one has to be careful not to bias it to high, as the amplifier might saturate. Due to the large signal, amplification with the CSA is not possible for the Si-LGAD detector.

	Area [nVs]	**Rise time [ns]**	**SNR**
SiC BB @300V	0.5-0.8	∼0.2	20-25
SiC TIA@300V	0.025-0.035	∼0.2	35-45
Si BB @300V	1.1-1.7	2.5-3	28-32
LGAD BB @50V	2.5-4.2	1.6-1.9	30-40

Table 6.1.: Characteristic ranges for the peak area, rise time and SNR for an example set of BB measurements for a Si, SiC and LGAD detector

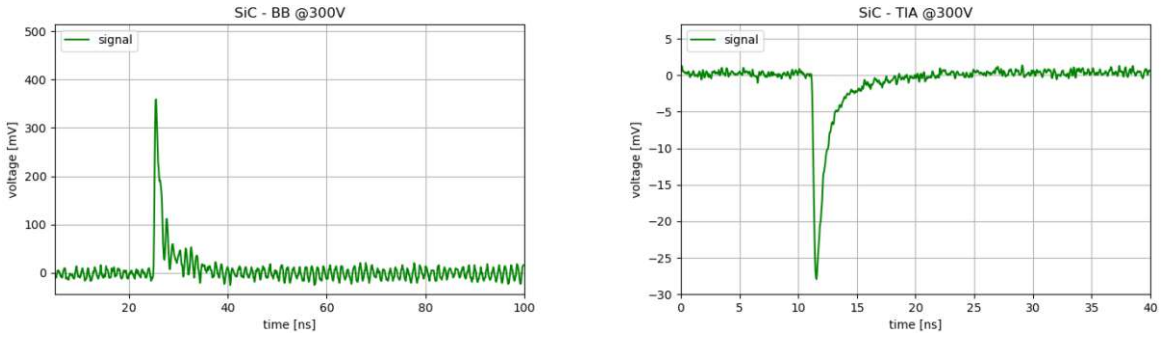

(a) SiC BB signal shape (b) SiC TIA signal shape

Figure 6.13.: The shape of an example signal peak of SiC measured with the BB amplifier on a bypassed LGAD board and with the onboard TIA. The BB amplifier is inverting, which is why the polarity differs for the same detector.

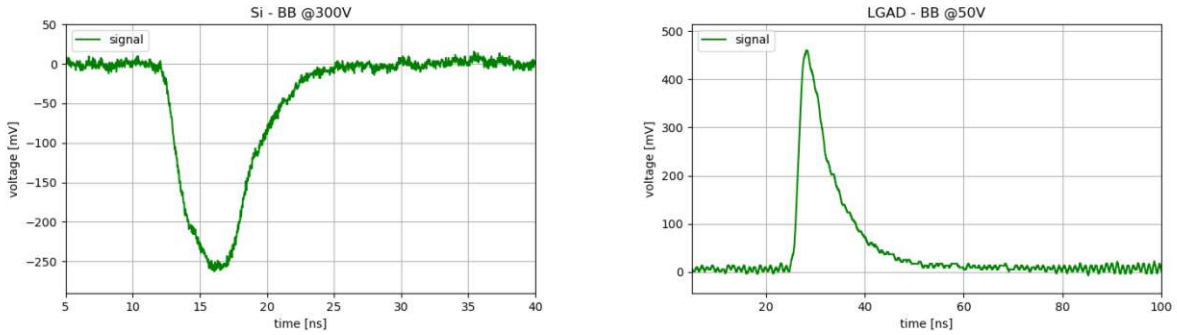

(a) Si BB signal shape (b) LGAD BB signal shape

Figure 6.14.: The shape of an example signal peak of Si and the Si-LGAD measured with the BB amplifier

The characteristics of the signal shapes for an example set of measurements for Si, SiC and LGAD are summarized in 6.1. Of course these values are varying with bias voltage, the type of radiation, geometry of the detectors and other factors. The given values are just intended to demonstrate the general characteristics of the given detectors.

The thinner SiC detector is clearly a faster option with a rise time about a factor ten smaller than the Si diode used. Over a number of measurement runs, a rise time of around 200 ps could be observed with the BB amplifier. The main advantage of the LGAD in this configuration is the bigger signal due to the internal amplification, which leads to an increased SNR compared to the other two sensors. The TIA signal (for the LGAD board used) is a factor 10 smaller than the amplitudes measured with the CSA and BB amplifier.

Concluding the observations made in this study, the use of the spectroscopic method is clearly recommended to ensure an accurate measurement of alpha radiation in future studies. With this mode of acquisition it is possible to reliably measure very reproducible, high resolution spectra showing little noise for different detectors, allowing for a direct comparison. The distinct decay energy peaks can be used for the calibration of spectra, as their energies scale linearly with both pressure and the ionization energy of the detectors. As for another advantage of SiC, an immunity to the visible spectrum was confirmed, allowing measurements in broad daylight.

7. SiC Ionization Energy

The average energy a single primary particle has to expend in order to produce one electron-hole pair on its passage through matter is referred to as the *ionization energy* ϵ_i. It is for all practical purposes independent of the total energy and type of radiation (although being temperature dependent) and thus allows for a direct conversion of the incident energy of a primary particle in terms of produced charge carrier pairs $n_{\text{e-h}}$, provided the particle comes to a complete stop in the medium. Alpha radiation is naturally an excellent candidate for this type of sensor calibration as it is completely absorbed, even in thin detectors. A good knowledge of the ionization energy for a given detector material is therefore a key part in evaluating spectra. As hinted in 2.2.5, the literature values for SiC are still ambiguous which is why further experimental clarification is needed.

In an ideal detector, all events along a particle track are considered independent and it is assumed that the the total number of electron-hole pairs is equal to $n_{\text{e-h}} = E/\epsilon_i$. The stopping of particles in matter is, however, subject to energy straggling and exhibits statistical fluctuations in both the number of individual processes and the respective individual energy losses. This process may be described by the Poisson statistic and leads to signal fluctuations on the order of $\sqrt{n_{\text{e-h}}}$. However, if the particle is completely absorbed in matter, the sum of individual contributions can not exceed the total energy of the incident particle due to energy conservation. This constraint allows for an improved energy resolution by a factor $\sqrt{F}$ smaller than one. The *Fano factor* F allows a specification of the intrinsic energy resolution for a given material due to fluctuations in the primary process of signal formation. It can be defined as the ratio of the observed variance σ to the assumed variance of the Poisson statistic $\sqrt{n_{\text{e-h}}}$

$$F = \frac{\text{observed variance}}{\text{Poisson variance}} = \frac{\sigma}{E/\epsilon_i}. \tag{7.1}$$

A detector should exhibit a Fano factor as small as possible, ideally close to zero, in order to enable a good energy resolution.

This chapter describes an indirect measurement of the SiC ionization energy by a comparison to the known value for Si. Values as low as 5.05 eV [51] as well as up to 8.6 eV [52] have previously been reported for SiC. Others determined it between 7 and 8 eV at 7.28 eV [53], 7.71 eV [54], 7.78 eV [55], 7.6 eV [56], and 7.8 eV [57], the first three using ^{241}Am alpha sources. A Fano factor for SiC was reported as 0.128 for measurements with an ^{241}Am source [53] or estimated as 0.1 using X-rays [58]. Others hypothesized a Fano factor for SiC around 0.12 [57].

7.1. Concept

The energy deposition of the triple alpha source is determined in a spectroscopic fashion for a Si and a SiC detector under identical conditions. This way, the only external factor needed for the determination of ϵ_{SiC} is the already well established value of ϵ_{Si} =3.62 eV [14]. The ionization energy is calculated from the ratio of the number of charge carriers $n_{\text{e-h}}$ produced by an alpha particle stopping in the detectors. In a spectroscopic readout chain, this corresponds to the ratio of the maxima of the CSA output

$$\frac{n_{\text{e-h}}^{\mathrm{Si}}}{n_{\text{e-h}}^{\mathrm{SiC}}} = \frac{V_{\mathrm{Peak}}^{\mathrm{Si}}}{V_{\mathrm{Peak}}^{\mathrm{SiC}}} = \frac{E_\alpha \epsilon^{\mathrm{SiC}}}{E_\alpha \epsilon^{\mathrm{Si}}} \Rightarrow \epsilon_{\mathrm{SiC}} = \frac{V_{\mathrm{Peak}}^{\mathrm{Si}}}{V_{\mathrm{Peak}}^{\mathrm{SiC}}} \cdot \epsilon_{\mathrm{Si}}. \tag{7.2}$$

Further analysis can be achieved by considering the width of the measured energy distributions. The Fano factor F scales as the product of ϵ_i and the observed variance σ of the corresponding peak in the energy distribution. It can be calculated from the same set of data as

$$F^{\mathrm{SiC}} = \frac{\epsilon^{\mathrm{SiC}} \cdot \sigma^{\mathrm{SiC}}}{\epsilon^{\mathrm{Si}} \cdot \sigma^{\mathrm{Si}}} \cdot F^{\mathrm{Si}}. \tag{7.3}$$

The absolute scale of σ is of no concern as long as the same metric for the variance is used in both spectra, as F is determined as a ratio. The individual variances per triple alpha peak were averaged for every spectrum, ϵ_{SiC} is taken as the value of the previously determined ionization energy. The Fano factor of Si is taken from literature as $F_{\mathrm{Si}} = 0.115$ [59]. The mean peak energies and variances were determined by applying both Gaussian and skewed Gaussian fits to all peaks as indicated in Figure 7.1. With several peaks per spectrum at multiple pressures, the final values of ϵ_{SiC} and F_{SiC} can be averaged to get a more reliable result.

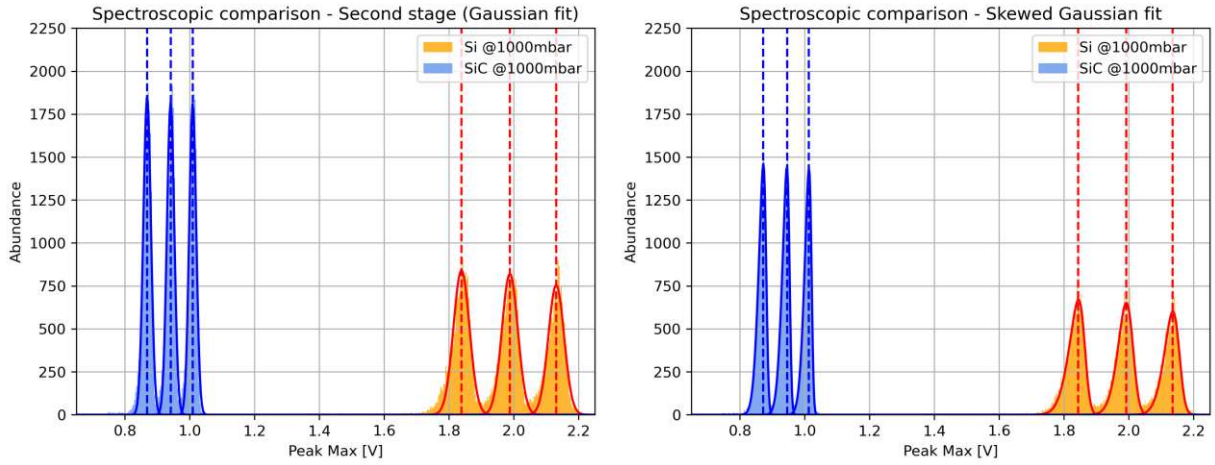

(a) Gaussian fit

(b) Skewed Gaussian fit

Figure 7.1.: Gaussian and skewed Gaussian fitting of the triple alpha peaks for the ionization energy and Fano factor calculation

7.1.1. Uncertainty Budget and Analysis

Assuming all individual contributions δx_i uncorrelated, the total uncertainty Δf_{tot} of a measured value f can be calculated as

$$\Delta f_{\text{tot}} = \sqrt{\delta x_1^2 + \delta x_2^2 + ... + \delta x_n^2} \tag{7.4}$$

using Gaussian error propagation

$$\delta x_i^2 = \left(\frac{\partial f(x_1, ..., x_n)}{\partial x_i} \right)^2 \cdot s_{x_i}^2. \tag{7.5}$$

Individual contributions are calculated from the measured data and estimated from equipment considerations per set of spectra (i.e. per pressure). Contributions to the uncertainty shared by both ϵ and F are:

- u_{noise}: Fluctuations in the measured voltage due to electronic noise,
- u_{CSA}: Deviations due to linearity effects of the CSA amplification (See appendix D for details),
- u_{fit}: The maximum uncertainties of the Gaussian and fit parameters (the mean μ for ϵ and the variance σ for F).

These are further combined with:

- $u_{\epsilon,\text{Lit.}}$: The variance of values for ϵ_{Si} that could be found in literature.

A final value of ϵ_{SiC} is achieved by averaging over all pressures. The associated uncertainty is calculated by combining the average individual uncertainty with:

- $u_{\epsilon,\text{Meas.}}$: The standard deviation of the individually determined values of ϵ_{SiC}.

To obtain uncertainties for the individual Fano factors, the spectrum uncertainty is combined with

- $\delta\epsilon_{\text{SiC}}$: The inherited uncertainty from the previous ionization energy calculation,
- $u_{\text{F,Lit.}}$ and $u_{\epsilon,\text{Lit.}}$: The variance of values for F_{Si} and ϵ_{Si} that could be found in literature.

The uncertainty for the final value F_{SiC} is again reached by combining the average individual uncertainty with:

- $u_{\text{F,Meas.}}$: The standard deviation of all individually determined values of F_{SiC} per pressure.

The literature uncertainties $u_{\text{F,Lit.}}$ and $u_{\epsilon,\text{Lit.}}$, as well as u_{noise} and u_{CSA} do not change with pressure.

The spectra measured with Si had to be re-scaled for two reasons. Firstly, the generated charge partly overshoots the assured linearity range of the CSA, rendering the resulting spectra increasingly distorted for higher energy depositions, i.e. the ^{241}Am and ^{244}Cm peaks at low pressure. The process of compensating this effect and an explanation of the associated uncertainty u_{CSA} are given in the appendix in D.

Secondly, the difference in the structure of the diodes has to be considered. As mentioned in section 3.4, the surface composition of the Si and SiC sensor is relatively similar (passivation and metalization, mainly Aluminium) and allows for their direct comparison. A scaling factor for the Si energy distributions is the result of an estimate using the Bethe-Bloch equation. It is achieved by calculating the ratio of the relative shift of the main ^{241}Am decay energy due to energy loss in the metalization to its initial value. $S_{\mathrm{structure}}$ =1.8 % quantifies the relative energy shift due to the different metalizations of the Si and SiC diode. The effect of the passivation is negligibly small due to the small thicknesses. A detailed description of the evaluation is given in the appendix in D.

Most of the initially considered uncertainties turned out to be negligible in the process of evaluation. In this evaluation, the biggest influence on the result is the choice of ϵ_{Si} and F_{Si} , for which a conservative uncertainty estimate is given from the range of values found in literature. The ionization energy of Si at 300 K has consistently been reported since the early 1960s between 3.6 eV and 3.65 eV, a commonly assumed value is 3.62 eV [17, 14] allowing an estimate of $u_{\epsilon,\mathrm{Lit.}} \approx 1.5\,\%$. The Fano factor for Si was reported between 0.084 [60] and 0.128 [61], with most reports accumulating around a value of 0.115 (or 0.12) [17, 13]. An uncertainty of $u_{\mathrm{F,Lit.}} \approx 5\,\%$ was estimated from a selection of reported values. An uncertainty contribution due to a difference in the source-detector distance, which was expected to grow with increasing pressure, was considered but turned out to be of negligible size by direct comparison of the spectra to each other as well as with GATE simulations.

7.2. Results

A series of spectra was taken for Si and SiC at pressures of 0.3, 50, 100, 250, 500 and 1000 mbar. Using skewed Gaussian fits, an average value for the ionization energy

$$\epsilon_{\mathrm{SiC}} = 7.755 \pm 0.132 \text{ eV}$$

could be determined agreeing with literature values between 7 and 8 eV with a relative error of only 1.7 % , being mainly attributed to the uncertainty of the ϵ_{Si} literature value. A Fano factor for SiC was measured as

$$F^{\mathrm{SiC}} = 0.100 \pm 0.01.$$

Due to the larger standard deviation of the individual measurements, the inherited uncertainty of ϵ_{SiC} and the ambiguous value for F_{Si}, its relative uncertainty measures 9.1 %.

The choice of fit function turned out to be negligible (below 0.02 %) in terms of the determined ionization energy between a Gaussian and a skewed Gaussian. For the Fano factor, the difference is around 1.5 %, which is below the uncertainty of the measured value. The figures 7.2 and 7.3 show the individual values and uncertainties for every pair of evaluated spectra (Skewed Gaussian fits) and the final averaged results and uncertainties of ϵ_{SiC} and F_{SiC}. Measured values and the final results for both evaluations are given in the appendix in Figure D.2.

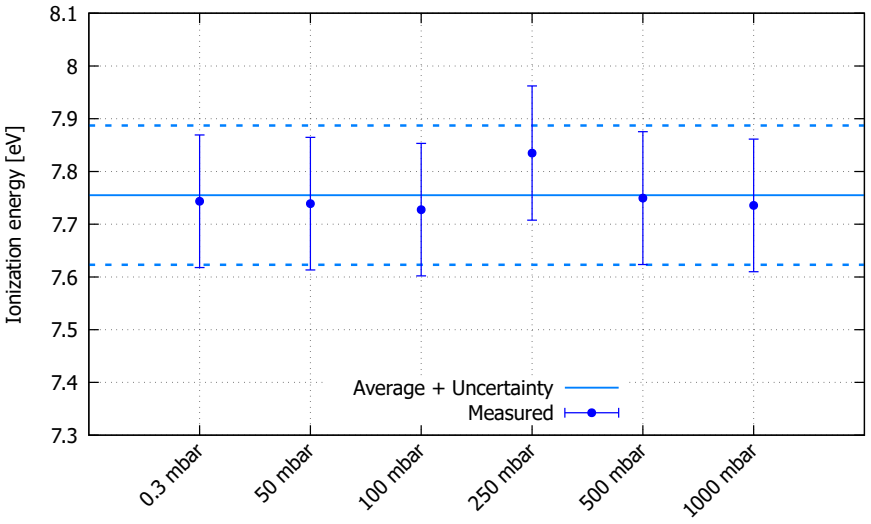

Figure 7.2.: Individual and average values measured for ϵ_{SiC}

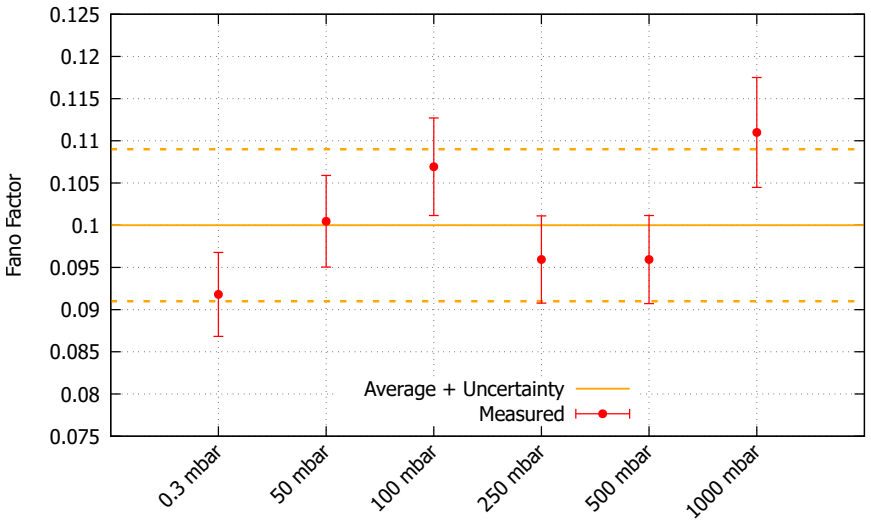

Figure 7.3.: Individual and average values measured for F_{SiC}

8. Conclusion and Outlook

A new vacuum setup was be designed, built and put in operation at HEPHY, providing a facility to perform measurements in selectable low pressure environments between 0.3 mbar and ambient pressure. This is especially valuable for consistently measuring highly ionizing alpha radiation. A control software was implemented featuring a simple, yet very reliable pressure control with the help of a PLC acting as both the controller and a communication device between the different components. The control software is structured in a way to allow the future extension and implementation into DAQ systems.

Spectra of the ^{241}Am and triple alpha source were measured thoroughly, employing different readout chains. Different types of semiconductor detectors and amplification schemes were compared. The triple alpha source turned out to be a suitable device for calibration measurements at any pressure regime, as the three peaks scale together with pressure in a predictable way. The individual decay energies stay separated in the spectra even at ambient pressure, regardless of the readout electronics.

Nevertheless, the spectroscopic readout chain employing a CSA enables the measurement of the highest precision spectra due to the low noise associated with its slow amplification. Measured results correspond very well with GATE simulations at all pressures. As these simulations precisely match the measured behavior, they may serve as input for the energy calibration of SiC detectors. Spectra taken with the BB or TIA readout chain can also be associated with the GATE simulations but do not show the distinct separation of the three decay energies evident in the spectroscopic measurements. This is a result of electronic noise significantly broadening the energy spectra. A clear recommendation is made for spectroscopic measurement using high-bandwidth oscilloscopes offering high vertical resolution. Alternatively, an MCA could be employed.

The general trend of a linear decrease of the mean peak energies of the alpha energy deposition with pressure, as well as a roughly linear increase of the energy spread, could be confirmed several times with a number of independent measurements and GATE simulations. This matches the theoretical expectations due to energy loss and straggling in air.

Due to the passivation and metalization of the diodes used, only a single broadened decay energy peak was visible per radioactive isotope. The spectrum measurements could be further enhanced in the future by employing detectors featuring as little surface metalization as possible to allow for a prospective secondary peak resolution.

Due to reduced high-voltage breakdown capabilities in vacuum, the HV compatibility of detectors and all its components need to be studied in the future. This was not yet necessary for the measurements in this work as the bias voltages were sufficiently low for the electronics not to suffer electrical breakdown in the vacuum. However, especially detectors who suffered radiation damage and particularly SiC detectors are biased with increasingly high voltages, up to the order of 1000 V. The characteristics and prevention of voltage breakdowns in PCBs and detectors used at low pressure can be studied in the future with the help of the new vacuum setup. During initial attempts over the course of the work no conclusive result could be reached.

Employing the spectroscopic readout chain, a value for the ionization energy $\epsilon_{\mathrm{SiC}} = 7.755 \pm 0.132$ eV and a Fano factor $F_{\mathrm{SiC}} = 0.100 \pm 0.01$ for SiC could be determined by evaluating a set of measurements performed under similar conditions. The results is in accordance with a number of published values and can serve as valuable input for calibrating SiC spectra. Further investigations like can be achieved in the future with a set of structurally similar detectors, possibly narrowing down the uncertainties of the measurements.

A. GATE Simulations

A.1. Effect of Gold Layer Thickness on ^{241}Am Spectra

Selected results of the GATE simulations quantifying the influence of the protective gold layer on the ^{241}Am alpha source in vacuum. A Gaussian fit is included in the plots as the peaks are initially barely skewed for thin gold layers.

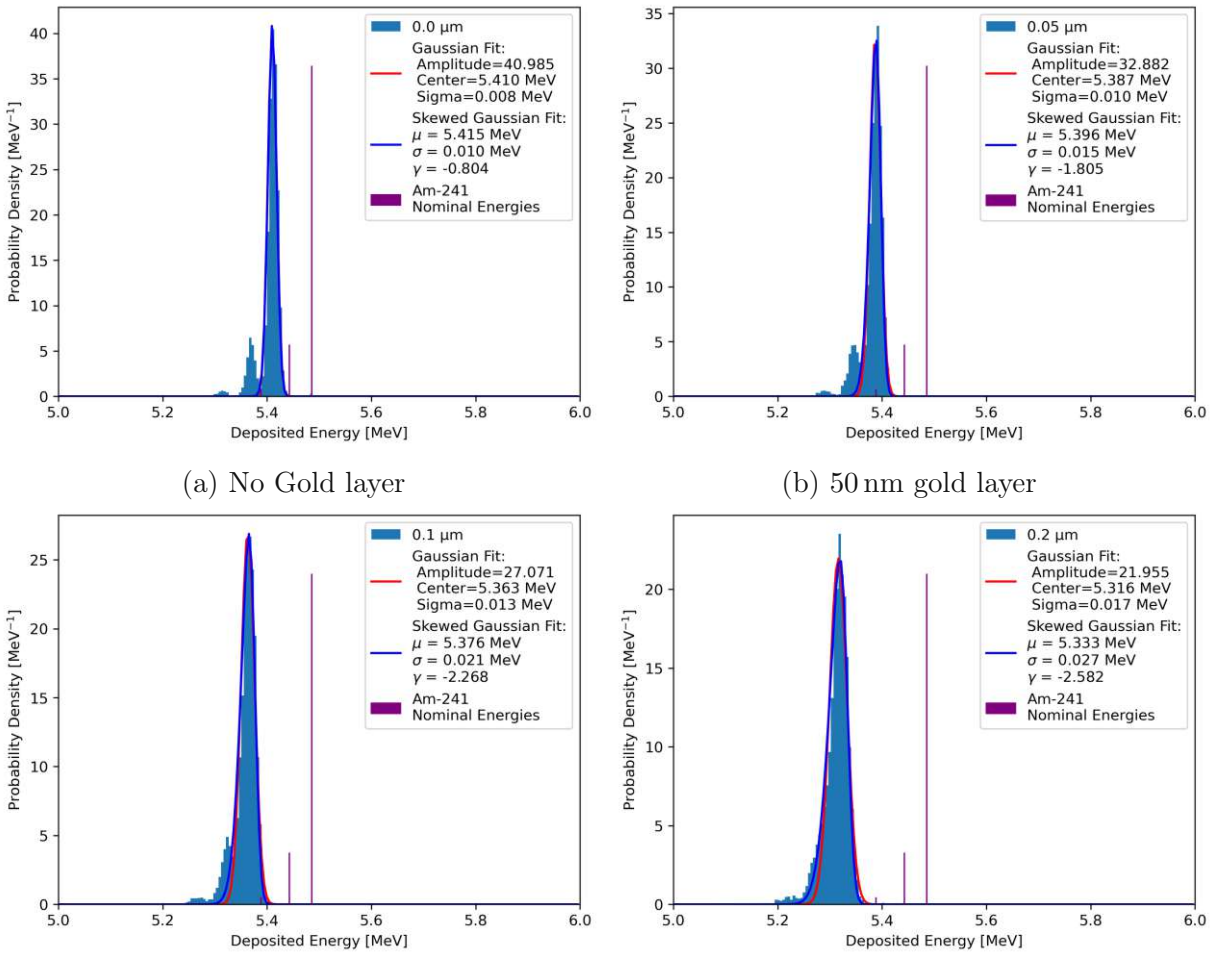

(a) No Gold layer

(b) 50 nm gold layer

(c) 100 nm gold layer

(d) 200 nm gold layer

Figure A.1.: Alterations in energy deposition of the ^{241}Am alpha source in a SiC detector as a function of the protective Gold layer thickness (in vacuum)

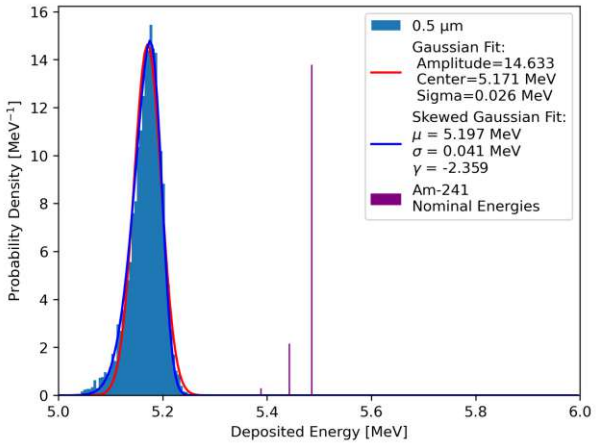

(e) 500 nm gold layer

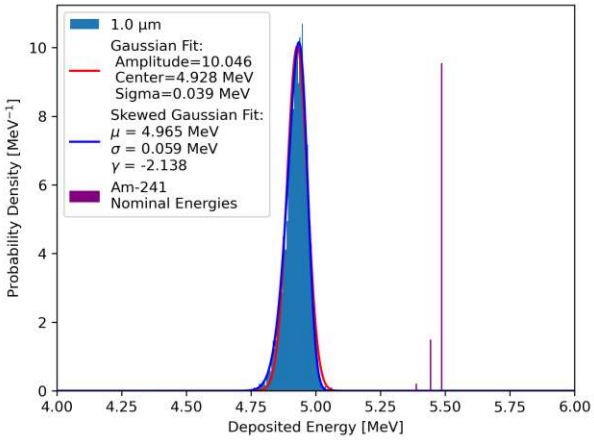

(f) 1 µm gold layer

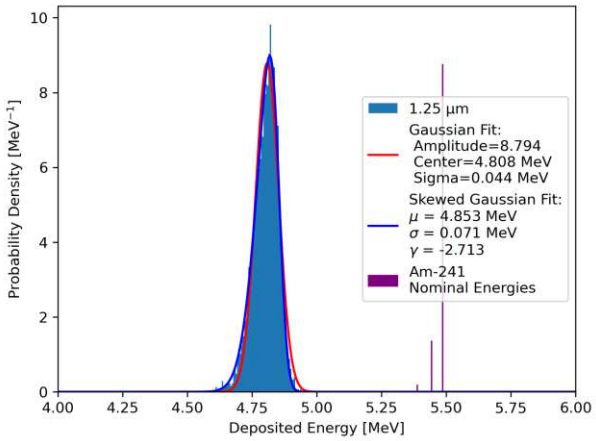

(g) 1.25 µm gold layer

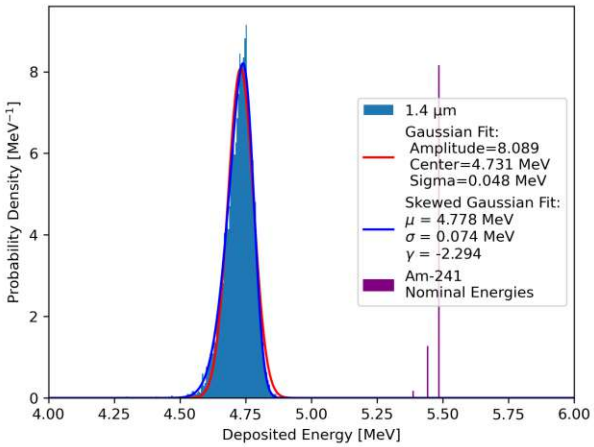

(h) 1.4 µm gold layer

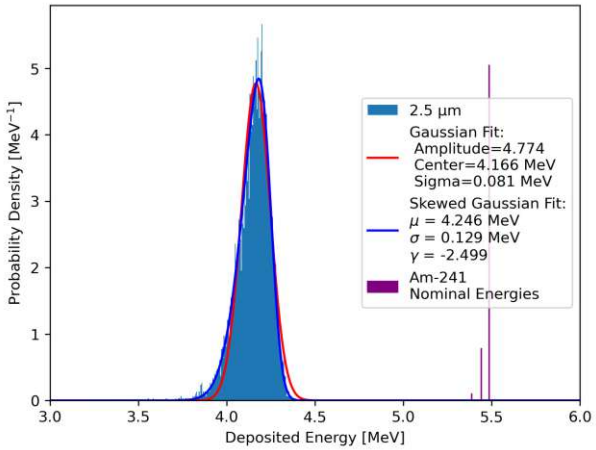

(i) 2.5 µm gold layer

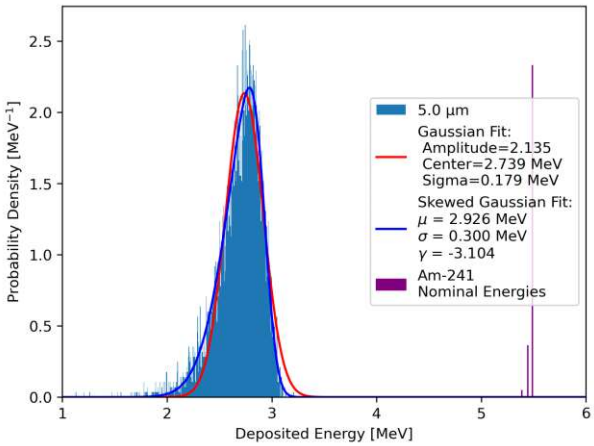

(j) 5 µm gold layer

Figure A.1.: Alterations in energy deposition of the ^{241}Am alpha source in a SiC detector as a function of the protective Gold layer thickness (in vacuum)

A.2. Pressure Response of the ^{241}Am Source

Selected results for the GATE simulations quantifying the pressure response of the ^{241}Am alpha source. As the peaks are all skewed, a Gaussian fit was omitted. Even at very low pressures, the energy is shifted strongly by the gold layer.

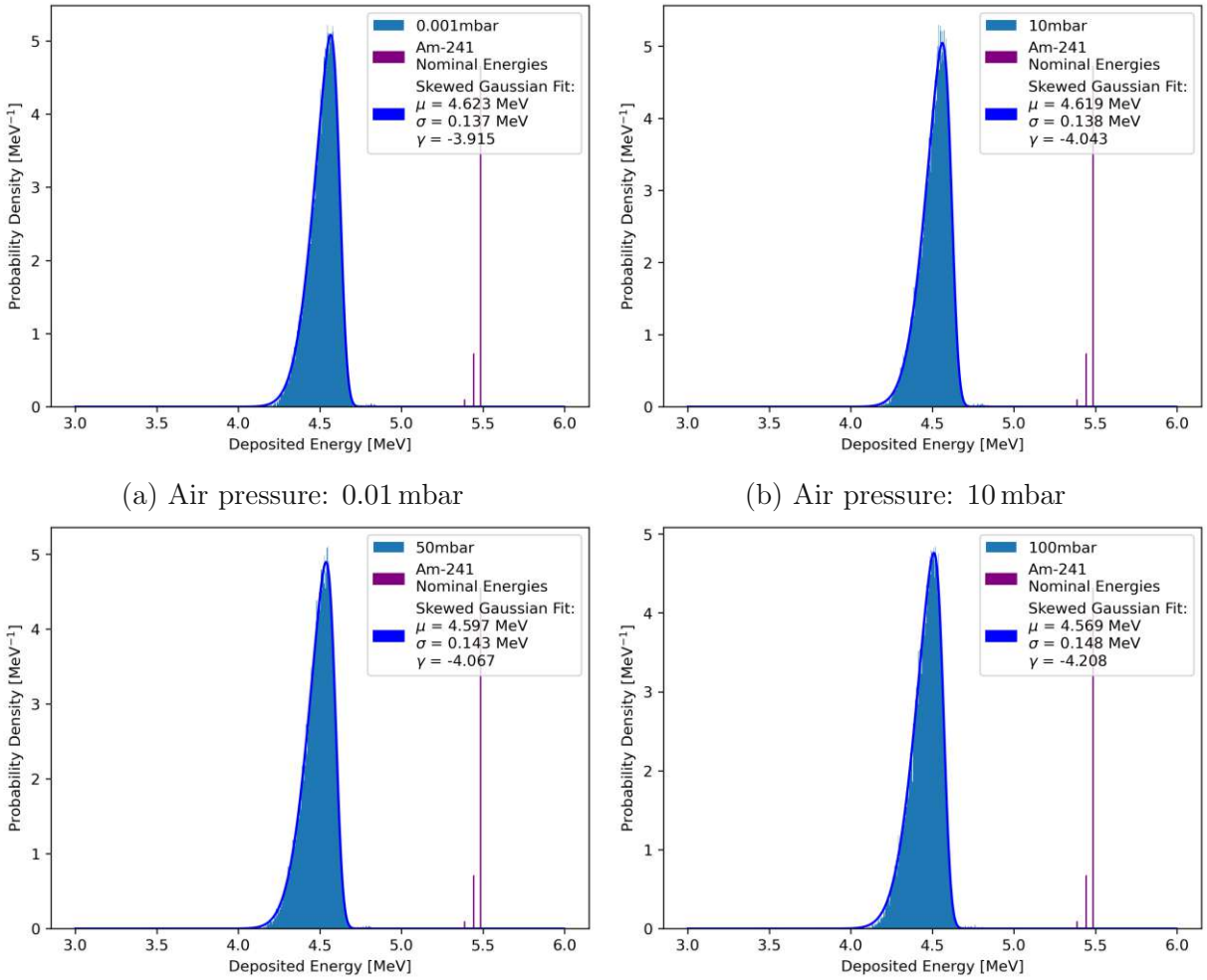

(a) Air pressure: 0.01 mbar

(b) Air pressure: 10 mbar

(c) Air pressure: 50 mbar

(d) Air pressure: 100 mbar

Figure A.2.: Energy deposition of the ^{241}Am alpha source in a SiC detector as a function of air pressure

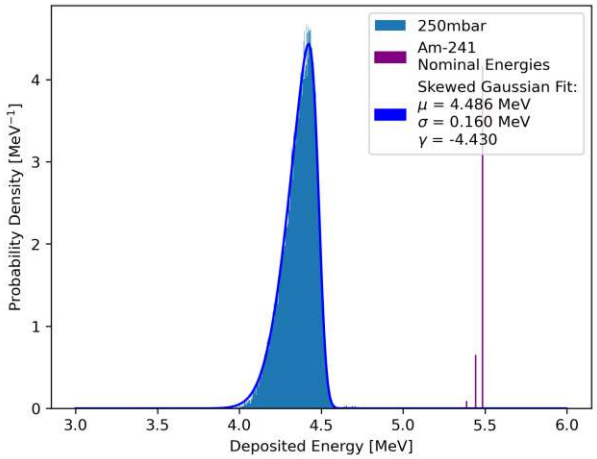

(e) Air pressure: 250 mbar

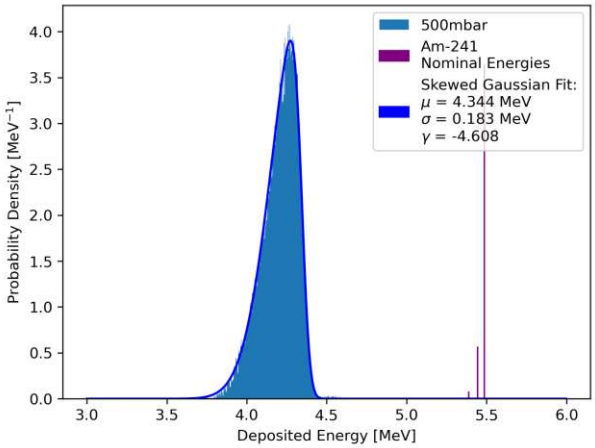

(f) Air pressure: 500 mbar

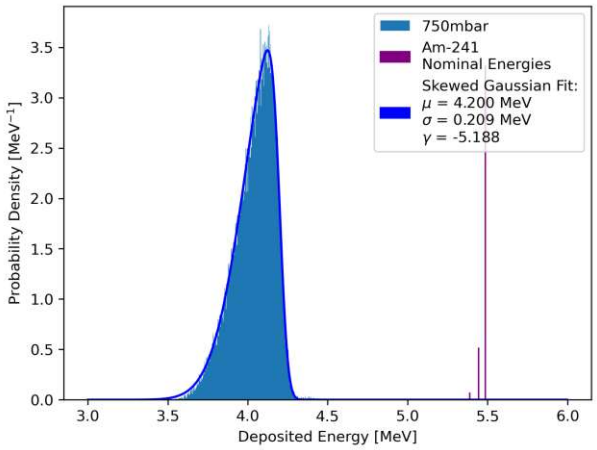

(g) Air pressure: 750 mbar

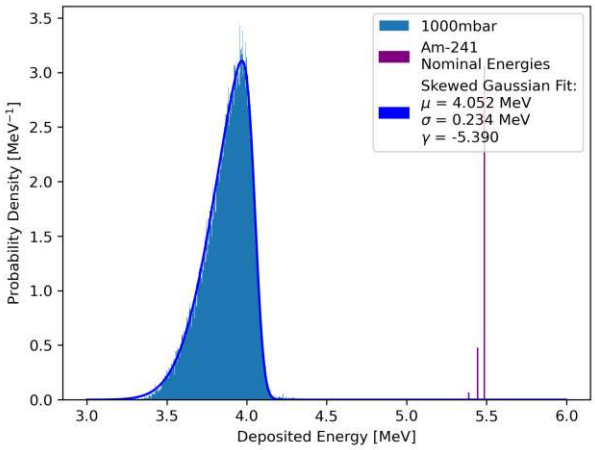

(h) Air pressure: 1000 mbar

Figure A.2.: Alterations in energy deposition of the ^{241}Am alpha source in a SiC detector as a function of the protective Gold layer thickness (in vacuum)

A.3. Pressure Response of the Triple alpha source

Selected results for the GATE simulations quantifying the pressure response of the triple alpha source. Fit functions are not included for visibility purposes.

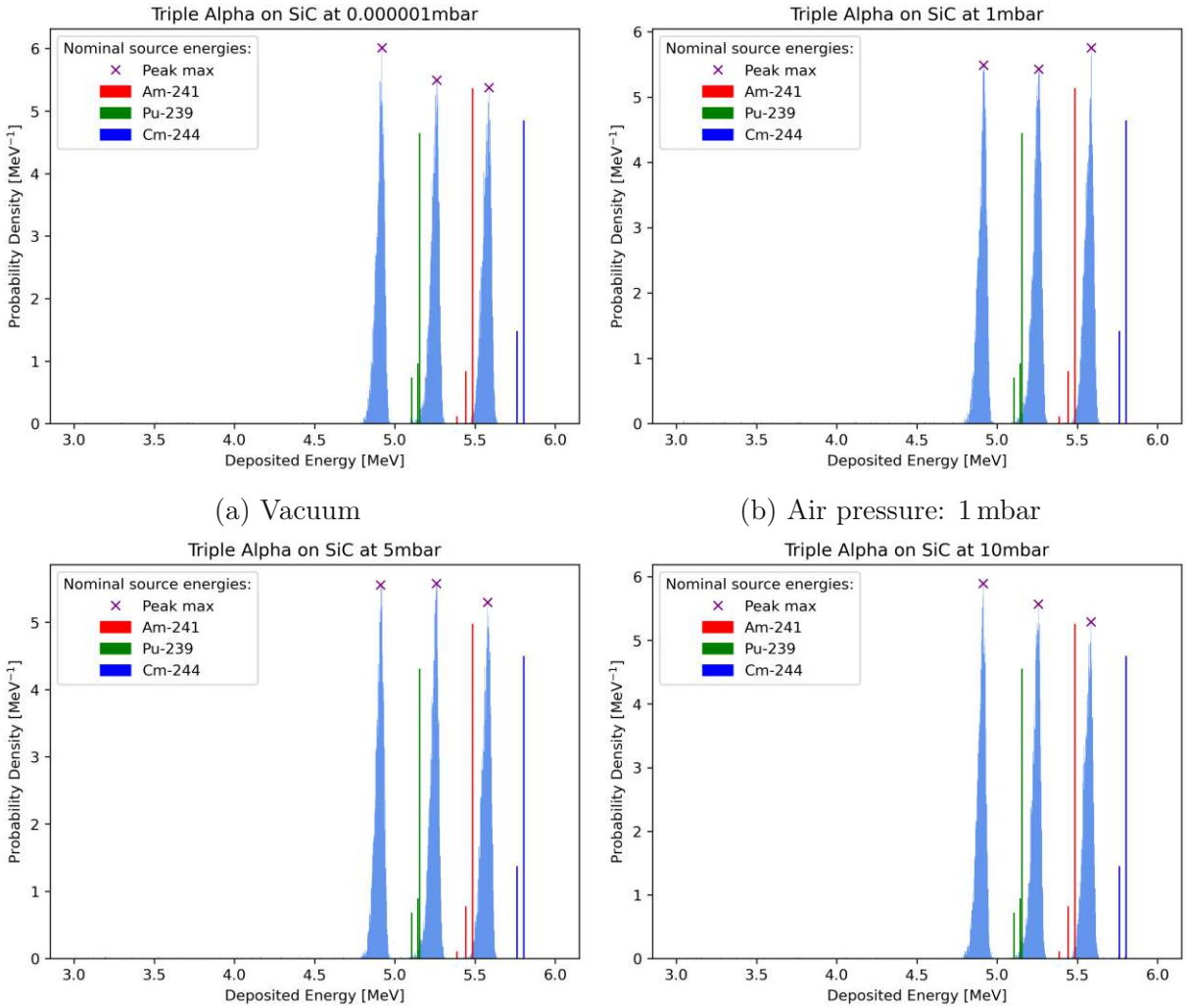

(a) Vacuum

(b) Air pressure: 1 mbar

(c) Air pressure: 5 mbar

(d) Air pressure: 10 mbar

Figure A.3.: Energy deposition of the Triple alpha source in a SiC detector as a function of air pressure

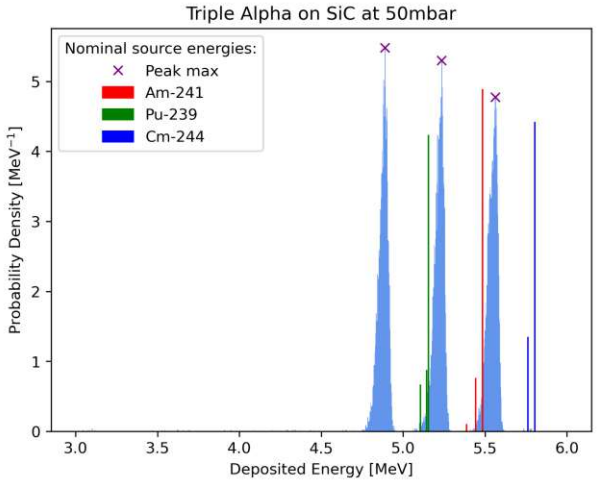

(e) Air pressure: 50 mbar

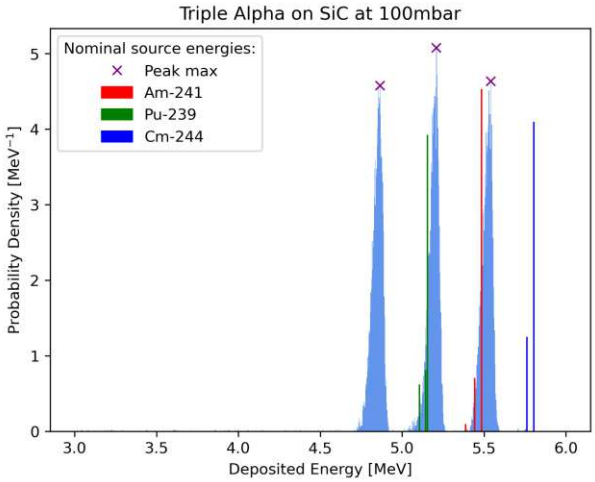

(f) Air pressure: 100 mbar

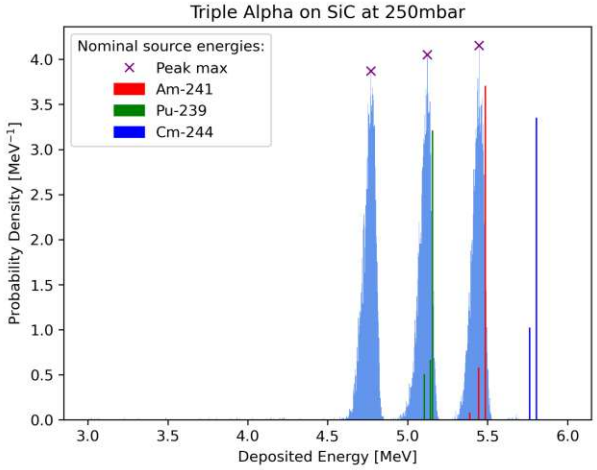

(g) Air pressure: 250 mbar

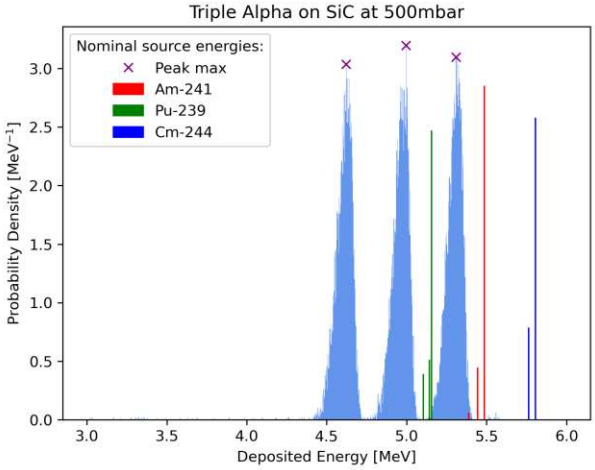

(h) Air pressure: 500 mbar

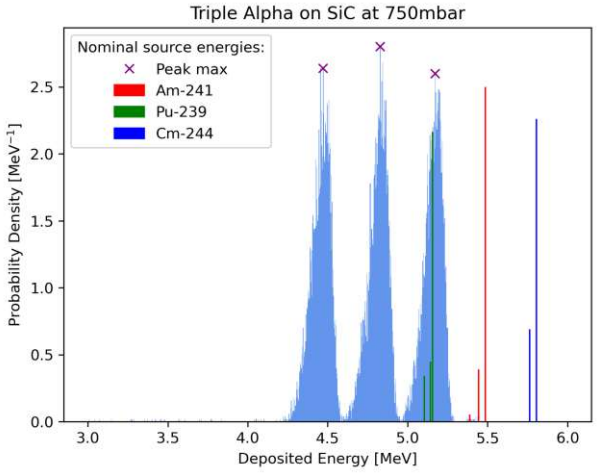

(i) Air pressure: 750 mbar

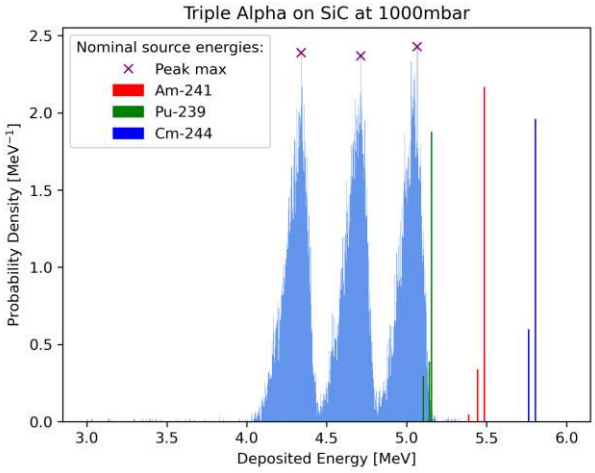

(j) Air pressure: 1000 mbar

Figure A.3.: Energy deposition of the Triple alpha source in a SiC detector as a function of air pressure

B. Pressure Control Code

The JSON-RPC Server implemented to interact with the vacuum setup:

```
import jsonrpc
import logging
import socketserver
import time
from typing import Any, Dict

from PressureController import PressureController
logger = logging.getLogger(__name__)

class TCPHandler(socketserver.BaseRequestHandler):

    buffer_size: int = 1024

    def handle(self) -> None:
        self.data = self.request.recv(self.buffer_size).strip().decode("utf-8")
        logger.info("%s wrote: %s", self.client_address[0], self.data)
        # self.server.messageReady.emit(format(self.data))
        response = self.server.rpcHandler.handle(self.data)
        if response:
            data = response.json.encode("utf-8")
            logger.info("%s returned: %s", self.client_address[0], response.json)
            # self.server.messageReady.emit(format(response.json))
            self.request.sendall(data)

class TCPServer(socketserver.TCPServer):

    allow_reuse_address: bool = True

class RPCHandler:

    def __init__(self) -> None:

        self.PressureController = PressureController()

        #Adding methods
        self.dispatcher = jsonrpc.Dispatcher()
        self.dispatcher["state"] = self.get_state
        self.dispatcher["set_pressure"] = self.set_pressure
        self.dispatcher["open_valve"] = self.open_valve
        self.dispatcher["close_valve"] = self.close_valve
        self.manager = jsonrpc.JSONRPCResponseManager()
```

```
45      def handle(self, request) -> Dict[str, Any]:
46          print("Got JSON string as request: ", request)
47
48          return self.manager.handle(request, self.dispatcher)
49
50      def set_pressure(self, **kwargs):
51          pressure_to_set = kwargs["set_pressure_mbar"]
52          print("Set pressure was called with {} mbar".format(pressure_to_set))
53          self.PressureController.set_pressure(pressure_to_set)
54
55      def get_state(self):
56          print("Get state was called")
57          gauge = self.PressureController.read_gauge()
58          valve = self.PressureController.read_valve()
59
60          response = {
61              "jsonrpc": "2.0",
62              "result": {"valve_voltage_volt": valve, "gauge_pressure_mbar": gauge},
63              "id": 0
64          }
65
66          return response
67
68      def open_valve(self):
69          print("Open valve was called")
70          self.PressureController.open_valve()
71
72      def close_valve(self):
73          print("Close valve was called")
74          self.PressureController.close_valve()
75
76  class Server:
77
78      def __init__(self, hostname: str, port: int) -> None:
79          """Constructor
80
81          Args:
82              hostname (str): Hostname
83              port (int): Port to listen on
84          """
85          self.hostname = hostname
86          self.port = port
87
88      def _setupServer(self, server):
89          """Setup the TCP server by adding the RPC handler
90
91          Args:
92              server (TCPServer): TCPServer to configure
93          """
94          server.rpcHandler = RPCHandler()
95
96
97
```

```
    def runServer(self) -> None:
        """Start running the server"""

        logger.info("TCP started %s:%s", hostname, port)
        try:
            with TCPServer((self.hostname, self.port), TCPHandler) as server:

                self._setupServer(server)
                server.serve_forever()
        except Exception as exc:
            logger.exception(exc)
        finally:
            logger.info("TCP stopped %s:%s", hostname, port)
            time.sleep(0.50)

if __name__ == "__main__":

    hostname = "127.0.0.1"
    port = 8001

    server = Server(hostname, port)
    server.runServer()
```

The list of functions for the JSON-RPC Server:

```
import snap7
import logging
import numpy as np

logger = logging.getLogger(__name__)

class PressureController:

    def __init__(self):
        #Connect to LOGO
        self.plc = snap7.logo.Logo()
        self.plc.connect("192.168.0.73", 0x0200, 0x0300)

        if self.plc.get_connected():
            logger.info("PLC connected")
        else:
            logger.error("PLC conncetion failed")

    def read_gauge(self):
        """ Read value from Analog In 1 (Pressure Gauge) connected to LOGO AM1
           Returns: gauge_press_mbar (float): Current pressure measured by gauge in
     mbar
        """

        vm_address_am1 = ("VW1118")
        gauge_volt_num = self.plc.read(vm_address_am1)
        gauge_press_mbar = 10**((gauge_volt_num/100) - 5.5)

        return gauge_press_mbar
```

```
29
30      def read_valve(self):
31          """ Read value from Analog Out 1 (Needle valve) connected to LOGO AM3
32          Returns: valve_volt_volt (float): Current voltage supplied to Needle valve
    in V """
33
34          vm_address_am3 = ("VW1122")
35          valve_volt_num = self.plc.read(vm_address_am3)
36          valve_volt_volt = valve_volt_num * 100
37
38          return valve_volt_volt
39
40      def set_pressure(self, set_press_mbar):
41          """ Send value to LOGO AM2 connected to Internal PI Controller
42          Args: set_press_mbar (float): Desired pressure in mbar """
43
44          print('Pressure set to {} mbar'.format(set_press_mbar))
45          set_volt = round(((5.5 + np.log10(float(set_press_mbar)))*100),0)
46          vm_address_am2 = ("VW1120")
47          self.plc.write(vm_address_am2, int(set_volt))
48
49      def close_valve(self):
50          """ Completely shut needle valve """
51
52          vm_address_am3 = ("VW1122")
53          self.plc.write(vm_address_am3, 0)
54
55      def open_valve(self):
56          """ Completely open needle valve """
57
58          vm_address_am3 = ("VW1122")
59          self.plc.write(vm_address_am3, 1000)
```

C. Selected Measurement Results

Data for the spectroscopic pressure ramp of the ^{241}Am source in Si gathered at low resolution with the Tektronix TBS2204B oscilloscope. The linear decrease in energy deposition in the detector with pressure could again be verified. Due to the low resolution, the determination of the energy distribution width deviates from the ideal linear behavior.

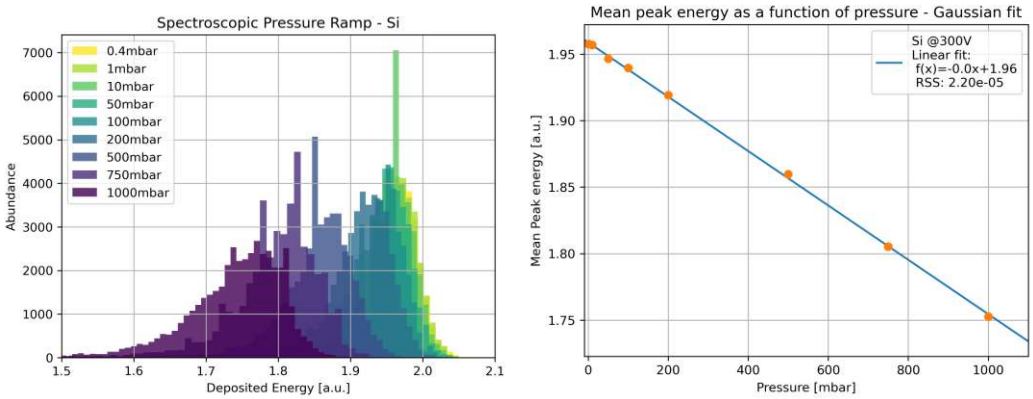

(a) Mean peak energy against pressure (b) Peak width against pressure

Figure C.1.: Spectroscopic pressure ramp of ^{241}Am in Si. Linear behavior in both energy and peak width in the spectroscopic pressure ramp of ^{241}Am in Si

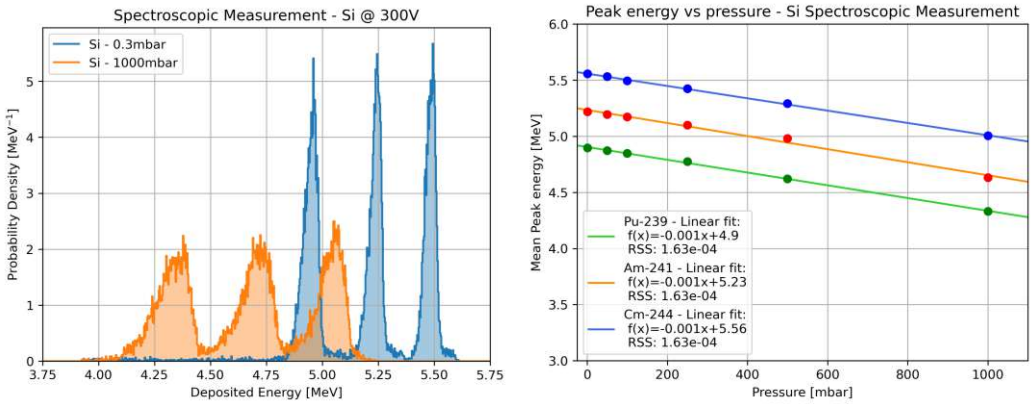

(a) Pressure response measured with the Si detector (b) Mean peak energy against pressure for the Si detector

Figure C.2.: Spectroscopic pressure ramp for the triple alpha source in Si

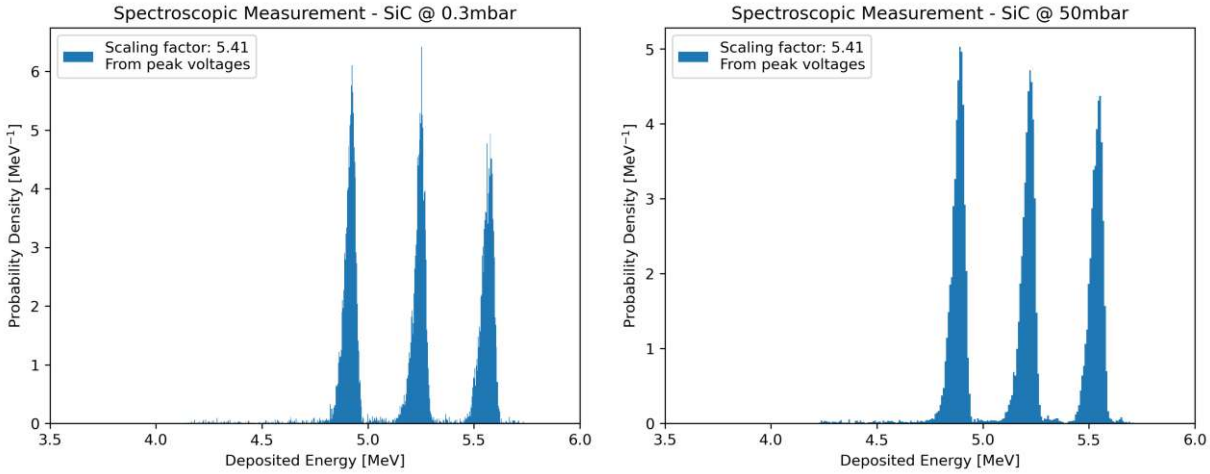

(a) Air pressure: 0.3 mbar

(b) Air pressure: 50 mbar

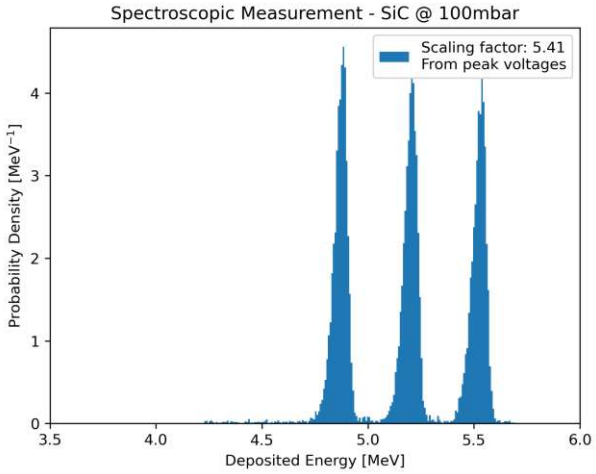

(c) Air pressure: 100 mbar

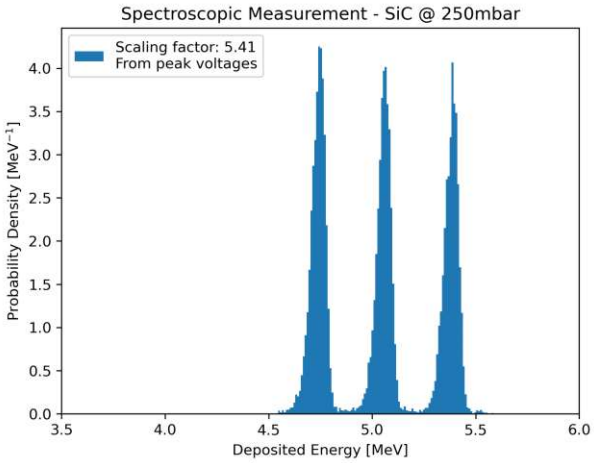

(d) Air pressure: 250 mbar

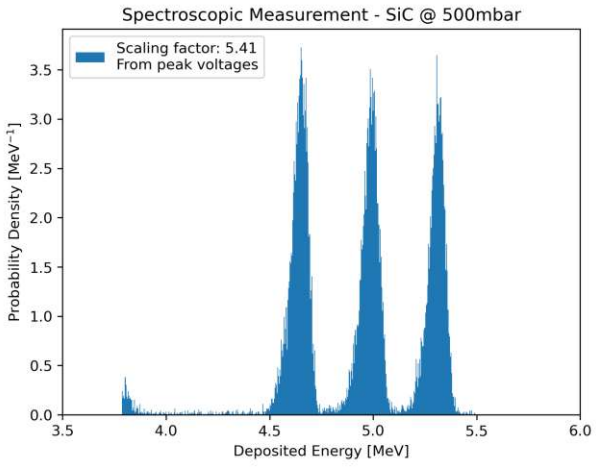

(e) Air pressure: 500 mbar

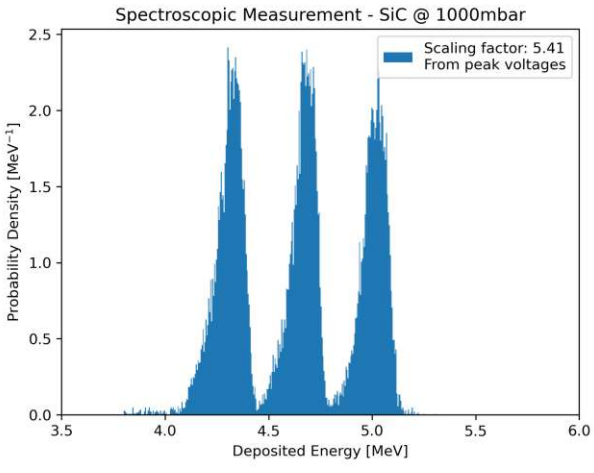

(f) Air pressure: 1000 mbar

Figure C.3.: Spectroscopic pressure ramp for the triple alpha source in SiC

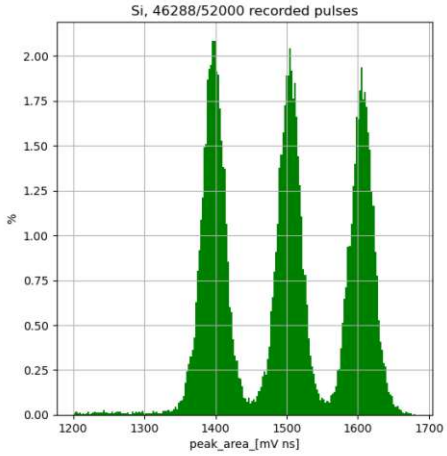

(a) Si at 0.3 mbar

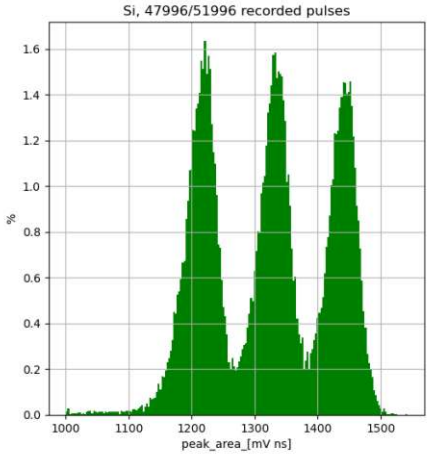

(b) Si at 1000 mbar

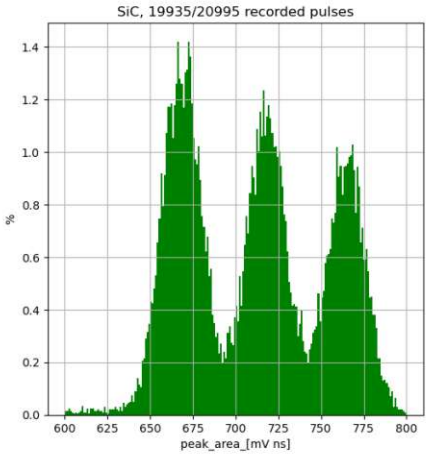

(c) SiC at 0.3 mbar

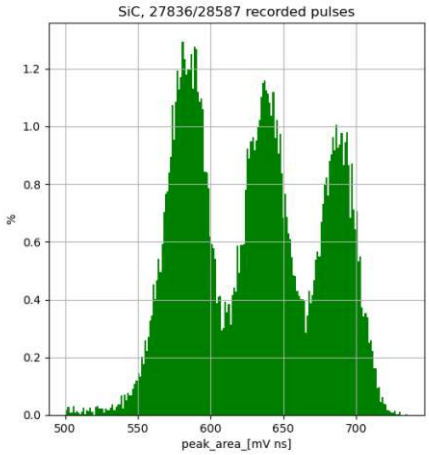

(d) SiC at 1000 mbar

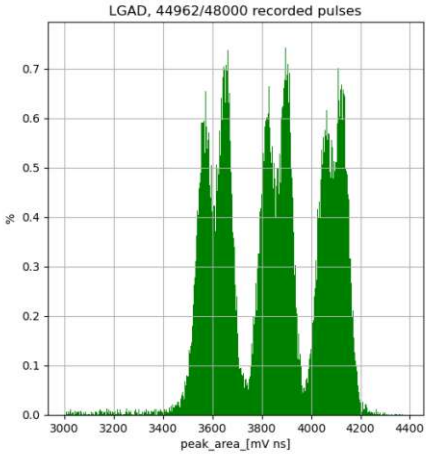

(e) LGAD at 0.3 mbar

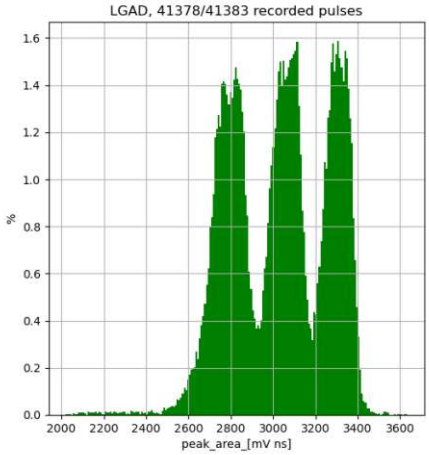

(f) LGAD at 1000 mbar

Figure C.4.: BB triple alpha spectra for the Si, SiC and LGAD detector

D. Annotations to the ϵ_{SiC} Measurement

The scaling factor for the Si spectra, which are necessary due to the difference in the structure of the diodes, was estimated via a calculation of the relative shift of the ^{241}Am peak (the approximate mean of a triple alpha spectrum) due to the surface layers above the active volume with the Bethe-Bloch equation.

At first, values for the stopping power $-\frac{\mathrm{d}E}{\mathrm{d}x}$ in the relevant materials upon entering (at $x = 0$) were obtained with [62]. These were then multiplied with the thickness Δx of a given layer to get an estimate of the amount of energy a particle loses by traversing it. This value is then expressed as a percentage relative to the nominal ^{241}Am peak energy to get a measure of the approximate relative shift in energy $\Delta E_{\%}$ for an alpha peak as

$$\Delta E_{\%} = \frac{-\frac{\mathrm{d}E}{\mathrm{d}x} \cdot \Delta x}{E_{\text{Am-241}}}. \tag{D.1}$$

The multiplication yields a sufficiently accurate result for the energy loss in thin absorbers without the need for a proper integration of the Bethe-Bloch formula. An alpha particle with 5.486 MeV loses about 158.45 keV µm^{-1} upon entering Aluminium. For a thickness of 1.5 µm this leads to an energy shift of about 5 % to the nominal peaks. This constitutes the difference between a detector without any metalization and a generous overestimation of the Aluminium metalization on the Si detector. The metalization of the SiC diodes (Ti, Al, Ni with a total of 1020 nm) amount to a combined shift of 3.3 % of the average peak energy. The passivation layers have a negligible effect on the measurement. Firstly, they are considered to be the same for both sensors and secondly, they are only on the order of 100 nm thick, which consequently leads to a shift in the peak energy of less than 0.5 %. The scaling factor for the Si spectra associated with the different structure can hence be taken as the difference in the relative energy shift due to both metalizations

$$S_{\text{structure}} = \Delta E_{\%}^{\text{Si-metal}} - \Delta E_{\%}^{\text{SiC-metal}} = +1.8\%. \tag{D.2}$$

Table D.1 summarizes the results of this estimate.

The ^{241}Am and ^{244}Cm voltages measured with the Si detector overshoot the linearity range of the CSA, slightly deforming the upper part of the spectra. To get a consistent basis for comparison, these spectra were re-scaled by determining the CSA gain function. As the ^{239}Pu voltages are below 2 V, their amplification is still perfectly linear. A scaling factor was determined per spectrum as the ratio mean peak voltages of ^{239}Pu in Si to the

	Material	$-\frac{dE}{dx}$ **at** $\Delta x = 0$ **[keV µm^{-1}]**	**Approx.** $\Delta E_{\%}$ **[%]**
Si	Aluminium (Δx =1.5 µm)	158.45	5.0
SiC	Titan (Δx =70 nm)	90.16	0.1
	Aluminium (Δx =870 nm)	158.45	2.5
	Nickel (Δx =80 nm)	406.40	0.6
Passivation	SiO_2(Δx =100 nm)	140.50	0.26
	Si_3N_4(Δx =100 nm)	177.08	0.32

Table D.1.: Relative shifts in the ^{241}Am peak energy due to the metalization and passivation layers obtained from Bethe-Bloch estimations

ones in SiC,

$$S_{\text{Pu-239}} = \frac{V^{\text{Si}}_{\text{Pu-239}}}{V^{\text{SiC}}_{\text{Pu-239}}}. \tag{D.3}$$

Plotting the initially measured values $V^{\text{Si}}_{\text{Peak}}$ for all three peaks against the scaled values $V^{\text{SiC}}_{\text{Peak}} \cdot S_{\text{Pu-239}}$ yields the amplification curve of the CSA. The inverse of this curve can be used to scale the spectra of Si to the assumed ideal linearity of a shaping amplifier. A satisfying continuous scaling function could be found by fitting a third order polynomial to the data as shown in Figure D.1. The largest deviation of the measured values from the polynomial fit was taken as the uncertainty contribution associated with this process.

$$u_{\text{CSA}} = 0.37\%. \tag{D.4}$$

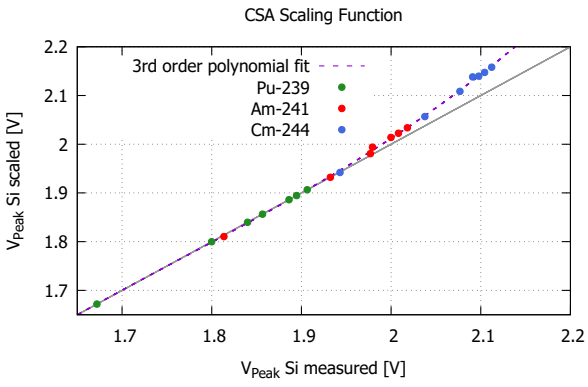

(a) Scaling function for the CSA (Inverse of the gain function)

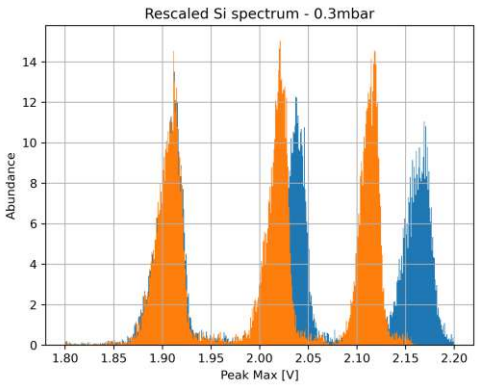

(b) Re-scaled Si spectrum at 0.3 mbar

Figure D.1.: Rescaling of the Si spectra taken with the CSA

The table in Figure D.2 summarizes the peak voltages and widths used for the evaluation of the ionization energy of SiC as they were determined by fitting Gaussian and skewed Gaussian functions to the spectra. For Si, both the originally obtained values and the ones for the scaled spectra are given.

GAUSSIAN EVALUATION

Pressure	Original Peak Voltage Si [V]			Re-scaled Peak Voltage Si [V]			Peak Voltage SiC [V]			Mean Rel.	Original σ Si [mV]			Re-scaled σ Si [mV]			σ SiC [mV]			Mean Rel.	ϵ_{SiC} [eV]	error ϵ_{SiC} [eV]	F_{SiC}	error F_{SiC}
	Pu-239	Am-241	Cm-241	Pu-239	Am-241	Cm-241	Pu-239	Am-241	Cm-241	Size V	Pu-239	Am-241	Cm-241	Pu-239	Am-241	Cm-241	Pu-239	Am-241	Cm-241	Size F				
0.3	1.906	2.018	2.112	1.941	2.071	2.201	0.908	0.968	1.028	2.140	11.836	9.439	9.082	12.761	11.992	13.621	4.638	4.488	5.190	0.798	7.746	0.126	0.092	0.005
50	1.895	2.008	2.104	1.928	2.059	2.189	0.902	0.963	1.022	2.139	12.236	10.404	8.933	13.111	12.931	13.227	5.158	5.125	5.421	0.855	7.745	0.126	0.098	0.005
100	1.886	2.000	2.098	1.919	2.048	2.179	0.899	0.960	1.020	2.134	11.559	10.799	9.050	12.292	13.258	13.197	5.573	5.834	5.919	0.955	7.727	0.125	0.110	0.006
250	1.857	1.977	2.077	1.889	2.021	2.149	0.875	0.934	0.994	2.162	14.800	10.739	11.128	15.351	12.741	15.595	6.057	6.012	6.293	0.915	7.826	0.127	0.105	0.006
500	1.800	1.932	2.038	1.831	1.970	2.096	0.858	0.921	0.980	2.138	17.395	14.995	14.490	17.408	16.805	18.959	7.265	7.389	6.970	0.873	7.739	0.126	0.100	0.005
1000	1.672	1.814	1.943	1.703	1.845	1.981	0.797	0.863	0.926	2.138	25.951	25.300	20.993	26.357	25.533	24.065	11.529	10.353	10.745	0.919	7.740	0.126	0.106	0.006
																				AVERAGE	**7.754**	**0.131**	**0.102**	**0.008**
																				STD. DEV.	0.036		0.006	

SKEWED GAUSSIAN EVALUATION

Pressure	Original Peak Voltage Si [V]			Re-scaled Peak Voltage Si [V]			Peak Voltage SiC [V]			Mean Rel.	Original σ Si [mV]			Re-scaled σ Si [mV]			σ SiC [mV]			Mean Rel.	ϵ_{SiC} [eV]	error ϵ_{SiC} [eV]	F_{SiC}	error F_{SiC}
	Pu-239	Am-241	Cm-241	Pu-239	Am-241	Cm-241	Pu-239	Am-241	Cm-241	Size V	Pu-239	Am-241	Cm-241	Pu-239	Am-241	Cm-241	Pu-239	Am-241	Cm-241	Size F				
0.3	1.910	2.021	2.115	1.945	2.075	2.203	0.909	0.971	1.030	2.139	46.628	37.601	34.253	50.564	47.576	51.413	17.518	17.699	20.622	0.798	7.744	0.126	0.092	0.005
50	1.898	2.012	2.108	1.932	2.063	2.193	0.904	0.966	1.025	2.138	47.313	40.946	35.126	50.169	50.919	51.344	20.219	20.553	21.529	0.874	7.739	0.126	0.100	0.005
100	1.891	2.004	2.100	1.922	2.053	2.183	0.902	0.961	1.022	2.135	45.257	43.021	35.482	47.839	52.333	51.535	21.270	21.545	23.214	0.930	7.728	0.125	0.107	0.006
250	1.864	1.982	2.081	1.895	2.025	2.153	0.877	0.934	0.995	2.164	60.690	43.686	43.632	62.418	51.543	60.276	22.688	21.150	23.056	0.834	7.835	0.127	0.096	0.005
500	1.804	1.938	2.044	1.834	1.975	2.103	0.860	0.921	0.981	2.141	65.485	59.512	57.266	66.194	65.579	73.095	28.008	26.228	25.290	0.834	7.749	0.126	0.096	0.005
1000	1.676	1.819	1.950	1.709	1.852	1.988	0.800	0.867	0.929	2.137	87.868	96.250	80.846	91.974	97.650	91.014	45.670	41.179	39.752	0.965	7.736	0.126	0.111	0.007
																				AVERAGE	**7.755**	**0.132**	**0.100**	**0.009**
																				STD. DEV.	0.040		0.007	

Figure D.2.: Data for the evaluation of ϵ_{SiC} and F_{SiC}

List of Figures

List of Tables

Bibliography

[1] R. R. Wilson. "Radiological Use of Fast Protons". *Radiology* 47.5 (1946), 487–491.

[2] O. Jäkel. "Physical advantages of particles: protons and light ions". *The British Journal of Radiology* 93.1107 (2020), 20190428. ISSN: 0007-1285, 1748-880X. DOI: 10.1259/bjr.20190428.

[3] Doug Berry et al. *4-Dimensional Trackers*. 2022.

[4] N. Cartiglia et al. "LGAD designs for Future Particle Trackers". *Nuclear Instruments and Methods in Physics Research Section A: Accelerators, Spectrometers, Detectors and Associated Equipment* 979 (2020), 164383. ISSN: 01689002. DOI: 10.1016/j.nima.2020.164383.

[5] M. De Napoli. "SiC detectors: A review on the use of silicon carbide as radiation detection material". *Frontiers in Physics* 10 (2022), 898833. ISSN: 2296-424X. DOI: 10.3389/fphy.2022.898833.

[6] M. Christanell, M. Tomaschek, and T. Bergauer. "4H-silicon carbide as particle detector for high-intensity ion beams". *Journal of Instrumentation* 17.1 (2022), C01060. ISSN: 1748-0221. DOI: 10.1088/1748-0221/17/01/C01060.

[7] F. Nava et al. "Silicon carbide and its use as a radiation detector material". *Measurement Science and Technology* 19.10 (2008), 102001. DOI: 10.1088/0957-0233/19/10/102001.

[8] R. Bernat et al. "Response of 4H-SiC Detectors to Ionizing Particles". *Crystals* 11.1 (2020), 10. ISSN: 2073-4352. DOI: 10.3390/cryst11010010. URL: https://www.mdpi.com/2073-4352/11/1/10.

[9] P. Gaggl et al. "Performance of neutron-irradiated 4H-silicon carbide diodes subjected to alpha radiation". *Journal of Instrumentation* 18.1 (2023), C01042. ISSN: 1748-0221. DOI: 10.1088/1748-0221/18/01/C01042.

[10] N. Vajda, Paul Martin, and Chang-Kyu Kim. *Alpha Spectrometry*. Elsevier, 2012, 363–422. ISBN: 978-0-12-384873-4. DOI: 10.1016/B978-0-12-384873-4.00006-2.

[11] R. L. Workman et al. "Review of Particle Physics". *PTEP* 2022 (2022), 083C01. DOI: 10.1093/ptep/ptac097.

[12] Wikimedia Commons. *File:Bragg Curve for Alphas in Air-PT-en.svg — Wikimedia Commons*. [Online; accessed 23-February-2023]. 2022. URL: https://commons.wikimedia.org/w/index.php?title=File:Bragg_Curve_for_Alphas_in_Air-PT-en.svg.

[13] W. R. Leo. *Techniques for Nuclear and Particle Physics Experiments*. Springer-Verlag, Berlin Heidelberg, 1994. ISBN: 978-3-540-57280-0. DOI: 10.1007/978-3-658-00386-9.

[14] G. F. Knoll. *Radiation detection and measurement*. 3rd ed. New York: Wiley, 2000. ISBN: 978-0-471-07338-3.

[15] M J Berger et al. "Stopping-Power & Range Tables for Electrons, Protons, and Helium Ions". *NIST Standard Reference Database 124* (2017). URL: https://www.nist.gov/pml/stopping-power-range-tables-electrons-protons-and-helium-ions.

[16] D. Sarrut, M. Bała, and Manuel et al. "Advanced Monte Carlo simulations of emission tomography imaging systems with GATE". *Physics in Medicine & Biology* 66.10 (2021), 10TR03. DOI: 10.1088/1361-6560/abf276. URL: https://dx.doi.org/10.1088/1361-6560/abf276.

[17] H. Kolanoski and N Wermes. *Teilchendetektoren (German version)*. Springer Spektrum, 2016. ISBN: 978-3-662-45349-0. DOI: 0.1007/978-3-662-45350-6.

[18] E. H.M. Heijne. "1980, a revolution in silicon detectors, from energy spectrometer to radiation imager: Some technical and historical details". *Nuclear Instruments and Methods in Physics Research Section A: Accelerators, Spectrometers, Detectors and Associated Equipment* 591.1 (2008), 6–13. ISSN: 01689002. DOI: 10.1016/j.nima.2008.03.015.

[19] Wikimedia Commons. *File:Energy band model (DE).svg — Wikimedia Commons*. [Online; accessed 29-Oktober-2022]. 2020. URL: https://commons.wikimedia.org/w/index.php?title=File:Energy_band_model_(DE).svg.

[20] Wikimedia Commons. *File:Pn-junction-equilibrium-graphs.png — Wikimedia Commons*. [Online; accessed 29-October-2022]. 2020. URL: https://commons.wikimedia.org/w/index.php?title=File:Pn-junction-equilibrium-graphs.png.

[21] M. Ferrero et al. *An Introduction to Ultra-Fast Silicon Detectors*. Taylor & Francis, 2021. ISBN: 978-0-367-64629-5.

[22] A. B. Sproul, M. A. Green, and J. Zhao. "Improved value for the silicon intrinsic carrier concentration at 300 K". *Applied Physics Letters* 57.3 (1990), 255–257. DOI: 10.1063/1.103707.

[23] H. Spieler. *Semiconductor Detector Systems*. Oxford University Press, 2005. ISBN: 978–0–19–852784–8.

[24] S. M. Sze and M. K. Lee. *Semiconductor Devices*. John Wiley & Sons, 1985. ISBN: 978-0470-53794-7.

[25] S. Parker. "A proposed VLSI pixel device for particle detection". *Nuclear Instruments and Methods in Physics Research Section A: Accelerators, Spectrometers, Detectors and Associated Equipment* 275.3 (1989), 494–516. ISSN: 0168-9002. DOI: https://doi.org/10.1016/0168-9002(89)90736-5.

[26] J. Kemmer et al. "Experimental confirmation of a new semiconductor detector principle". *Nuclear Instruments and Methods in Physics Research Section A: Accelerators, Spectrometers, Detectors and Associated Equipment* 288.1 (1990). Proceedings of the Fifth European Symposium on Semiconductors Detectors, 92–98. ISSN: 0168-9002. DOI: https://doi.org/10.1016/0168-9002(90)90470-Q.

[27] I. Perić. "A novel monolithic pixelated particle detector implemented in high-voltage CMOS technology". *Nuclear Instruments and Methods in Physics Research Section A: Accelerators, Spectrometers, Detectors and Associated Equipment* 582.3 (2007), 876–885. ISSN: 0168-9002. DOI: https://doi.org/10.1016/j.nima.2007.07.115.

[28] W. Shockley. "Currents to Conductors Induced by a Moving Point Charge". *Journal of Applied Physics* 9.10 (1938), 635–636. ISSN: 0021-8979, 1089-7550. DOI: 10.1063/1.1710367.

[29] S. Ramo. "Currents Induced by Electron Motion". *Proceedings of the IRE* 27.9 (1939), 584–585. ISSN: 0096-8390. DOI: 10.1109/JRPROC.1939.228757.

[30] D. Berry et al. *4-Dimensional Trackers*. arXiv: 2203.13900[hep-ex,physics:physics].

[31] T. Kimoto and James A. Cooper. *Fundamentals of silicon carbide technology: growth, characterization, devices and applications*. Singapore: Wiley, 2014. 1 p. ISBN: 978-1-118-31355-8.

[32] P. Barletta et al. "Fast Timing With Silicon Carbide Low Gain Avalanche Detectors" (2022). DOI: 10.48550/ARXIV.2203.08554. URL: https://arxiv.org/abs/2203.08554.

[33] T. Kimoto. "Material science and device physics in SiC technology for high-voltage power devices". *Japanese Journal of Applied Physics* 54.4 (2015), 040103. DOI: 10.7567/JJAP.54.040103.

[34] S. Metzger et al. "Silicon carbide radiation detector for harsh environments". *IEEE Transactions on Nuclear Science* 49.3 (2002), 1351–1355. DOI: 10.1109/TNS.2002.1039666.

[35] J.B. Casady and R.W. Johnson. "Status of silicon carbide (SiC) as a wide-bandgap semiconductor for high-temperature applications: A review". *Solid-State Electronics* 39.10 (1996), 1409–1422. ISSN: 0038-1101. DOI: https://doi.org/10.1016/0038-1101(96)00045-7.

[36] N. Moffat et al. "Low Gain Avalanche Detectors (LGAD) for particle physics and synchrotron applications". *Journal of Instrumentation* 13.3 (2018), C03014–C03014. ISSN: 1748-0221.

[37] G. Pellegrini et al. "Technology developments and first measurements of Low Gain Avalanche Detectors (LGAD) for high energy physics applications". *Nuclear Instruments and Methods in Physics Research Section A: Accelerators, Spectrometers, Detectors and Associated Equipment* 765 (2014), 12–16. ISSN: 01689002. DOI: 10.1016/j.nima.2014.06.008.

[38] M. Moll. "Acceptor removal - Displacement damage effects involving the shallow acceptor doping of p-type silicon devices" (2019), 027. DOI: 10.22323/1.373.0027.

[39] Wikimedia Commons. *File:APD3 German.png — Wikimedia Commons*. [Online; accessed 30-October-2022]. 2020. URL: https://commons.wikimedia.org/w/index.php?title=File:APD3_German.png&oldid=510636710.

[40] G. Vagelis. *Description and details of the UCSC single channel board design*. [Online; accessed 20.01.2023]. URL: https://twiki.cern.ch/twiki/bin/view/Main/UcscSingleChannel.

[41] *Open Source Pulse Analysis Software*. URL: https://gitlab.com/dd-hephy/HiBPM/RS_DRS4_run_analysis.

[42] *IMB(Instituto de Microelectrónica de Barcelona)-CNM(Centre Nacional de Microelectònica)-CSIC(Consejo Superior de Investigaciones Científicas)*. URL: https://www.imb-cnm.csic.es.

[43] J. M. Rafí et al. "Electron, Neutron, and Proton Irradiation Effects on SiC Radiation Detectors". *IEEE Transactions on Nuclear Science* 67.12 (2020), 2481–2489. DOI: 10.1109/TNS.2020.3029730.

[44] J.M. Rafí et al. "Four-quadrant silicon and silicon carbide photodiodes for beam position monitor applications: electrical characterization and electron irradiation effects". *Journal of Instrumentation* 13.01 (2018), C01045. DOI: 10.1088/1748-0221/13/01/C01045.

[45] C. Allaire et al. "Beam test measurements of Low Gain Avalanche Detector single pads and arrays for the ATLAS High Granularity Timing Detector". *Journal of Instrumentation* 13.06 (2018), P06017. DOI: 10.1088/1748-0221/13/06/P06017.

[46] A. Sonzogni. "NuDat 3". *National Nuclear Data Center (NNDC) - Brookhaven National Laboratory* (). URL: https://www.nndc.bnl.gov/nudat3/.

[47] *Eckert & Ziegler Nuclitec GmbH*. URL: https://www.nuclitec.de.

[48] S. Agostinelli and J. Allison et al. "Geant4—a simulation toolkit". *Nuclear Instruments and Methods in Physics Research Section A: Accelerators, Spectrometers, Detectors and Associated Equipment* 506.3 (2003), 250–303. ISSN: 0168-9002. DOI: https://doi.org/10.1016/S0168-9002(03)01368-8.

[49] D. Nardella. *Step7 Open Source Ethernet Communication Suite*. [Online; accessed 06.02.2023]. URL: https://snap7.sourceforge.net/.

[50] M. Morley. *JSON-RPC*. [Online; accessed 06.02.2023]. URL: https://www.jsonrpc.org/.

[51] M. V. S. Chandrashekhar, Christopher I. Thomas, and Michael G. Spencer. "Measurement of the mean electron-hole pair ionization energy in 4H SiC". *Applied Physics Letters* 89.4 (2006), 042113. DOI: 10.1063/1.2243799.

[52] A.A. Lebedev, A.M. Ivanov, and N.B. Strokan. "Radiation resistance of SiC and nuclear-radiation detectors based on SiC films". *Semiconductors* 38.2 (2004), 125–147. ISSN: 1063-7826.

[53] S. K. Chaudhuri, Kelvin J. Zavalla, and Krishna C. Mandal. "Experimental determination of electron-hole pair creation energy in 4H-SiC epitaxial layer: An absolute calibration approach". *Applied Physics Letters* 102.3 (2013), 031109. ISSN: 0003-6951, 1077-3118. DOI: 10.1063/1.4776703.

[54] A.M. Ivanov et al. "High-resolution short range ion detectors based on 4H-SiC films". *Technical Physics Letters* 30 (7 2004), 575–577. DOI: 10.1134/1.1783406.

[55] A. Lo Giudice et al. "Average energy dissipated by mega-electron-volt hydrogen and helium ions per electron-hole pair generation in 4H-SiC". *Applied Physics Letters* 87.22 (2005), 222105. DOI: 10.1063/1.2135507.

[56] B.F. Phlips et al. "Silicon carbide pin diodes as radiation detectors". *IEEE Nuclear Science Symposium Conference Record, 2005.* Vol. 3. 2005, 1236–1239. DOI: 10.1109/NSSMIC.2005.1596542.

[57] G. Bertuccio and R. Casiraghi. "Study of silicon carbide for X-ray detection and spectroscopy". *IEEE Transactions on Nuclear Science* 50.1 (2003), 175–185. DOI: 10.1109/TNS.2003.807855.

[58] G. Bertuccio et al. "Advances in silicon carbide X-ray detectors". *Nuclear Instruments and Methods in Physics Research Section A: Accelerators, Spectrometers, Detectors and Associated Equipment* 652.1 (2011). Symposium on Radiation Measurements and Applications (SORMA) XII 2010, 193–196. ISSN: 0168-9002. DOI: https://doi.org/10.1016/j.nima.2010.08.046.

[59] R. C. Alig, S. Bloom, and C. W. Struck. "Scattering by ionization and phonon emission in semiconductors". *Phys. Rev. B* 22 (12 1980), 5565–5582. DOI: 10.1103/PhysRevB.22.5565.

[60] J.E. Eberhardt. "Fano factor in silicon at 90 K". *Nuclear Instruments and Methods* 80.2 (1970), 291–292. ISSN: 0029-554X. DOI: https://doi.org/10.1016/0029-554X(70)90774-3.

[61] I.V. Kotov, H. Neal, and P. O'Connor. "Pair creation energy and Fano factor of silicon measured at 185 K using 55Fe X-rays". *Nuclear Instruments and Methods in Physics Research Section A: Accelerators, Spectrometers, Detectors and Associated Equipment* 901 (2018), 126–132. ISSN: 0168-9002. DOI: https://doi.org/10.1016/j.nima.2018.06.022.

[62] GSI - M. Letinsky. *Bethe Bloch calculator*. [Online; accessed 27-February-2023]. 2022. URL: https://web-docs.gsi.de/~lestinsk/beamcalc/bb.php.